Title
Laboratory studies of frictional sliding and the implications of precursory seismicity

Author
Selvadurai, Paul A.

Publication Date
2015

Peer reviewed|Thesis/dissertation

Laboratory studies of frictional sliding and the implications of precursory seismicity

by

Paul A. Selvadurai

A dissertation submitted in partial satisfaction of the

requirements for the degree of

Doctor of Philosophy

in

Engineering – Civil and Environmental Engineering

in the

Graduate Division

of the

University of California, Berkeley

Committee in charge:

Professor Steven D. Glaser, Chair
Professor Alexandre M. Bayen
Professor Douglas S. Dreger

Fall 2015

Laboratory studies of frictional sliding and the implications of precursory seismicity

Abstract

Laboratory studies of frictional sliding and the implications of precursory seismicity

by

Paul A. Selvadurai

Doctor of Philosophy in Engineering – Civil and Environmental Engineering

University of California, Berkeley

Professor Steven D. Glaser, Chair

The dynamic transition from slow to rapid sliding along a frictional interface is of interest to geophysicists, engineers and scientists alike. In our direct shear experiment, we simulated a pre-existing frictional fault similar to those occurring naturally in the Earth. Laboratory experiments have been used in the past to successfully link the fields of rock mechanics and seismology and have been able to produce better estimates of seismic hazard. These laboratory studies found that prior to large earthquakes a nucleation region grows outwardly. Within this region shear stress is overcome through the accumulation of slip across the fault. This phenomena is referred to as slip-weakening. Once the region grows large enough an earthquake ensues. The growth phase of this nucleation zone is called the premonitory phase. Newer seismological instruments are showing that this phase actually carries seismic signatures (originally thought to be an aseismic process). This precursory seismicity is observed as foreshocks and migrating swarm-like foreshocks occur at the fringe of this expanding nucleation front. The previous laboratory studies, used to develop the major phenomenological earthquake models, did not observe this precursory seismicity, possibly due to the lack of sensors capable of measuring this high-frequency phenomenon. The laboratory study reported here has incorporated appropriate sensors that can detect foreshock events on the fringe of a nucleation zone prior to a gross fault rupture (main shock).

During loading we observed foreshocks sequences as slip transitioned from slow to rapid sliding. These laboratory-induced foreshocks showed similar acoustic characteristics and spatio-temporal evolution as those detected in nature. Through direct observation (video camera), foreshocks were found to be the rapid, localized (millimeter length scale) failure of highly stresses asperities formed along the interface. The interface was created by the meshing of two rough polymethyl methacrylate (PMMA) bodies in a direct shear configuration. A carefully calibrated pressure sensitive film was used to map the contact junctions (asperities) throughout the interface at a range of applied normal loads F_n. Foreshocks were found to coalesce in a region of the fault that exhibited a more dense distribution of asperities (referred to as the *seismogenic* region).

Microscopy of the interface in the *seismogenic* region displayed a variety of surface roughness at various length scales. This may have been introduced from the surface preparation techniques use to create a mature interface. The mature interface consisted of 'flat-topped' asperity regions with separating sharp valleys. The 'flat-topped' sections spanned millimetric length scales and were considerably flatter (nanometric roughness) that the roughness exhibited at longer length scales (tens of millimeters). We believe that the smoother, 'flat-topped' sections were responsible

for the individual asperity formation (determining their size and strength), whereas the longer length scale roughness influenced the asperity-asperity interaction during the nucleation phase. Asperities in the *seismogenic* region where shown to exist close enough to each other so that elastic communication (through the off-fault material) could not be neglected.

Prior to gross fault rupture (i.e. mainshock), we measured the propagation of a slow nucleating rupture into the relatively 'locked', *seimsogenic* region of the fault. Slow slip dynamics were captured using slip sensors placed along the fault that measured a non-uniform slip profile leading up to failure. We found that the propagation of the slow rupture into the locked region was dependent on the normal force F_n. Higher F_n was found to slow the propagation of shear rupture into the locked region. Within the relatively 'locked' region, a noticeable increase in size and a more compact spatial-temporal distribution of foreshocks were measured when F_n was increased.

In order to develop an understanding of the relationship between F_n and the resistance of the fault to slow rupture, a quasi-static finite element (FE) model was developed. The model used distributions of asperities measured directly from the pressure sensitive film in a small section of the interface where foreshocks coalesced; specifically, the region where the slowly propagating slip front encountered the more dense distribution of asperities. A single asperity was modeled and followed the Cattaneo partial slip asperity solution. As the shear force increased along the fault, the asperities in this model were able to accommodate tangential slip by entering a partial sliding regime; the central contact of the asperities remained adhered while sliding accumulated along its periphery. Partial slip on the asperity propagated inwards as the shear force was incrementally increased. A further increase in the shear force caused the asperity to enter a full sliding condition. Increasing confining loads caused increased stiffness and increased capacity to store potential shear strain energy – a possible measure of the 'degree of coupling' between the fault surfaces. Physics from the numerical model followed the qualitative observations made using photometry of asperities along the interface, which visualized asperities in the 'locked' region – larger asperities remained stuck throughout the loading cycle and the light transmitted through individual asperities decreased from the periphery as shear loads increased.

The numerical partial slip, quantified by the potential energy stored by the asperity, increased relative to the normal pressure p. Asperity-asperity interactions were modeled along the interface using a quasi-static analysis. Progression of slip into the asperity field was increasingly inhibited as the normal confining force F_n was increased. The computational model provided an explanation as to why an increased confining force F_n could result in an increased resistance to slow rupture as well as an increased potential for larger foreshocks within the resistive, relatively 'locked' section of a fault. The experiments and modeling presented in this study lay the foundation for more innovative laboratory work that could potentially improve the phenomenological models currently used to estimate earthquake hazard.

To parents Patrick and Sally, my sisters Emily and Elizabeth, my brother Mark, my Friends and Moose

Contents

List of Figures

Acknowledgments

I am grateful to my research supervisor Professor Steven D. Glaser for providing me with a unique opportunity to conduct research under his supervision. He has taught me patience and to believe in my abilities. His support in my abilities has not wavered once during my time at UC Berkeley.

Next, I would like to thank my family for their support throughout my entire academic career. My father, Patrick, has been an influential and driving force towards continuing my studies. His knowledge and insight never ceases to impress me. My mother, Sally, has provided me much needed advice with regards to my writing and was also influential in my decision to continue my education. My siblings (Emily, Mark and Elizabeth), have always supported the decisions I've made and their support was crucial during some of the tribulations I've endured over the last five years.

A very special and deserved acknowledgment is directed to my friend, Greg McLaskey. My apprenticeship under him upon my arrival at UC Berkeley was important and instrumental in this body of work. I truly enjoy and continue to appreciate the discussions we've had and will have in the years to come.

All my lab mates should also take a bow. A special thanks must be sent to Chris Sherman, Mario Magliocco and Ziran Zhang. All of them have been helpful and provided great feedback regarding my studies. While their academic advice was spot on, I could always come to them and receive sound personal advice, thank you.

I have made so many friends since moving to California. And have lost some (Dan, Karen and Anna). They have provided my foundation and I truly appreciate our times together.

The research support provided by the Natural Sciences and Engineering Research Council of Canada in the form of a traveling doctoral fellowship, the research support provided by the University of California, Berkeley in the form of the Lady Jane Lewis Fellowship and the support from the National Science Foundation are gratefully acknowledged.

Finally, there's Moose. The adorable little Boston terrier that has been here throughout and stuck out some hard times in California. No matter how tough the times and how bad I felt, he always puts a smile on my face.

Chapter 1

Introduction

1.1 General

Our understanding of earthquakes is that they are produced when either intact rock fractures rapidly or fractured rock interfaces experience rapid slip. Energy released from these processes is conveyed to frictional heating, wear of the faulting surfaces and seismic radiation. While seismic radiation is considered to be a small portion of the energy released during an earthquake [3], these waves are what we feel and can cause tremendous damage to infrastructure and loss of human life. The unpredictable and devastating nature of earthquakes and our general lack of understanding of their physics has motivated this study and many other studies in the field of seismology and engineering.

Earthquakes are unpredictable, but are confined primarily to faults that occur along the boundaries of tectonic plates that make up the Earth's crust (lithosphere). A fault is a fracture that may or may not be active. Activity depends on the stress states along the fault and in the surrounding rock mass. As the tectonic plates are driven past each other by geodynamic processes, shear stress builds up along a fault until it overcomes the forces which hold it together and an earthquake is produced. The change in the stress states that drives instability is referred to as nucleation. Nucleation is a topic of great importance due to its immediate impact on the predictability of earthquakes and is a main focus of this dissertation. Are there precursory events intrinsic to the nucleation of large or small earthquakes? Can we detect these changes in nature? Are better sensors/sensor placement needed to do so? Can we develop analogs that simulate earthquake physics and increase our knowledge of these precursors in controlled laboratory environments?

Nucleation and earthquake prediction are primarily studied in three scientific disciplines: seismology, geology and rock mechanics. Seismology is the study of the generation, propagation and recording of elastic waves in the Earth and the sources that produce them [106]. Geology is primarily concerned with the study of the faults themselves and their origins. In the past, study of earthquakes, fell most often into these two disciplines since the consensus was that they must be inter-related – faults cause earthquakes [48, 152]. Rock mechanics arrived later allowing the study of the mechanical behavior of rock and rock masses with respect to the force fields of their environment. Mechanicists believed that natural earthquake phenomena are defined by the material properties of the rock, their surfaces and stress states [161]. We believe this to be an appropriate approach for developing better understanding of the factors controlling earthquake nucleation on

natural faults [23]. The marriage of seismology and rock mechanics has shown great promise, especially in a laboratory setting [e.g. 61, 65, 110, 113]. Laboratory studies allow for the accurate monitoring of features controlling nucleation.

Our understanding of earthquakes and faulting in nature has been directly impacted by laboratory studies, where experiments allow the measurement of fault asperity behavior with details that cannot be readily discerned from field data. There are still many open questions about mechanistic fault behavior leading up to gross rupture; in this dissertation we will investigate the mechanistic components of pre-slip along the frictional interface. Pre-slip (also referred to as premonitory slip [179, 161]) is slip that accumulates along the fault brought on by far-field tectonic loading. Pre-slip is a byproduct of the nucleation process – a frictional process that dictates the dynamic breakdown of stress on a fault and the transition of stable to unstable sliding. Unstable slip generates the elastodynamic stress waves we perceive as earthquakes. Pre-slip occurs in a quasi-stable/static manner [56, 139] and (if detectable) can lead to better estimates of seismic hazard or even prediction. Spatially, pre-slip accumulates non-uniformly on faults due to the presence of asperities. Asperities can be considered as rheological differences due to variations in material properties (elastic modulus, plasticity, material strength, etc.), stress states or environmental factors (e.g. pressure, temperature). Asperities formed along rock-rock interfaces have been interpreted as forming and behaving due to thermo-hydro-mechanical (THM) interactions [152]. In this dissertation the mechanical aspect causing rheological difference in the laboratory is controlled. Asperities distribution along a frictional interface is controlled via mechanical interactions; surface roughness and the applied pressure to two bodies forced into contact are the main features controlling asperity formation. I have set out to study, in the laboratory, how varying the asperity distribution affects pre-slip accumulation before large earthquakes. Our lack of insight into local frictional faulting processes makes predictive determination of why, when and where large earthquakes will occur impossible. For example, we currently have little understanding of the physical mechanisms that control pre-slip due to limitations in the field such as sensor sensitivity, sensor proximity to the fault and array coverage.

1.2 Field observations

1.2.1 Seismological and geodetic instruments

The ability of laboratory experiments to reproduce and behave analogously to observations made in nature is entirely dependent on the quality of both laboratory and field measurements. The primary goal of laboratory studies is to develop a mechanistic understanding of observations made in the field. Figure 1.1 shows examples of typical field measurements. Figure 1.1(a) is the vertical component of a velocity seismogram recorded by field seismometers (Mark Products L22-D) from Iio [86]. Figure 1.1(b) shows global positioning system (GPS) velocities near the San Francisco Bay Area relative to site LUTZ on the Bay Block. The velocities show right-lateral deformation and deformation gradients across the fault itself (red lines). Figure 1.1(c) shows accurate interferometric synthetic aperture radar (InSAR) measurements of the surface displacement in the line of sight between the satellite and the ground along the central San Andreas fault between May 1992 and January 2001. Figure 1.1(d) uses InSAR measurements to estimate the slip rates along the Hayward-Calaveras Fault system (HCFS) from surface creep inversion. Figures 1.1(b), (c) and (d) are used courtesy of the Active Tectonics group at University of California, Berkeley. Inverting for

fault slip rates from surface slip rates (GPS) [42] or repeating earthquakes (seismograms) [129] or both (GPS and seismograms) [130] are now commonly used to develop an intimate understanding of slip and slip rates along faults. These studies have found that faults are not simply 'locked' (i.e. no relative motion/slip across the faults) but 'creep' non-uniformly at different rates (Figure 1.1(d)). The slow, non-uniform motions of the faults cause a local increase of strain energy. At some point, conditions become favorable and a large earthquake is produced. This is also referred to as instability in nucleation theory (see Section 1.3.1). Once a large earthquake commences, rupture can move along the frictional fault or create new faults [100]. During an earthquake, rupture propagates at speeds closer to the shear velocity V_S of the material [3]. Energy released during an earthquake is called the seismic moment M_0 and is given as

$$M_0 = G \cdot A \cdot \bar{\delta} \tag{1.1}$$

where G is the shear modulus of the material (N/m^2), A is the faulting area (m^2) and $\bar{\delta}$ is the average slip (m) along the faulting area A. Seismic moment in (1.1) has units of N·m.

The earthquake itself only accounts for a small fraction of time of the total earthquake cycle. The cycle is composed of an interseismic and seismic portion. Time-scales of the intersesimic phase are slow (accumulation of slip can be from years to centuries) and the seismic event is rapid (seconds to minutes). The total seismic moment M_{0T} of the earthquake cycle can be separated into the total aseismic moment M_{0A} (from the interseismic phase) and coseismic moment M_{0C} (from the seismic phase). For total seismic moment, equation (1.1) can be rewritten as

$$M_{0T} = M_{0a} + M_{0c} = G \cdot A \cdot \left(\bar{\delta}_a + \bar{\delta}_c\right). \tag{1.2}$$

where $\bar{\delta}_a$ is the average aseismic slip and $\bar{\delta}_c$ is the average coseismic slip (both in meters) along the faulting area A.

The focus of this study is the preparatory portion of the cycle that leads up to large earthquakes. This is referred to as the premonitory or nucleation phase. During the premonitory phase slip accumulates slowly. Prior to the generation of large earthquakes a nucleation zone grows outwardly in a stable manner along the frictional fault. Inside this region, slow premonitory slip (pre-slip) can accumulate. Fault rheology determines how this pre-slip is allowed to accumulate and its heterogeneous distribution. Some parts of the fault are considered to be *locked* (resistive to rupture) and/or *creeping* (unable to sustain shear stresses). Large earthquakes tend to be initiated at the boarder of the locked-creeping section of the fault [130, 12, 41]. We have little knowledge of the mechanical factors controlling the accumulation of slip on the locked-creeping section. Higher quality field sensors and coverage have allowed seismologists to see small earthquakes that were previously undetected. These smaller earthquakes at the locked-creeping fringe may describe breakdown processes but the mechanical interactions and how they relate to the large earthquake in that region remains unknown.

1.2.2 Precursor seismicity before large earthquakes

The mechanical model describing the transition of frictional sliding from slow (stable) to rapid (unstable) is described in Section 1.3.1. Both laboratory [e.g., 62, 140, 119, 162] and numerical studies [e.g., 104, 4, 94] have shown that a preparatory phase (nucleation) exists where a region of slow aseismic accelerating fault slip precedes a large earthquake. Detection of the precursory

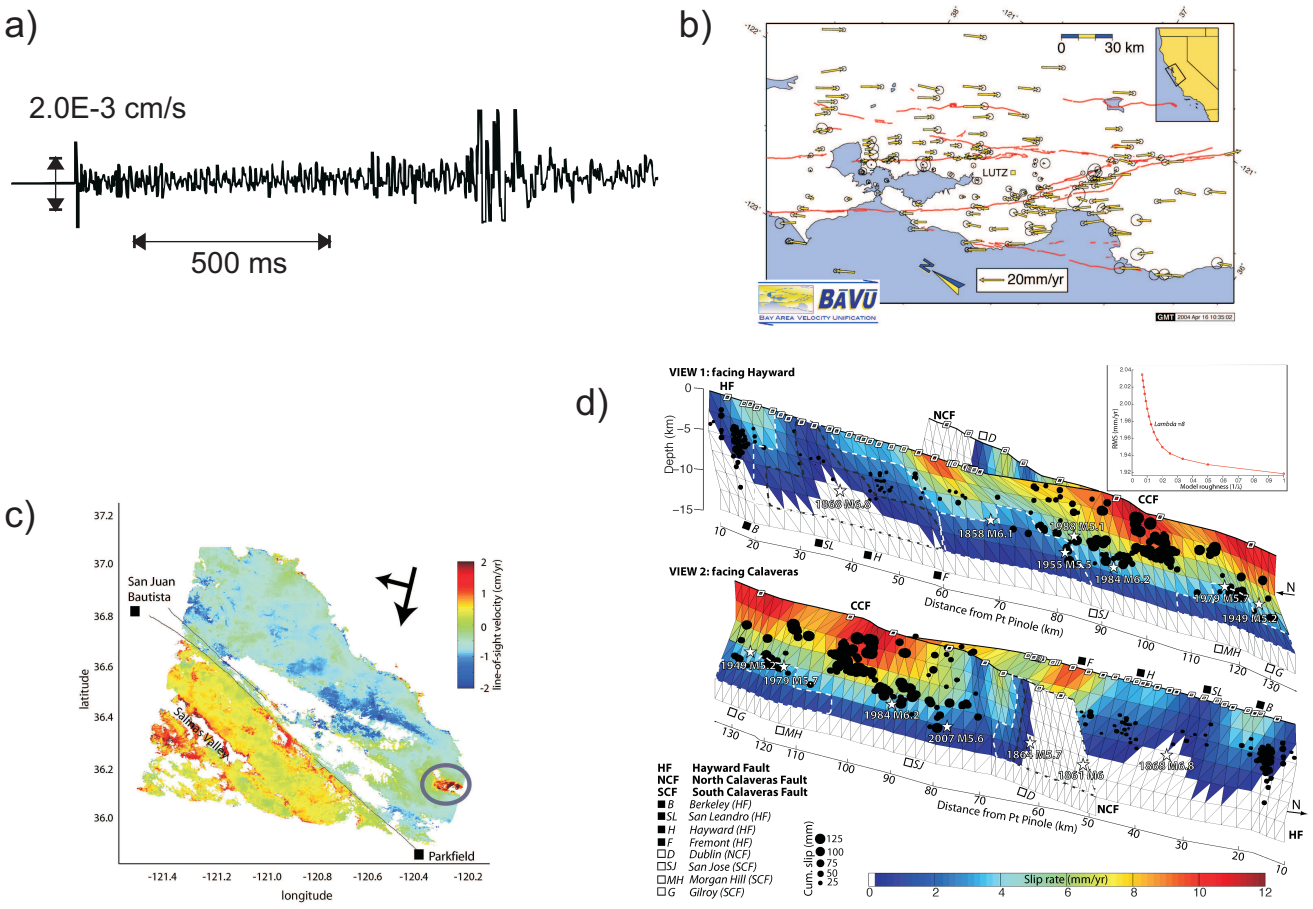

Figure 1.1: **(a)** Vertical component velocity seismogram recorded by seismometers from Iio [86]. **(b)** GPS (global positioning system) velocities near the San Francisco Bay Area. **(c)** Vertical ground velocities along the central San Andreas fault between May 1992 and January 2001 found using InSAR (interferometric synthetic aperture radar) **(d)** Example of inversions performed to solve for slip rates along the Haward- Calaveras Fault system (HCFS) from surface creep inversion. Figures 1(b), 1(c) and 1(d) were taken courtesy of the Active Tectonics group at University of California, Berkeley.

phase is extremely difficult using current geodetic measurements [179, 155] due to array coverage and location constraints, and the small size and limited timing of the accelerating aseismic region. However, with recent advances in broadband seismometers, recorded events are smaller and went previously undetected. This seismicity is generated at the fringe of the nucleation region. Seismologists have begun looking at this seismic activity as an indicator of the otherwise aseismic preparatory phase. In certain cases, clusters and swarms of small earthquakes and/or foreshocks have been detected weeks to minutes before and in close proximity the eventual main shocks [e.g., 126, 93, 138, 131, 68, 67, 49, 75, 175]. It is now believed that at least 50% of major intraplate earthquakes have foreshocks [37], whereas Bouchon et al. [32] believe it to be more in the range of $\sim 70\%$ for intraplate earthquakes. Foreshock sequences and slow slip processes prior to recent, well-monitored large earthquakes, i.e. the 2011 Tohoku-Oki, Japan, [97] and the 2014 Iquique earthquakes [37, 183] are forcing scientists to reconsider original estimates of spatial and temporal scales over which preparatory phases occur.

A priori detection of foreshocks are currently difficult (if not impossible) to distinguish from non-precursory seismic activity – much of this is the result of our lack of understanding of the mechanical processes controlling precursory seismicity. Interpretation of the impact of stress changes along faults are not well understood; in certain cases, earthquake swarms do not culminate in a major event [82]. The exact relation between foreshocks and the aseismic preparatory phase is also debatable [124]. Two concurrent conceptual models exist that explain the presence of preparatory seismicicity: (*i*) the *pre-slip* and (*ii*) the *earthquake cascade* models [70, 23, 181]. In the *pre-slip* model, slow aseismic slip is responsible for foreshocks and other precursory seismic activity. If the slow slip is below the detection threshold of modern geodetic networks, the seismicity produced is a means to monitor the extent and growth rate of the slow slip region. The size of this region, as we will see from Section 1.3.1, determines the stability of the fault – once a nucleation region reaches a critical size, unstable rupture will ensue. Better estimates of the size and growth rate of the nucleation zone could lead to better estimates and the possible prediction of the larger impending earthquakes. Conversely, the *earthquake cascade* model does not require an initial region of slow slip. Here, earthquakes trigger the subsequent event. Each event is a 'foreshock' to the previous event – the main shock thus has only one foreshock (not a sequence) and triggering is due to dynamic or after-slip stress perturbations (triggering). Prediction becomes futile for the *breakaway earthquake* model; there is a lack of understanding of the fundamental mechanics, which is unlike that describing the nucleation theory for the *pre-slip* model. Epidemic-Type Aftershock Sequence models (ETAS) [137] use empirically based laws (i.e. Gutenburg-Richter and Omori time diffusion law) to study after-slip triggering. This model implicitly assumes that any transient change in the overall seismicity is due to the triggering of an earthquake by another one. In my research I have made studies of the preparatory phase along a frictional fault and the seismicity (specifically foreshocks) prior to a large main shock.

1.3 Laboratory friction studies

1.3.1 Nucleation theory

Nucleation theory determines the dynamic transition of slip along the fault from slow and stable to rapid and unstable. Rapid unstable sliding generates stress waves and these are what we interpret as earthquakes. Mathematically, nucleation of earthquakes on a frictional fault can

be modeled in terms of a either fracture or stick-slip friction [161]. Due to the similarities, nucleation of rapid sliding on a frictional fault is modeled as an expanding shear fracture/crack. A conceptual drawing of a typical premonitory phase along a frictional fault is shown in Figure 1.2. Two bodies are initially pushed together with a normal force F_n (blue arrows). The fictional fault is subsequently subjected to increasing shear force F_s (red arrows). This causes *slip* (δ) along the interface (orange region). Slip is the relative displacement across the interface or $\delta = (u^+ - u^-)$, where u is the displacement and positive and negative superscripts indicate top and bottom sides in the plane of the discontinuity, respectively [3]. Upon first application of shear, slip will initially accumulate from a relatively weak section of the fault. Even though the edges of the two bodies remain locked (i.e. no slip), both the amount of slip within the nucleation zone and size of the nucleation zone will grow with increased shear force. We note that in a tectonic setting, increasing shear force is caused by differences in plate convergence rates [58]. Across the nucleation front, shear stress decreases from an initial level (τ_i) to a residual level (τ_r) by accumulating slip (δ). A critical slip displacement of D_c is required to fully achieve this breakdown (i.e. stress drop $\Delta\tau = \tau_i - \tau_r$), occurring over the length X_c, which is known as the breakdown/cohesive zone (hatched region in Figure 1.2).

In Figure 1.3, two types of shear stress and slip displacement solutions near the crack tip (fringe of the nucleation zone) are examined. Figure 1.3(a) shows the shear stress distribution for a 'singular crack' [15, 100]. The singularity in particle velocity (i.e. vertical tangent in slip distribution) induces a singularity in stress ahead of the rupture. This can be avoided by choosing an appropriate rupture velocity [6, 83] that smoothly transitions over the finite breakdown region X_c, as shown in the profiles shown in Figure 1.3(b). Stress transition is smooth as long as the prescribed slip displacement is C^2 continuous [83]. Avoiding a stress concentration at the crack tip is a logical assumption since real material cannot sustain infinite shear stress.

I will show that as the nucleation zone expands, it can grow until it reaches a critical size L_c after which an earthquake is produced. Since premonitory slip is that accumulated within the nucleation zone, and this may directly be linked to precursory seismicity, we proceed to examine the mathematical principles in more detail. The concept of surface energy, as applicable to crack stability and growth, was first introduced by Griffith [79]. For a shear fracture working against friction the solution for critical nucleation size can be determined from first principles. Displacement of the crack u^+ is given as [99]:

$$u^+ = \frac{\tau_i - \tau_r}{G}\left(L^2 - x^2\right)^{1/2}. \tag{1.3}$$

where G is the shear modulus and the crack has a finite length $\in [-L, L]$. Slip δ is twice as large as equation (1.3) [3]. The slip distribution is used to calculate the strain energy accumulated from both sides of the fault U and the work done against friction to produce the crack W ($= 2 \cdot \tau_r \int \delta dx$). The energy available to supply surface energy and extend the crack is then calculated [6]:

$$-U - W = \frac{\pi}{2}\frac{1}{G}\left(\tau_i - \tau_r\right)^2 L^2. \tag{1.4}$$

The incremental change in energy required to increase the crack half-length from L to $(L + \Delta L)$ is therefore

$$-dU - dW = \pi\frac{1}{G}\left(\tau_i - \tau_r\right)^2 L dL. \tag{1.5}$$

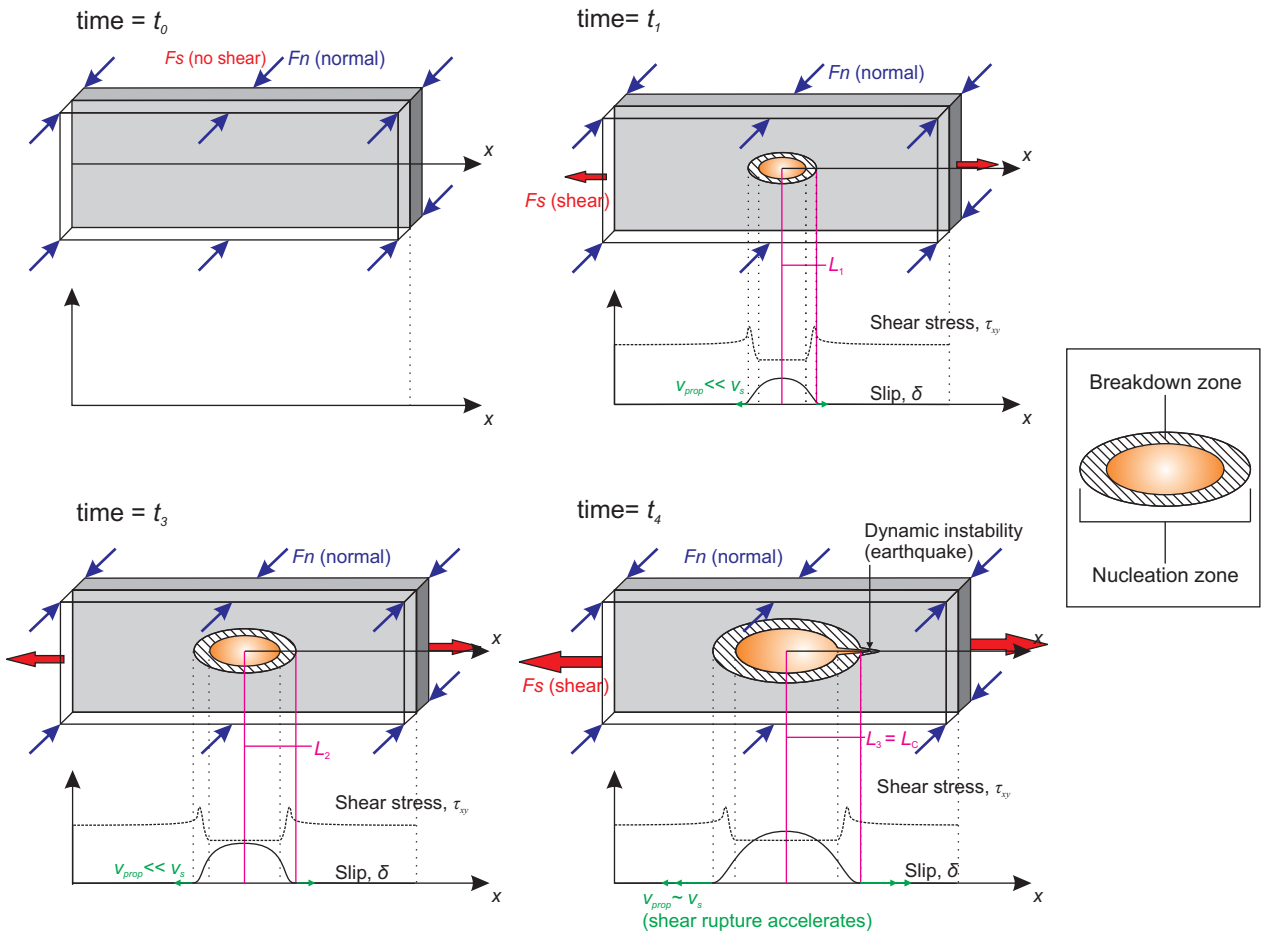

Figure 1.2: Schematic drawing describing the expansion of a shear rupture on a frictional fault. At time $t = t_0$, two bodies are pressed together under normal force F_n creating a frictional interface. In this description of the nucleation process (equations (1.3) - (1.6)) the normal force remains constant and there is no fault dilatation. From time $t = t_1$ to t_4 a shear force is applied which causes the growth of a nucleation zone, a region where slip (differential motion of the fault) is allowed to accumulate. A breakdown zone exists at the fringe of the nucleation zone. In this region the slip-weakening constitutive relation allows for the decrease in shear stress with accumulated slip. Once the crack reaches a critical half-length L_c it will begin to accelerate to velocities closer to the shear velocity of the material V_s.

As the crack reaches a specific critical crack half-length L_c, the energy available balances the energy required to incrementally lengthen the crack, i.e. $4\Gamma \cdot dL$ (Γ is the effective fracture energy with units N/m). Equating Γ to equation (1.5), we solve for the critical crack half-length:

$$L_c = \frac{4}{\pi} \frac{G \cdot \Gamma}{(\tau_i - \tau_r)^2}. \tag{1.6}$$

The schematic drawing in Figure 1.2 shows a growing nucleation front made by the unstable shear crack along a frictional fault. From time t_0 until t_3 the crack extends due to increasing shear loads on the fault. At time t_4 the crack half-length equals the critical half-length given by equation (1.6). Extension of the crack beyond this causes unstable propagation and acceleration of the crack tip is given by equation (1) in Andrews [6]. The derivation of critical crack length (via equations (1.3)-(1.6)) describes the case where shear fracture occurs but now we must quantify the effective fracture energy Γ using a constitutive model that links the shear stress to slip.

1.3.2 Constitutive modeling of an expanding nucleation zone

One constitutive model governing breakdown of stress by the accumulation of slip is called the *slip-weakening* relation [6, 141]. This relation determines how the crack grows and how much premonitory slip is accumulated during breakdown. Shear stress can be written as a function of slip as follows:

$$\begin{aligned} \tau_{xy}(\delta) &= \tau_p - (\tau_p - \tau_r)\, \delta / D_c \quad \delta < D_c \\ \tau_{xy}(\delta) &= \tau_r \quad \delta \geq D_c \end{aligned} \tag{1.7}$$

where τ_p is the upper yield point, τ_r is the residual or frictional stress level and D_c is the critical slip distance required for stress drop. It is assumed that the initial stress level τ_i lies between the upper yield point and residual stress level (i.e. $\tau_p > \tau_i > \tau_r$). The effective fracture energy Γ is given as the area under the slip-weakening curve but above the residual stress level:

$$\Gamma = \int_0^{D_c} \left[\tau_{xy}\left(\delta\right) - \tau_r\right] d\delta = \frac{1}{4}\left(\tau_p - \tau_r\right) \cdot D_c. \tag{1.8}$$

Using this result with equation (1.6) we obtain

$$L_c = \frac{4}{\pi} \frac{G \cdot \Gamma}{(\tau_i - \tau_r)^2} = \frac{1}{\pi} \frac{G\left(\tau_p - \tau_f\right)}{\left(\tau_0 - \tau_f\right)^2} D_c. \tag{1.9}$$

We now have an expression for the critical crack length in terms of only slip and shear stress. The slip-weakening relation can have different forms [83]. Homogeneity is a necessary conditions within the cohesive zone for the previous derivation to hold. In this dissertation I look at the possibility that the cohesive zone may be populated by strength heterogeneities (i.e. asperities). Scientists believe that foreshocks (and other precursory seismic events) occurring before large earthquakes are due to the localized failure of asperities within the nucleation zone [139, 138, 183, 37]. One such model was proposed by Ohnaka [139] and presented schematically in Figure 1.4(b). The local fluctuations in slip and stress caused by the asperities (see Figure 1.4(d)) could evoke a slightly different slip-weakening relation (dashed line in Figure 1.4(a)). A better understanding of the true slip-weakening relations that can account for local strength heterogeneity,

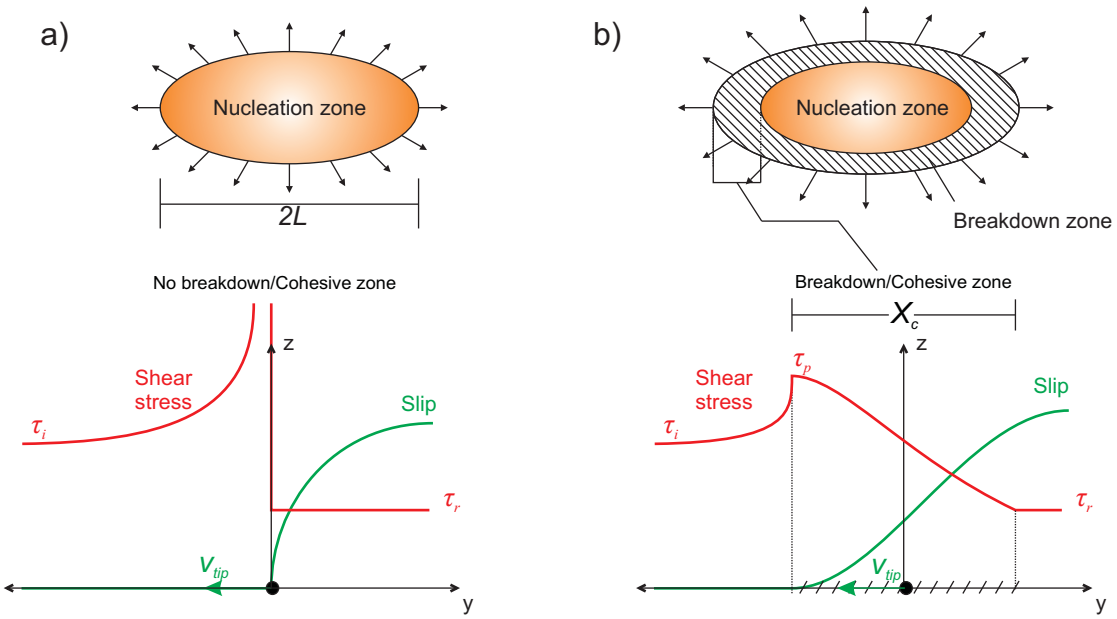

Figure 1.3: Slip and stress distributions at the fringe of the nucleation region with (a) no cohesive zone and (b) with a cohesive zone.

may help us to appreciate the intricacies of nucleation region growth, pre-slip accumulation and precursory seismicity. In this dissertation, I will discuss the presence of premonitory seismicity in the laboratory. I look at how the slowly growing nucleation interacts with a resistive patch of asperities. The concept is presented in Figure 1.4(c). I wish to understand what conditions (stress states, pre-slip accumulation, slip rates) are necessary/control the generation of foreshocks in the nucleation region.

1.3.3 Applications of nucleation theory and current issues

There are two main types of constitutive relationships to describe nucleation theory: slip-weakening (also known as slip-dependent) [6, 141] and rate- and state-dependent (RS) laws [61, 157]. The former assumes that friction only depends on fault slip and, unlike the RS relation, it is slip-rate and time insensitive. The slip-dependent relation is the rate-insensitive limit of the RS framework. Slip-weakening concepts are rooted in the laboratory-derived rate- and state-dependent (RS) constitutive relation [61, 157, 104, and references therein]. Both have proven success in studying dynamic traction behavior throughout natural earthquake cycles [e.g., 179, 151, 66, 94]. A variety of laboratory setups, in a variety of configurations, have been used to develop and confirm the rate-and-state frictional relation empirically [60, 59, 65, 142, 113, 26]. However, the empirical nature of the RS law does not take micromechanics directly into consideration; it only captures a collective behavior of the asperity populations [185].

Shear stress drop (across the breakdown zone) physically represents the birth and death of populations of asperities over a critical slip distance D_c [186, 185]. If foreshocks appear within the nucleation zone, this would violate the original phenomenological observation [61] used to

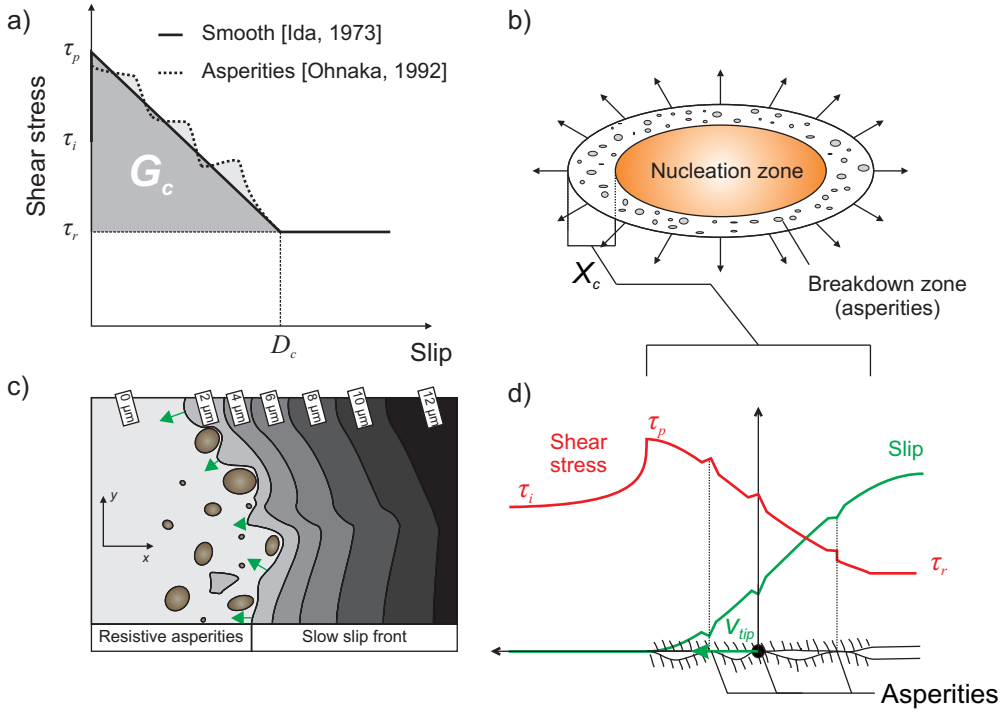

Figure 1.4: (a) Slip-weakening relation for the homogenous cohesive zone (solid line) and conceptual model with the presence of strength heterogeneities (i.e. asperities). (b) Schematic description of asperities populating the breakdown zone. (c) Non-uniform accumulation of slow slip as a slowly expanding nucleation region encroaches on a resistive patch of asperities. (d) Slip and stress distribution at the fringe of a nucleation region where the cohesive zone is formed by asperities. This causes local fluctuations in slip and shear stress.

develop the rate-state (RS) law [157]. Whether foreshocks appeared in the original phenomenological observations by Dieterich [61] is unknown but these new precursory seismic observations (both in the laboratory and the field) lend credence to further study frictional nucleation processes in the laboratory.

I use piezoelectric sensors, in addition to the sensors used in the original studies, to observe the more complex features of nucleation; foreshocks can be detected at the fringe of the growing nucleation region [119, 74, 122, 162]. Currently, studies have tried to embed geologic heterogeneity into the RS framework [9, 10, 69, 134] but it is done in a relatively arbitrary manner; spatial distributions and material parameters of the strength heterogeneities are determined by the modeler. Contact mechanics may provide a better understanding of how these geologic heterogeneities (asperities) develop spatially, under a non-uniform normal stress field.

1.4 Contact mechanics overview

The earliest work into contact mechanics to understand frictional effect can be traced back to experiments performed by Leonardo Da Vinci (ca. 1500). Fundamental aspects of friction and its modelization for the purpose of seismic fault dynamics is still under debate [161, 145]. In this dissertation, I focus on the study of 'solid'-dry friction [18] where the wearing process and self-heating play a negligible role and lubrication is not present. For the sake of completeness we give a brief overview of the historical aspects of friction studies and then discuss more recent frictional models.

Friction deals with the interaction of two surfaces and is therefore a contact property and not a bulk property. Frictional resistance to motion is defined as the force arising when a body is slid tangentially on another body where contact forms along a surface. DaVinci's work was re-discovered by Guillaume Amontons [27]. His experiments showed that frictional resistance to sliding decreased as the two contacting surfaces of the body became smoother. In his 1699 paper, Amontons described the two main laws of friction [see 161]:

- Amontons's first law: The frictional force is independent of the size of the areas in contact.
- Amontons's second law: Friction is proportional to the normal load pressing bodies together.

It was during the next 100 years that mechanisms for controlling frictional resistance were proposed. Factors studied included surface roughness, the interactions of protrusions where contacting surfaces met (i.e. asperities), differences in static and dynamic friction and the increase of static friction the longer two surfaces remained at rest.

1.4.1 Adhesion theory of friction

Adhesion theory of friction was summarized by Bowden and Tabor [33] who envisioned real surfaces to have a roughness and when they are brought together they touch at small points called asperities. Figure 1.5 shows a schematic view of the interaction between two rough surfaces. Where the surfaces contact (red regions) are called asperities and the sum of the area is referred to as the real contact area A_r, which is generally much smaller than the nominal or geometric area A. Bowden and Tabor [33] first noted that the real contact formed along an interface was typically orders of magnitude lower than the nominal area of the interface. Only the real contact A_r is responsible for friction; stresses cannot be transmitted through the non-contacting void region (as seen in the inset diagram in Figure 1.5). It is only the area A_r and not A that defines motion of the fault. The behavior of the fault is therefore controlled by the nature of the contact surfaces – its roughness.

In geophysical studies [e.g. 38, 149], the rough interacting rock surfaces showed self-affinity characterized by the Hurst exponent H [31, 43, 44]. The interaction of these self-affine surfaces caused scale dependent heterogeneous normal stress fields [80, 145] which influences friction at low velocities on surfaces that exhibit negligibly small wear effects, i.e., void of gouge [18].

When a normal force F_n is applied (see Figure 1.5), forces are transmitted through the asperities. Asperities can fracture or grow until the far-field normal force is supported over all the contacts. Dieterich and Kilgore [65, 64] confirmed this using optical experiments; populations of

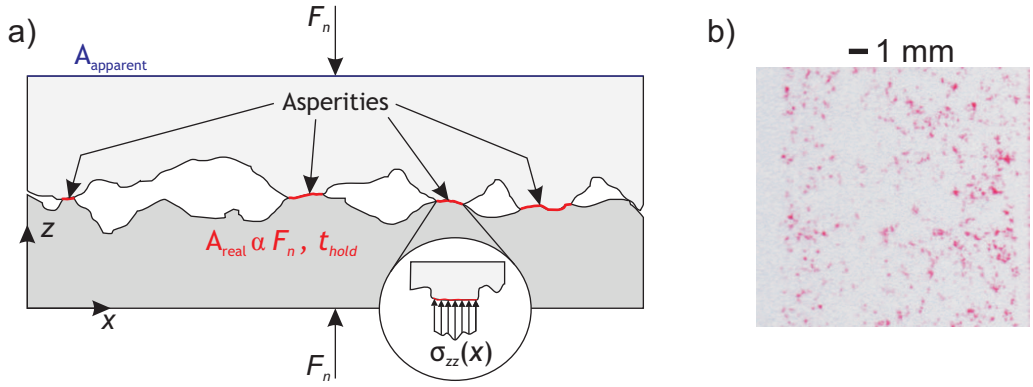

Figure 1.5: **(a)** The contacts formed between the rough-rough surface interactions are asperities (red) region. The total sum of all asperities gives the real contact area A_r which is much smaller than the nominal contact area A (defined by the overall geometry of the surface.) **(b)** An example of the raw measurement from the pressure sensitive film (Section 3) employed to directly measure and locate asperities occurring along the frictional interface. (**NB**: The darker images are indicative of the contact zones.)

'island-like' contact regions, known as asperities, were transmitting the stresses between two lucite bodies. When the bodies were subjected to a nominal squeezing pressure of 2.5 MPa they only observed asperities forming on ~0.5-0.35 % of the nominal contact area A_0. The normal stress field across the asperities was uniform, resulting from localized yielding at the plastic flow limit P_f of the material (also known as the indentation hardness with units of $\mathrm{N/m^2}$). If all asperities yield plastically then the normal load can be written as:

$$F_n = P_f \cdot A_r. \tag{1.10}$$

For adhesive friction, the high compressive stresses at the junction points causes welding of the surfaces. Slip is accommodated along the interface by shearing of these junctions. The constitutive relation describing the amount of frictional force F_f required to break these bonds is,

$$F_f = \tau_s \cdot A_r, \tag{1.11}$$

where τ_s is the shear strength of the material. Combining equation (1.10) and (1.11) gives us the coefficient of friction μ,

$$\mu = \frac{F_f}{F_n} = \frac{\tau_s}{P_f}. \tag{1.12}$$

The constitutive relation given by (1.11) governing the shear interactions, is satisfied if the frictional force is proportional to the real contact area A_r, thus, also satisfying Amontons's first law. Equation (1.10) implicitly satisfies Amontons's second law.

1.4.2 Factors violating adhesive friction theory

While adhesion friction theory elegantly satisfies both Amontons's first and second laws, a number of exceptions exist that allows for equations (1.10) and (1.11) to be violated. Both the

indentation hardness and shear strength are strongly dependent on temperature, pressure and sliding velocity, making the first order approximation of μ more complicated. Lubrication can also change the specific mechanisms allowing for (1.10) and (1.11) [147, 146, 161]. Asperities can interlock and plough through each other, which changes the shear response [163]. The real contact area A_r may also increase or decrease as slip is accommodated along the interface. Finally, the original assumption in equation (1.10) that asperities form and grow through plastic yielding may be incorrect. As the normal force is increased, a single asperity must undergo a transition from an elastic to elasto-plastic, then 'fully plastic' regime [87]. Recent tribological studies have shown that, in ductile metals, only a percentage of asperities form through plastic yielding along the interface and that elasto-plastic and elastic asperities also exist [154, 135]. Figure 1.5(b) shows raw measurements from an experimental pressure sensitive film (discussed in detail in Section 3) that allowed us to locate, size and measure normal stresses on individual asperities. The result show that normal stress does fluctuate along the asperities. Variations in the normal stress field on single asperities indicate that they were not formed under a single 'flow pressure' P_f.

1.4.3 Mechanisms for single asperity formation under normal loads

In the previous section, we addressed some limitations to adhesive friction theory; some of the main issues leading to the violation of equations (1.10) and (1.11) were lubrication, temperature and velocity dependence of hardness and strength, variable A_r with increased friction force, asperity interlocking, and non-plastic formation of asperities. The coefficient of friction (equation (1.12)) is actually a combination of two constitutive relations describing the formation (equation (1.10)) and the shearing of asperities (equation (1.11)). We first examine the formation of asperities under normal loads.

Hertz's [81] first studied the contact formed between two perfectly smooth elastic spheres pressed together under normal forces P (see Figure 1.6). The elastic spheres have a radius of R_1 and R_2, Young's moduli E_1 and E_2 and Poisson's ratio's ν_1 and ν_2. Hertzian contact theory was used by Cattaneo [46], and others [125], as the foundation for more intricate contact models. Deformation fields in the solid can be determined by minimizing the elastic deformation energy. From this we can determine the approach distance s or elastic 'penetration' (i.e. the change in distance between the two centers of the spheres). It is given as

$$s = \left(\frac{R_1 + R_2}{R_1 R_2}\right)^{1/3} \left(\frac{3P(1-\nu^2)}{4E}\right)^{2/3} \tag{1.13}$$

where

$$\frac{1-\nu^2}{E} = \frac{1-\nu_1^2}{E_1} + \frac{1-\nu_2^2}{E_2}. \tag{1.14}$$

For the special case where a sphere with radius $R = (R_1)$ is pressed against a flat surface (i.e. $R_2 \to \infty$) a circular contact patch with radius a_0 is formed:

$$\pi a_0^2 = \pi R s \tag{1.15}$$

for the normal force

$$P = \frac{4E}{3(1-\nu^2)} s^{3/2} R^{1/2}. \tag{1.16}$$

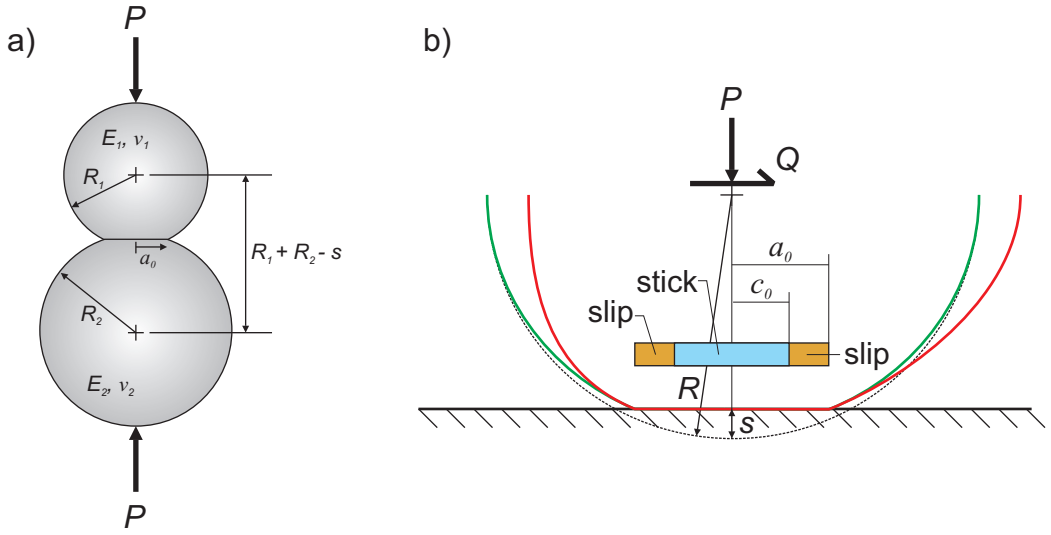

Figure 1.6: **(a)** Contact between two elastic smooth spherical. Spheres are subjected to a normal force P causing the formation of circular contact with radius a_0. **(b)** Schematic drawing of a single asperity compressed and then loaded tangentially [adopted from 143]. Due to loading, slip accrues along the periphery of the contact area and grows inwards with increasing shearing. We refer to this asperity response as a partial-slip asperity.

A concise derivation can be found in Persson [145] who also gives an excellent overview of the current field of contact mechanics. In the next section, we use this derivation and examine the effect of adding shear forces to the Hertzian contact problem.

1.4.4 Mechanisms for single asperity responses under normal and shear loading

Cattaneo [46] elaborated on Hertz's derivation and studied the effects of a sphere pressed against a flat surface and loaded tangentially [see also 125, 51, 50, 30, 186]. Figure 1.6 shows a schematic representation of a spherical elastic body pressed against a rigid flat surface [adopted from 143]. The green line shows the deformation under only normal forces and the red line shows the deformation with the addition of tangential loads. As the tangential load increased slip is accrued along the periphery of the contact region while the central portion remains stuck. Mindlin [125] refers to this as *incipient sliding*. Johnson [Chapter 7 in 87] has presented the full derivation for the partial sliding spherical asperity against a flat plate. The radius of the stuck region is given by c_0 and the full contact radius by a_0 and the ratio is given as

$$\frac{c_0}{a_0} = \left(1 - \frac{Q}{\mu P}\right)^{1/3} \tag{1.17}$$

where Q is the shear force calculated by integrating the tractions over the contact surface ($0 < r \leq a_0$) and μ is the coefficient of friction. Ciavarella [51, 50] generalized the Cattaneo partial slip problem for single, multiple and periodic contacts and, more recently, Paggi et al. [143] formulated the problem for rough surfaces. We use the partial-slip asperity model to interpret experimental

results in a finite element (FE) model (see Section 7). The model takes advantage of locations and size of asperities measured from the pressure sensitive film (Figure 1.5(b)). Each individual asperity abides by equation (1.17). Multicontact interfaces (MCI) take advantage of the fundamental theories for single asperity contacts. They may help in understanding features associated with precursory seismicity since they can provide estimates of local variations in the shear stiffness – a factor that controls the ingress of a shear rupture into a patch of resistive asperities.

1.4.5 Asperity formation on a multicontact interface (MCI)

Single asperity contact has been described in great detail by Mindlin [125] and a more recent overview is given by Johnson [87]. Archard [8] modeled the approach of randomly rough surfaces by modeling a surface made of smaller spherical protrusions on larger spherical protrusions which was pressed into a flat rigid surface. Greenwood [78] was the first to derive a mathematical study applicable for these realistic surfaces. The Greenwood-Williamson (GW) model assumed that the interacting surfaces where composed of spherical bumps of varying heights using statistical distributions. These random heights where defined mathematically as a Probability Density Function (PDF) of interchangeable distributions. The model predicts that as the normal force F_n is increased, real contact A_r increases through two processes [see also 17]:

1. growth of the individual area of previously "active" asperities;
2. growth of the total number N of asperities.

This was clearly observed by direct visualization by Dieterich and Kilgore [64] from experiments performed by pressing two Lucite blocks together in the laboratory. We note that in Dieterich's study, all asperities formed at the flow pressure, which may not be an appropriate assumption as mentioned previously. The model is widely cited in the geophysical literature but invokes some critical assumptions that may not be altogether realistic. One assumption is that contacts are formed independent of each other, meaning the separation between individual asperities must be large. Bowden and Tabor [33] found that the ratio of A_r/A and average asperity area $\bar{a}$ was $\sim 10^{-3}$ and a few microns, respectively. This meant asperities were sufficiently separated (~ 100 µm for the previous study) so they are therefore mechanically independent of each other. Greenwood [76] has recently and criticized his earlier "naive" hypothesis that

> *"[in the GW model, we] assume that a contact is formed whenever a summit meets the opposing surface, and that this contact then grows independently of all other contacts. Thus, the number of contacts steadily increases as the surfaces approach. This is, of course, not what actually happens: the true end of the approach process is that there is only a single contact area. Realistically, contacts do not simply grow, they merge to form 'contact patches'". – J. A. Greenwood.*

Seminal work by Nayak [133] discussed how asperities are formed on interacting surfaces where roughness was defined at two length scales: each length scale affected certain aspects of how the surfaces approached each other. This idea has also been mathematically detailed by Persson [145] and accounts for the formation of asperities where separation distances are small and, therefore, their mechanical independence is no longer valid. The model takes into account the fact that

as the incremental deformation of the asperity tips occurs, the incremental plastic volume reappears as a uniform rise in the nearby surface that is not in contact [see e.g. figure 1 from 133]. This process actually promotes the coalescing of asperities as the normal force is increased, and asperities no longer grow independently of each other as proposed in the GW model. The Nayak-Persson theory promotes irregularly shaped, larger asperities that contain *holes* and non-uniform variations in normal pressure due to the roughness on the coalescing large contact – more similar to Archard's [8] concept of asperities on asperities. The fact that asperities can form dependent of each other under increasing normal force has direct implications on how they react when they are subjected to shear force (or the stress perturbations from an advancing shear rupture). Within the adhesive friction model, bulk shear response of the interface is described by equation (1.11). Newer studies have determined that a level of shear elastic communication between neighboring asperities exists due to their close proximity [45, 2, 150, 184].

1.5 Other applications of this research

Seismicity is generated from a source, e.g. it is asperity failure in the context of this dissertation. Seismologists have become experts at deciphering properties of these sources; i.e. the mechanism associated with the rapid release of energy within the rock mass. This source holds information about the stress changes due to engineering activities that are perturbing the fault either intentionally or unintentionally. The seismicity is, however, an indicator of something that has already happened – the bulk stress states of the rock mass generating seismicity are still elusive. The primary goal of laboratory tests is to produce analogous seismicity and carefully monitor stress states that cause them. A greater understanding of the stress states surrounding nucleation of rapid shear rupture along frictional faults is important in many engineering endeavors, such as enhanced geothermal systems (EGS), geologic sequestration of CO_2, deep geologic disposal of high-level nuclear waste, oil and gas recovery, slope stability with regards to landslides, hydraulic dam stability (e.g. taillings dams), mining safety, among others.

In projects where fluids (or proppants) are injected into a rock mass with a fracture network, one major concern is whether a pre-existing fracture (or fault) experiences frictional sliding or the generation of new fracture surfaces. With regards to EGS and oil and gas recovery, the goal is to generate new fracture surfaces without uncontrolled extension of fractures (referred as *induced seismicity*). While large scale seismicity has to be avoided [174], scientists and engineers have begun to observe small, previously undetectable seismicity [29] due to improved instrumentation and down-borehole seismometers [102, 92]. This small seismicity carries important information regarding a cohesive zone (or process zone) lagging the fracture tip [see e.g. 112, 128, 85, 111]. Laboratory efforts (such as those described here) are attempting to better understand this seismicity in relation to the sudden transition from quasi-static to dynamic slip along the fault.

While the previous applications require the generation of new surfaces, lack of seismicity becomes paramount during other activities. When disposing of nuclear wastes in deep geologic repositories [166], physical excavation of the repository may cause damage and seismic monitoring can help evaluate the extent of this damage. The irreversible processes associated with seismicity can increase the hydraulic permeability in an endeavor where water ingress is highly detrimental to the safety of millions of people.

Sequestration of CO_2 in saline aquifers has also become important in lieu of the negative effects

that greenhouse gasses have on our climate systems. Ensuring that the supercritical CO_2 remains within an aquifer for long periods (thousands of years) means that local monitoring of seismicity is important. A major problem for these projects are fractures of the low permeability cap rock, which retains the gas at depth within the aquifer [127]. Fractures that lead to the release of gases is counterproductive to the ultimate goal of reducing carbon emissions and may be potentially harmful and deadly if they occur on shore [53].

Chapter 2

Experimental facilities

In this chapter we detail the general experimental configuration used in this study. The setup is a direct shear apparatus that measured slow premonitory slip and precursory seismicity along a fault leading up to dynamic failure. We used a pressure sensitive film to better understand the initial distributions of asperities along the fault. A video camera was able to detect light transmitted through asperities during the experiments. All the tools detailed in this chapter have increased our understanding of the processes controlling heterogeneity in premonitory slip accumulation.

2.1 General experimental setup

A schematic view of the direct shear friction apparatus used in the experiments is shown in Figure 2.1(a). The reaction frame accommodated the larger PMMA base plate (600 mm x 300 mm x 50 mm thick) and could apply a normal force (F_n) of 5.8 kN through two balanced hydraulic cylinders (Parker H3LLT28A) and a rigid loading platen to a PMMA slider block (400 mm x 80 mm x 13 mm thick). The PMMA slider block was bonded to the rigid loading platen using cyanoacrylate. The PMMA-aluminum shear bond, tested in a separate load frame, had a shear stiffness of 28 N/µm compared to the 0.42 N/µm stiffness of the PMMA–PMMA interface determined subsequently. Gross interface stiffness is commonly calculated as the total force released divided by the amount of rapid slip during a stick-slip event [19]. A more detailed understanding of the interface stiffness is provided in Section 7, which examines stiffness in the slower, preparatory phase of nucleation. A maximum normal stress of $\sigma_n \approx 1.14$ MPa can be applied to the nominal surface area of the simulated fault (12.7 mm x 406 mm). The normal force (F_n) was estimated from an in-line pressure transducer (OMEGADYNE PX329-2KG5V) that measured the pressure in the hydraulic cylinders. To induce a shear force along the fault we used an electro-mechanical shear actuator (Exlar Tritex II T2X115) with shear stiffness of 154 N/µm operating at 1 Hz. The shear actuator was used to drive the rigid loading platen at a constant velocity V_{LP} while maintaining a normal force F_n on the slider block. The shear force (F_s) was measured using a load cell (OMEGADYNE LC213-1K) placed between the shear actuator and the loading platen. Detailed drawings of the individual components and load frame are presented in Appendix A. (**NB**: The detailed drawings in Appendix A differ slightly from that described in this study. It represents the most recent version of the apparatus (ca. 11/18/2015). However, the general dimension required to reproduce the results presented here remain identical and the only difference is the increase in the number

of sensors.)

2.2 Instrumentation

The general arrangement of sensors used in this investigation is shown in Figure 2.1(c). We used non-contact eddy current induction sensors (SHINKAWA VS-020L-1) at seven locations along the fault (NC1-NC7) to measure the macroscopic longitudinal slip along the fault. Slip is referred to as the differential displacements across the interface (see Section 1.3.1). Two eddy current sensors were placed at the leading (LE) and trailing edge (TE, the edge in contact with the thruster) of the slider block in the y-direction. These allowed us to index the slider block with respect to the base plate and measure for any twisting during failure of the interface. Aluminum targets were used to change the inductance of the magnetic field, which was linearized using a displacement converter (SHINKAWA VC-202N), over frequency ranges from DC to 20 kHz (-3 dB), and showed linearity $\sim 444.52 \pm 0.11$ µm/V between 0 and 2000 µm with a resolution of 0.1 µm for each sensor. Mounting of the targets to the sample was done with a minimal amount of cyanoacrylate in a similar manner to Ohnaka and Shen [140].

Acoustic emission sensors have been used in the past to study nucleation processes of rock failure in the laboratory [e.g., 110, 176, 171, 74, 120]. An array of 15 Glaser-type conical acoustic emission sensors (PZ1-PZ15) was placed on the underside of the base plate (Figure 2.1(c)). The detailed layout of the acoustic emission array and non-contact sensor array can be seen in Figure 2.2(a). These sensors were absolutely calibrated beforehand using the techniques of McLaskey and Glaser [117, 116]. They detect fault normal displacements from a near-field vantage point with a frequency bandwidth of ∼5 kHz to 2.5 MHz (-3dB) with ± 1 pm noise floor [117]. The sensors were connected to a high-speed digitizer (ELSYS TraNET EPC 16-bit dynamic range, 10 MHz sample rate) and measured the small dynamic stress waves (foreshocks) that were emitted before the block experienced a fault-wide dynamic rupture. During a full stick-slip event, the high sensitivity sensor signals became clipped immediately before rapid sliding ceased. Full waveforms of the acoustic emissions associated with individual stick-slip events were recorded using two passive piezoelectric sensors (OLYMPUS Panametrics V-103) at PZ14 and PZ15. Accurate locations of the non-contact sensor array are shown in Figure 2.2(a) [see also, 167] (red crosses) and the seismic array (black triangles) placed on the top (z = 0 mm) and bottom (z = 50.8 mm) surfaces of the base plate.

2.3 Sample preparation

The surfaces of the PMMA slider and base were machined flat (∼ 0.024 mm / 400 mm), then professionally sandblasted using 40-60 grit Al_2O_3 (440-220 µm) to create roughness profiles [159] similar to those found in nature [149, 43, 44]. Before any reported testing the interface was sheared for a cumulative slip ∼36.1 mm. This ensured the formation of a mature frictional interface; at this point the changes from abrasive and adhesive wear [161] become minimal and do not control friction [18] on the 'mature' faulting surface. Section 6.2 examines the mature surface roughness using a variety of surface profilometry techniques.

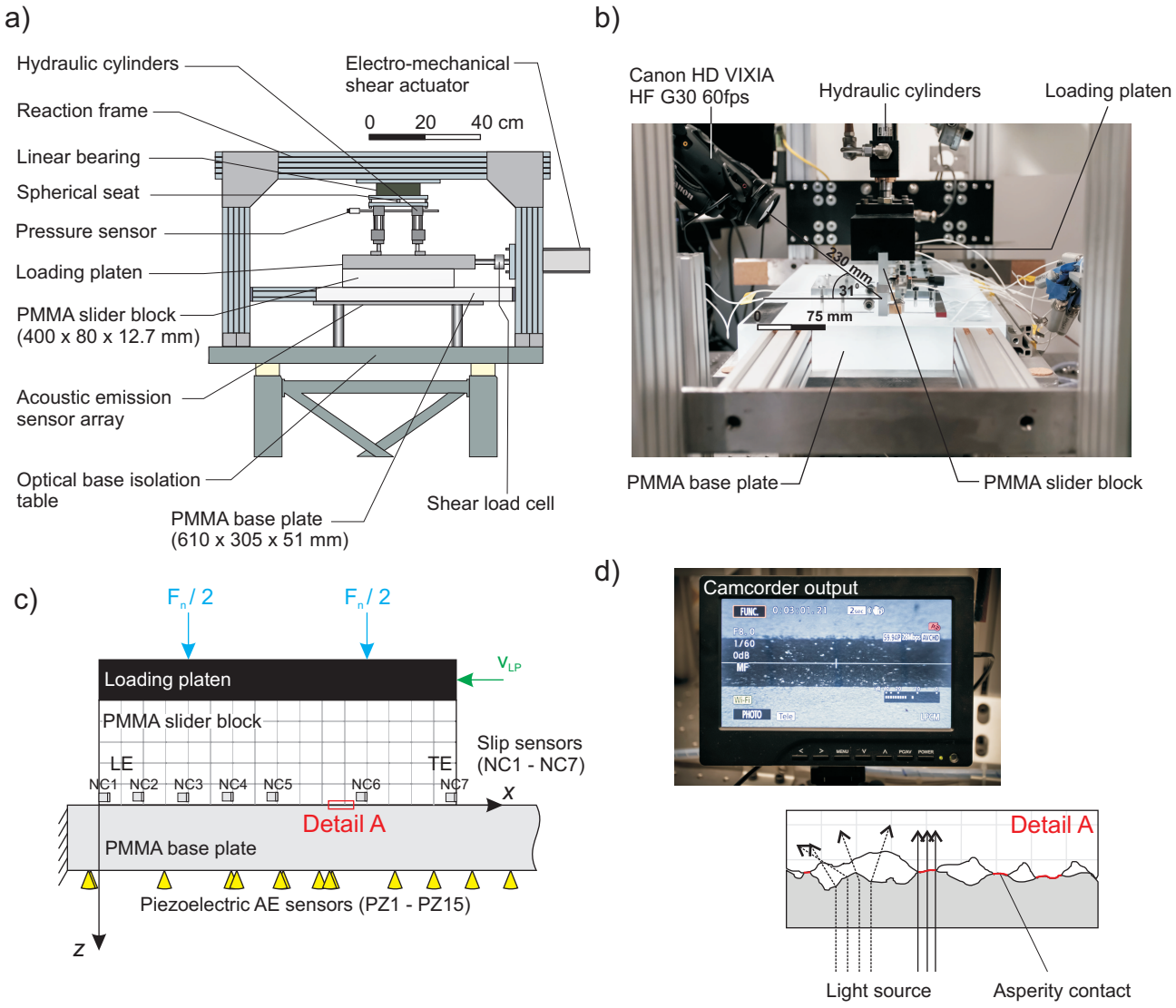

Figure 2.1: **(a)** An overall schematic representation of the direct shear friction apparatus and its major components. **(b)** A photograph of the apparatus showing the location of the video camera in relation to the frictional multicontact interface (MCI). **(c)** General configuration of direct shear apparatus from the side view with general locations for the non-contact eddy current (NC1-NC7) and AE sensors (PZ1-PZ15). These sensors were used to detect dynamic changes as the fault began to fail. **(d)** (top) A photograph of the monitor used to display the video camera images in real time. Asperities appear as bright spots within the darker, interface region. (bottom) A schematic representation of Detail A from (c) depicting the theory which describes the transmission of light through asperities (solid lines) and diffracted light along the void space (dashed lines).

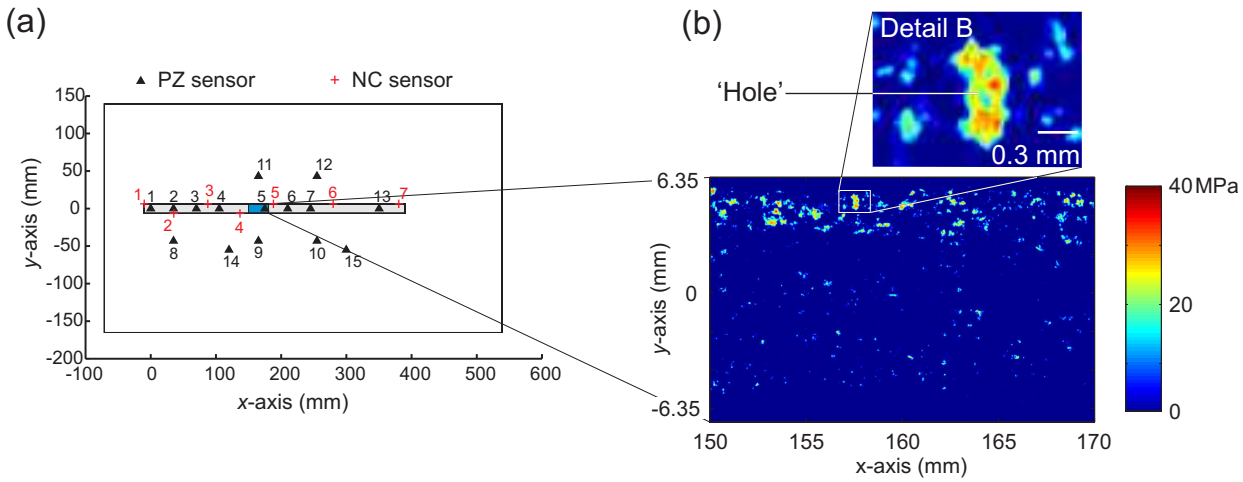

Figure 2.2: **(a)** Detailed locations of the non-contact sensors (red crosses) and piezoelectric sensors (black triangles) with respect to the interface (shaded region). **(b)** A small section of the interface (12.7 mm x 20 mm) showing regions of initial asperity contact along the solid-solid multi-contact interface measured using the pressure sensitive film.

Table 2.1: Material Properties for Polymethyl methacrylate (PMMA)

Density, ρ (kg/m^3)	Shear Modulus, G (MPa)	Young's Modulus, E (MPa)
1180	2277.1	6011.4
Poisson's ratio, ν	P wave velocity, C_p (m/s)	S wave velocity, C_s (m/s)
0.32	2700	1389.1

2.4 PMMA properties

A glassy polymer, polymethyl methacrylate (PMMA) was used as an analog for a ductile rock/rock interface [see e.g., 182, 170, 63, 26, 156, 21, 111, 115, 121, 107, 105, 173]. Poly(methyl methacrylate) is a glassy polymer [11] with physical characteristics at room temperature as follows: density ρ = 1180 kg/m^3, shear modulus G = 2.27 GPa [158] and a Poisson's ratio of ν = 0.32. The body and shear wave velocities are 2700 m/s and 1390 m/s, respectively. Using a digital scanning calorimeter (DSC) we determined the glass transition to be T_g = 114 ^{o}C. The rigidity of the sliders was $k_{slider} \approx (Area/h) \cdot G$ = 144.6 N/µm with a mass $M \sim$ 5.24 kg (including rigid loading platen). Material properties are also shown in Table 2.4 for clarity. We determined the above values independently; they fell within the range of values for PMMA material properties that can be found in the literature [11, 34].

2.5 Microscopy of asperity surface

Full asperity surfaces were initially visualized using light microscopy (dark field illumination) at less magnification. To reconstruct the asperity, multiple images were stitched together manually in an image processing software. Two different optical profilometers (using white light interferometry) were use to characterize the surface roughness at different length scales. For longer wavelengths (millimetric), a Nanovea PS50 Profilomter with a 3000 µm optical pen was used. Scans sizes were 25 mm x 13 mm with 10 µm spatial resolution and 0.5 µm height resolution. For shorter wavelengths, higher magnification (micron length scales) roughness measurements were required. Non-contact interferometry measurements were performed using the ADE MicroXAM-100 Optical Profilometer. The non-contact profilometry provided height measurements (0.01 µm resolution) over a scanning area of 256 µm x 196 µm (1 µm spatial resolution) in the x- and y -directions, respectively.

2.6 Photography of interfacial asperities

Dynamic changes along contacting asperities during the premonitory phase were measured using a similar technique to Dieterich and Kilgore [64]. The unique setup and transparent properties of the 'glassy' PMMA allowed us to directly observe the interface during the experiments. Figure 2.1 (b) depicts the location of the video camera (VIXIA HF G30 CMOS) in relation to the faulting plane. The video camera was focused at a 31^o angle to the horizontal and at a distance of 230 mm from the frictional plane. Detail A in Figure 2.1 (d) illustrates the theory of operation [65, 165, 162]; (*i*) two nominally flat interfaces only touch on asperities; (*ii*) the light was transmitted more effectively through these contacting asperities; and (*iii*) light was diffracted through the void space in which no contact occurred. The high definition video camera operated at a video frame rate of 60 fps (Δt_{frame} = 1/60 s $\sim$ 16.7 ms) and images were obtained at a focal length of 3.67 mm. To improve image resolution without the use of digital enhancement, a CANON 58 mm Close-up Lens 250D was attached directly to the camera. The field of view was 10 mm and images are 2136 x 1362 pixels per frame, making the resolution 0.005 mm/pixel ($\sim$5 µm/pixel). No image correction was performed for the optical distortion, instead 200 µm thick lines were drawn along the interface at 5 mm spacing to form a stereographic grid to account for any orthoscopic distortions from the camera, close-up optical lens attachment and light passing through the PMMA sample simultaneously. Through calibration tests (Section 4) I found that the light intensity increased linearly with normal stress levels between $\sigma_n \approx$ 23 to 32 MPa.

2.7 Pressure sensitive film

A FUJI Prescale pressure sensitive film was employed to detect and measure the contacting asperities formed between the interacting surfaces. Raw images of the film is presented in Figure 1.5(b). The pressure sensitive film is polyethylene based and has a thickness b of approximately 90 µm. The film has embedded microcapsules (5 µm resolution) that, when compressed, release ink with colors proportional to the applied pressure ($\pm$ 1.5 Pa resolution). The specific film used in this study is rated for normal pressures between 12 to 50 MPa according to the manufacturer. At stresses higher than 50 MPa the microcapsules do not experience further discoloration and

the intensity is saturated ($I \sim 0.3$ cd). An example of the processed images are shown in Figure 2.2(b). The film is first placed along the fault and compressed between the PMMA blocks where it develops for a period of ~ 900 s. After loading, the film was extracted and digitized using an image scanner (MUSTEK ScanExpress A3 USB 2400 Pro Scanner). Algorithms in MATLAB were created to isolate, size and catalogue all contacting asperities in the static state - under normal load and not subjected to shear. The film was calibrated using a finite element model (FEM) in the commercially available software ABAQUS and the results are presented in section 3.

Chapter 3

Calibration of pressure sensitive film

In this chapter we calibrate a novel pressure sensitive film that characterizes asperities formed along an interface between two bodies pressed into contact. The film was calibrated by performing indentation tests. A (relatively) rigid spherical steel indenter was pressed into the pressure sensitive film resting on an elastic substrate. A numerical finite element (FE) model was constructed and the numerically calculated stress profiles were compared to those given by the pressure sensitive film. These calibrations are more rigorously documented in Selvadurai and Glaser [167].

As mentioned in Section 1.2.1, the manner in which asperities form (equation (1.10)) and fail (equation (1.11)) are not well understood. The ability of the film to characterize the distributions and sizes of asperities on relatively large laboratory scales (~ 4000 mm^2 with ~ 25 µm^2 resolution) is important to better understand the frictional processes controlling the nucleation that occurs during unstable sliding. Additional detail of the normal stress along individual asperities gives a novel insight into the constitutive manner in which they form – previous studies have used the plastic flow asperity model (equation 1.10). Variations in normal stress along contacting asperities (seen using the pressure film) promotes the idea that they may form elastically (or a combination of elasto-plastic). These subtle changes may influence their response when resisting the growth of a shear rupture (seen in Figure 1.4(b)).

3.1 Indentation test

A spherical indenter apparatus was used to test the pressure sensitive film and is shown in Figure 3.1(a). The pressure sensitive film was used to measure the normal stress profiles caused by pressing the spherical steel indenter (radius R = 9.5 mm) into the pressure film that was laid freely on top of a 50.8 mm thick PMMA base plate. The PMMA substrate had a Young's modulus E = 6.0 GPa [34] and a Poisson's ratio ν = 0.32 [11]. The apparatus was capable of delivering a normal force F_n from 0 to 70 N (compression), which was measured using an in-line load cell (ELPF-T3M-500N). A new piece of pressure sensitive film was used for each indentation test. Once the film became discolored it no longer had the ability to measure a lower normal stress (the discoloration of the film is irreversible). The pixel color is representative of the highest level of stress that the pixel sustatined during a test. A small section, 5.5 mm x 6.1 mm, surrounding the discolored contact patch was digitized using an HD scanner (MUSTEK SE A3 USB 2400 Pro) at 24-bit resolution with RGB color. Once digitized, the image was imported into MATLAB [114] and each

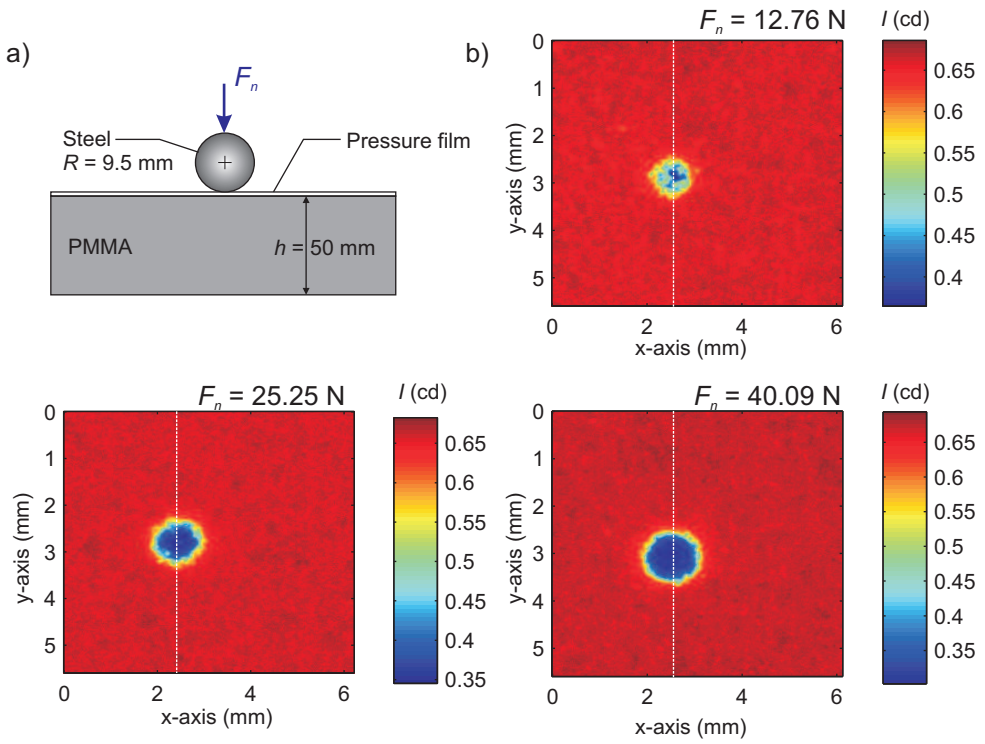

Figure 3.1: **(a)** Indentation test configuration used to calibrate the pressure sensitive film. **(b)** Digitized images of the pressure sensitive film for various levels of normal force applied through the steel indenter. Digitized images were converted to luminous intensity and had an absolute range of 0 to 1 candelas (cd).

pixel converted from an RGB color scheme to the luminous intensity color scheme [73]. Luminous intensity is an SI photometric measurement unit that has a value between 0 to 1 candelas (cd). This metric refers to an average measurement of light intensity across the visible spectrum and is known as *photometry*. Photometry was also employed for images obtained from the video camera that studied dynamic changes of light transmitted through asperities during nucleation (Section 4). Figure 3.1(b) shows the luminous intensity obtained for three indentation tests at $F_n \approx 13$, 25, and 50 N. The brighter region (outside the contact patch) has a higher value of I $\sim$ 0.65 cd while the darker contact region ranged from $I \sim 0.3$ to 0.6 cd.

3.1.1 Numerical modeling of indenter into elastic halfspace

To better understand the light intensity profiles shown in Figure 3.1(b) an axisymmetric, 2-dimensional finite element model was created using the commercially available ABAQUS software. The model excluded the effects of the film and assumed frictionless contact between the rigid indenter and PMMA substrate. At room temperature ($\sim$ 25 ^{o}C), we do not expect PMMA to yield (or soften) until $\sim$ 78 MPa [11]; a linear elastic model was therefore chosen. The deformations were modeled as classical Hookean isotropic elastic [177]. The incremental elastic strains are

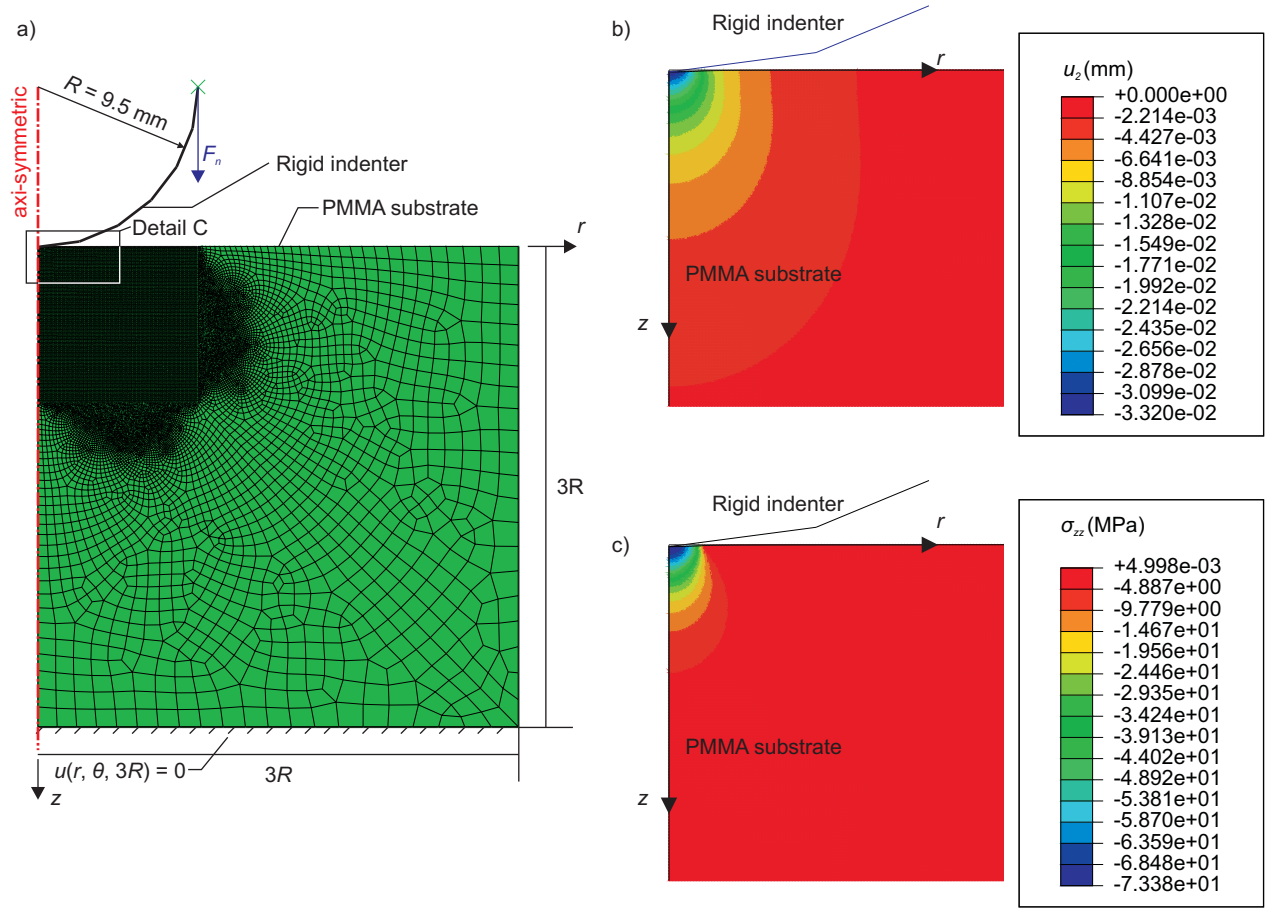

Figure 3.2: **(a)** Numerical model used to model the pressure distributions measured by the pressure sensitive film. **(b)** Displacements in the z-direction ($u_z = u_2$) and **(c)** normal stress (σ_{zz}) from Detail C in part (a). The results shown in (b) and (c) are for an applied normal force of F_n = 49.74 N.

given by,

$$d\epsilon_{ij} = \frac{d\sigma_{ij}}{2G} - \frac{\lambda^* \cdot d\sigma_{kk}\delta_{ij}}{2G(3\lambda^* + 2G)}, \tag{3.1}$$

where λ^* is the Lamé's first parameter, G is the shear modulus and summation over the repeated indices is implied. The model is composed of 46,687 quadratic elements (CAX4R) and was refined to a length scale of 100 µm in the region of contact. The model and boundary conditions are shown in Figure 3.2(a). Figure 3.2(b) shows the z-direction component of displacement ($u_z = u_2$) from Detail C in Figure 3.2(a). Figure 3.2(c) shows the normal stress component (σ_{zz}) from Detail C in Figure 3.2(a). The results in Figures 3.2(b) and (c) are for an applied normal force F_n = 49.74 N.

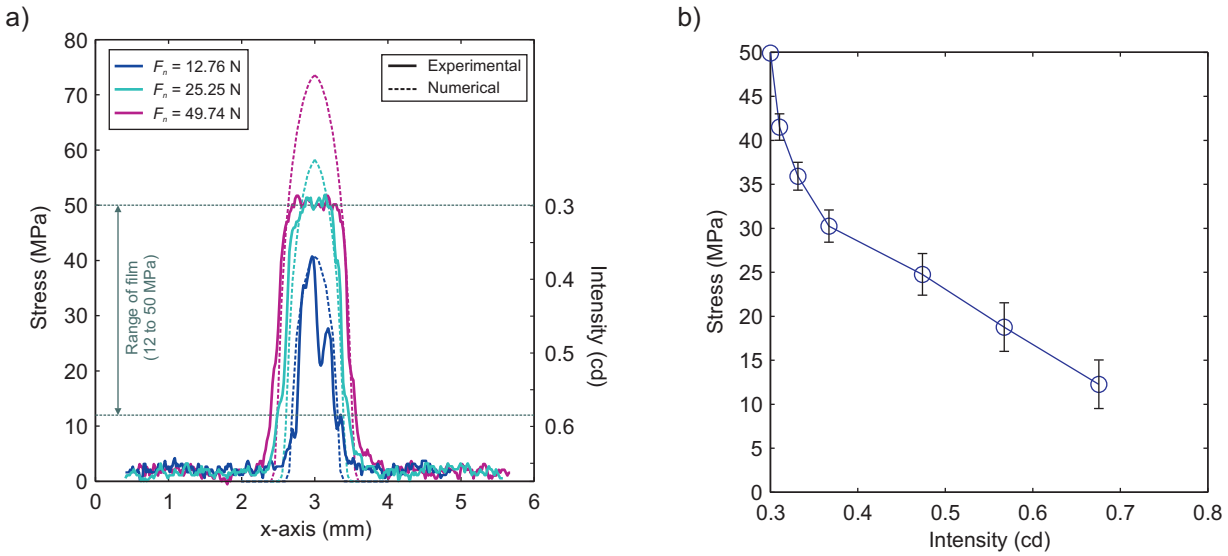

Figure 3.3: **(a)** Comparison of normal stress distributions from experimental pressure sensitive film (solid lines) and the numerical model shown in Figure 3.2 (dashed lines) for various normal loads. **(b)** The relationship between normal stress calculated numerically and the light intensity measured experimentally. The error bars represent spatial errors between the profiles.

3.1.2 Numerical modeling versus experimental observations

The distribution of pressures calculated using the numerical model are shown in Figure 3.3(a) for normal loads of $F_n \approx 13$, 25, and 50 N (dashed lines). Transects were drawn through the centroid of the contact region in the experimental measurements obtained from the images in Figure 3.1(b). The solid lines in Figure 3.3(a) show the experimental profiles of light intensity from these transects (see right hand axis for the corresponding measurement). The film was saturated at a light intensity of I=0.3 cd; this corresponds to a normal stress of 50 MPa, which was expected from the manufacturer's specifications. The error between the experimental and numerical stress profiles were calculate at a normal stress of 12 to 50 MPa. The percentage error in the normal stress profiles ranged from -5 % to 6.6 % at 12 MPa and ranged from -7.7 % to 0 % at 50 MPa. The relationship between light intensity and normal stress is shown in Figure 3.3. The error bars were determined by examining the error in the profiles of four independent indentation tests at each load level shown in Figure 3.1(b). The general shape of this relationship agrees with the manufacturer but was offset in the x-direction. This may have been due to ageing of the film; the manufacturer warns that the film becomes slightly darker with time.

3.1.3 Repeatable usage of the pressure sensitive film along a frictional interface

Using the calibration data curve in Figure 3.3(b) we mapped the interfacial distributions of asperities. An example of the contact measurements for a mature surface is shown in Figure2.2(b) with a magnified asperity in Detail B. Due to the static nature of this measurement and the inher-

ently dynamic nature of the test, the pressure sensitive film was removed from the interface prior to the application of a shear load. This study does not focus on a film-mediated sliding surface. Once the film was extracted from the interface, it was scanned to a spatial resolution of 5 μm and processed using MATLAB [114] image recognition algorithms.

Five algorithms were used to process the film and calculate the normal stress from the light intensity measurements: I_CONVERT_TO_STRESS.m, II_EQM.m, III_ANALYZE_ASPERITIES.m, IV_DISCRETIZE.m and Calibration_curve_good.m. These are given in Appendix B (with annotations) and should be applied in chronological order. Scripts are capitalized as opposed to the functions.

These algorithms first convert the scanned image (tagged image format file, TIFF) to normal stress using the calibration curve calculated in Figure 3.3(b). A lower threshold contact stress value was obtained in an iterative manner [164]. Two assumptions were made: contact occurred only along the x–y plane, and the force on each pixel (pixel area $\times$ pixel stress) was exactly outwards normal to the faulting plane. For all pixels experiencing stresses above the threshold, a total reactive force F_r was calculated. The threshold was then varied iteratively and lowered until F_r balanced the applied far-field load, i.e. $F_r = F_n$. Using the stress threshold, the image (in units of MPa) was converted into a binary image (above and below the stress threshold). All the pixels below the stress threshold were given a value 0 and those above were given 1. The MATLAB function *regionprops* then returns the properties of the discontiguous regions defined by the asperities. While many properties were determined (e.g. eccentricity, orientation, solidity, etc.) only a few properties that we deemed to be important to these frictional studies were included. We were able to accurately measure the asperity contact area and normal stress, including mapping of the actual size, shape, and spatial distributions observed over the entire fault [168]. The total contact area is the sum of all pixels above the stress threshold.

3.2 Determining changes in interfacial normal stress due to repeated loading

When using the pressure sensitive film, a major goal was the accurate and consistent measurement of the contacts along the fault. The film was not used during sliding; it was removed prior to application of shear loads to the fault. It was important to be able to re-index the fault accurately to an original datum location, between the slider block and base plate, after the film was extracted to ensure that the asperity information obtained from the film was maintained on the now solid-solid interface. To do this, small micrometer adjustment screws (accuracy $\pm$ 1.27 μm per revolution) were used for the x- and y-position adjustments [see 164].

As a test of repeatability, the slider block was indexed to within $\pm$ 2 μm in the y-direction and $\pm$ 5 μm in the x-direction of the base plate on three separate occasions. For each test an indentical load was applied and the film was used to characterize contact. For the results shown in Figure 3.4, the interface was subjected to a nominal interface pressure of 3.5 MPa, held for 60 seconds while the strip of pressure sensitive film was sandwiched along the full length of the interface. The relative humidity and temperature of the room were 35% and 21.5^{o}C, respectively, and remained constant for the duration of these tests. Figure 3.4 shows a detailed view of the normal stresses at two randomly chosen locations on the interface for the three consecutive tests (A, B and C). The low stress (12–17 MPa) contact areas varied by $\sim$14% due to loading. These changes occurred over

length scales of approximately 100 μm. Regions displaying higher stress (37.8–50 MPa) displayed a spatial variability at scales of approximately 20 μm. Error in recreating identical contact patches may be due to mundane experimental errors and surface roughness, which controls normal stress distribution [80, 2], an is defined by multiple roughness parameters [133]. The effect of roughness on the formation of asperities and their subsequent effect on preparatory seismicity will be discussed later. From the images seen here we see that at larger spatial wavelengths (scales of $\approx$ 100 μm) the general shapes of the asperities appear to be conserved quite well.

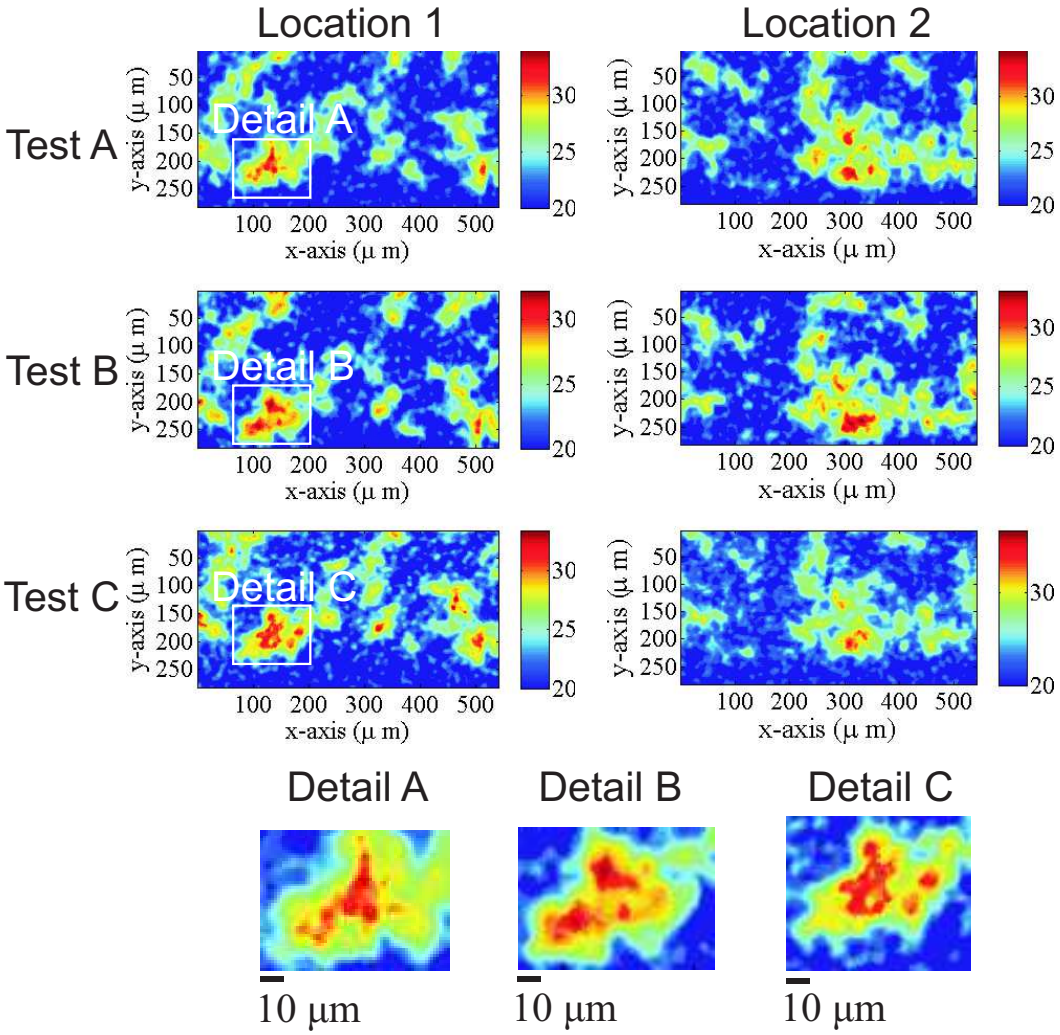

Figure 3.4: Results from three successive normal loading tests where a medium range pressure sensitive film was placed in a sand blasted PMMA-PMMA interface. Samples were loaded normally, to approximately the same nominal pressure (3.5MPa), for $\approx$ 60 seconds. Tests A, B and C were carried out in chronological order and the positioning of the top slider with respect to the base plate was done using the eddy current sensor array and fine threaded screws. Detailed views of two randomly chosen locations along the interface are presented (normal stresses are given in MPa). Each image is composed of approximately 100 x 200 pixels (image resolution $\approx$ 5 μm).

Chapter 4

Asperity Photometry

In this chapter we report on the use of a video camera (see Figure 2.1) to measure light transmitted when two transparent bodies come into contact. Asperities must form via elastic, elasto-plastic or fully plastic interactions (Section 1.4.2) but the manner in which they form is not well understood.

As mentioned in Section 2.6, asperities formed along a fault transmit light through the base plate to the slider block and then an image is captured by the camera. Asperities transmit light more easily than the void space making them appear brighter. In the first part of this chapter we employ similar digital techniques to those used for the pressure sensitive film; i.e. digital image processing [73, 114], is used to map the asperities present in the frame of the video camera. We examine how the asperities react to an incremental increase in the normal load F_n. We then examine the level of light intensity transmitted the through asperities and compare this to the normal stresses measured using the pressure sensitive film at identical locations on the fault and with the same applied normal loads F_n. We found that the light transmitted was proportional to the average normal stress on larger asperities. The majority of the findings and techniques presented in this chapter have been documented in Selvadurai and Glaser [167].

4.1 Interfacial measurements of transmitted light using photometric methods

As mentioned in section 2.6, we used a video camera to monitor the light transmitted through contacting asperities in the direct shear experimental configuration. Figure 4.1(a), shows an unprocessed image taken along the interface. The interface appears darker and this section small populations of bright asperities can be observed. The edges of the image are distorted due to the aperture effect of the lens. We focused our analysis on the portion of the image in the red box highlighted in Figure 4.1(a).

4.1.1 Variations in normal load and its effect on local luminous intensity

A test was performed to analyze the light transmitted through asperities due to an increased far-field normal force F_n in the direct shear setup shown in Figure 2.1(a). The normal force was varied incrementally in a step-like manner as seen in Figure 4.1(b). At each level of normal force a

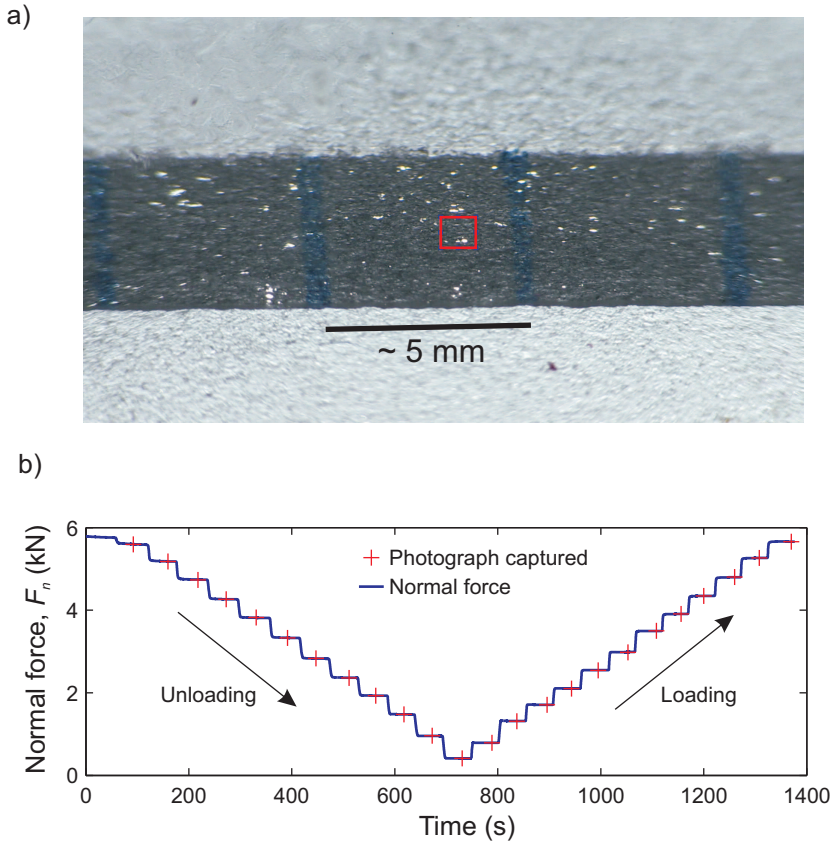

Figure 4.1: **(a)** An unprocessed image (2136 x 1362 pixels) from the video camera focused on the interface (darker region). Within the dark region are small bright regions that are asperities which transmit light more easily. **(b)** Test performed to measure the changes in light intensity and its relation to the applied normal force F_n.

2-second video (i.e. 120 picture frames) was captured and is indicated by the red crosses in Figure 4.1(b). The hypothesis is that as the far-field normal force increases so does the normal stress at the junction-level of the asperity. The closure of the asperity due to increased normal stress allows greater transmission of light. The normal force was first unloaded from $F_n \sim 5.8$ kN to 0.4 kN and then reloaded back to $F_n \sim 5.8$ kN. A total of 12 steps were taken for both the loading and unloading portions of this experiment. The central frame of the 2-second video was used in the following analysis. The raw image captured from the camera had a RGB color scheme and was stored in the tagged image file format (TIFF). The color was converted to luminous intensity I in the same manner as was done for the pressure sensitive film (Section 3.1). Identical algorithms were used for the pressure sensitive film to process the video camera images (see Section 3.1.3 and Appendix B for the algorithms themselves).

4.1.2 Asperity growth with step-like increase in normal force using photometric methods

We focused on the small section of the interface shown in the red box of Figure 4.1(a). The threshold for light intensity was set to I_{thresh} = 0.5 cd. We first examined the number of pixels above the threshold versus the applied normal force F_n. We believe that the absolute number of pixels is not an indication of area since the images are taken at an angle of $\sim 310^o$. However, we expect that the sum of light intensity above I_{thresh} is related to a projection of the real contact area. Mapping the distorted picture to an x-y frame was done by Selvadurai and Glaser [165] using an envelope mapping technique and should be investigated in future work.

In Figure 4.2(a), we show how a small population of asperities formed in relation to increased normal force applied in a stepwise fashion (Figure 4.1(b)). Within the highlighted region, the image processing algorithm allowed us to measure: *i*) the number of contiguous regions (i.e. the number of asperities) above I_{thresh}, (*ii*) the number of pixels in each of these contiguous regions and (*iii*) the distribution of light intensity within each region. To eliminate any background noise, an asperity was defined as a contiguous region if it had a minimum of 10 pixels with luminous intensity above the threshold I_{thresh}. The inset images in Figure 4.2(a) are snapshots of the highlighted region for respective levels of applied normal force F_n. The study of asperities using their transmitted light intensity and our ability to catalogue them individually using post-processing software has many benefits and can provide a number of interesting metrics to better understand the random process models describing approaching rough surfaces [e.g., 133, 146, 145].

Since the seminal paper by Greenwood and Williamson [78], the study of asperity formation between randomly rough surfaces (GW model) has been extensively employed in numerous engineering and scientific endeavors. As mentioned in Section 1.4.5, Greenwood has recently come forward [77, 76] criticizing some of the assumptions made in the GW model and recent works. The field of tribology (i.e. the science and engineering of interacting surfaces in relative motion) is most interested in better understanding these key criticisms. One critical assumption of the GW model is that asperities form independent of each other. The spacing between larger asperities is great enough that they do not interact as the normal force F_n is increased. While interaction was believed to happen only when higher normal loads were applied, in truth, the process of asperity interaction is seen as prevalent. Studying the additional stresses introduced by the elastic interactions of asperities through the substrate are becoming an important topic [145, 36]; the more recent studies on this subject are primarily computational interpretations [45, 52, 2, 150, 184] while experimental studies [101] are at the early stages of development.

In Figure 4.2(b), we show the potential application for further experimental studies of asperity populations (and their interactions) using the photometric tools described above. In Figure 4.2(b), we examine the average light intensity $\bar{I}$ versus the number of asperities N. As the normal force was increased the asperity population is either in (*i*) a 'locked' state, where no new asperities are formed but the intensity increases or (*ii*) a 'growing' state, where new asperities are formed and the average light intensity over the population decreases.

Throughout normal loading of this small asperity cluster (Figure 4.2(a)), we see that the sum of pixels increased (mostly linearly) as F_n was increased. Examining the number of asperities forming in this cluster shows that growth, and formation of new asperities, is highly non-linear; clusters seem to form dependently based on constraints *i* and *ii*. While this measurement is preliminary, it demonstrates a potential method for increasing our tribological understanding of how

asperities are forming in the laboratory. The processes (elastic, elasto-plastic or fully plastic) are important in understanding the constitutive response of single asperities or local clusters of asperities. As mentioned in section 1.4.1 asperity(ies) form due to two constitutive responses (equations (1.10) and (1.11)). The experimental methods described here may provide insight into how asperities form due to increases in normal load (equation (1.10)). Futhermore, we only describe increasing normal force but the capabilities of asperity photometry increases when we are able to study effects from both normal and shear loadings during dynamic loading (albeit limited to the frame rate of the camera).

4.2 Combining pressure film and photometric measurements

We use the now calibrated pressure sensitive film (Section 3) to examine any relationship between luminous intensity across an asperity junction using the photometric methods described in the previous section. We employed the pressure sensitive film in the direct shear apparatus in the same manner mentioned in section 3.1.3 at various normal load levels shown by the red crosses in Figure 4.1(a). For each load level the fault was positioned to a datum location, the film was placed along the fault and the appropriate level of normal force F_n was applied. A new strip of pressure sensitive film was used at each load level. The pressure sensitive film was developed for t_{hold} = 900 s and then the fault was unloaded and the film was carefully extracted and digitized. The calibration used in section 3.1.2 was applied to determine the normal stress field along the fault. The frictional fault was carefully re-indexed to the same location using the eddy current sensor array and fine threaded screws [164], and loaded at the same normal load for an identical amount of time. At this point, photographs of the interface were taken at the central region of the frictional fault. We avoided the end regions of the interface (i.e. x = 0 to 100 mm and x = 300 to 400 mm) to prevent the combination shear and normal stress conditions that arise from the direct shear configuration [21, 103].

In Figure 4.3, we present a pre-processed photograph of the interface (Figure 4.3(a)) and the post-processed image of the same location using the pressure sensitive film (Figure 4.3(b)) for the same applied normal load F_n. The three lines, physically drawn along the interface (i.e. L1, L2 and L3), were used to construct a grid (white dashed lines) along the interface that accounted for the orthoscopic distortions imposed from the camera, additional lens and the PMMA slider sample itself. This grid was superimposed over the pressure film measurements in Figure 4.3(b) and referenced using the lines L1, L2 and L3. Within the grid, two locations are highlighted in the pressure measurements (Figure 4.3(b)) using a yellow and red box. The pressure sensitive film measurements were distorted using an image processing software (COREL DRAW X4) so that the distorted coordinate system matched those from the photographic images. In Figure 4.3(c) locations where light is highly transmitted (in the photographic frame) are compared to locations where the normal stress appears to be higher (from the pressure film measurements). Not all regions exhibiting high levels of normal stress were coincident and this was most likely due to experimental error and our inability to perfectly recreate the interface (see Section 3.1.2).

4.2.1 Calibration of luminous intensity to normal stress along larger asperities

A total of 40 asperities that both transmitted light and had simultaneous film measurements of normal stress were analyzed for the same far-field normal load of $F_n \sim$ 5.6 kN. These asper-

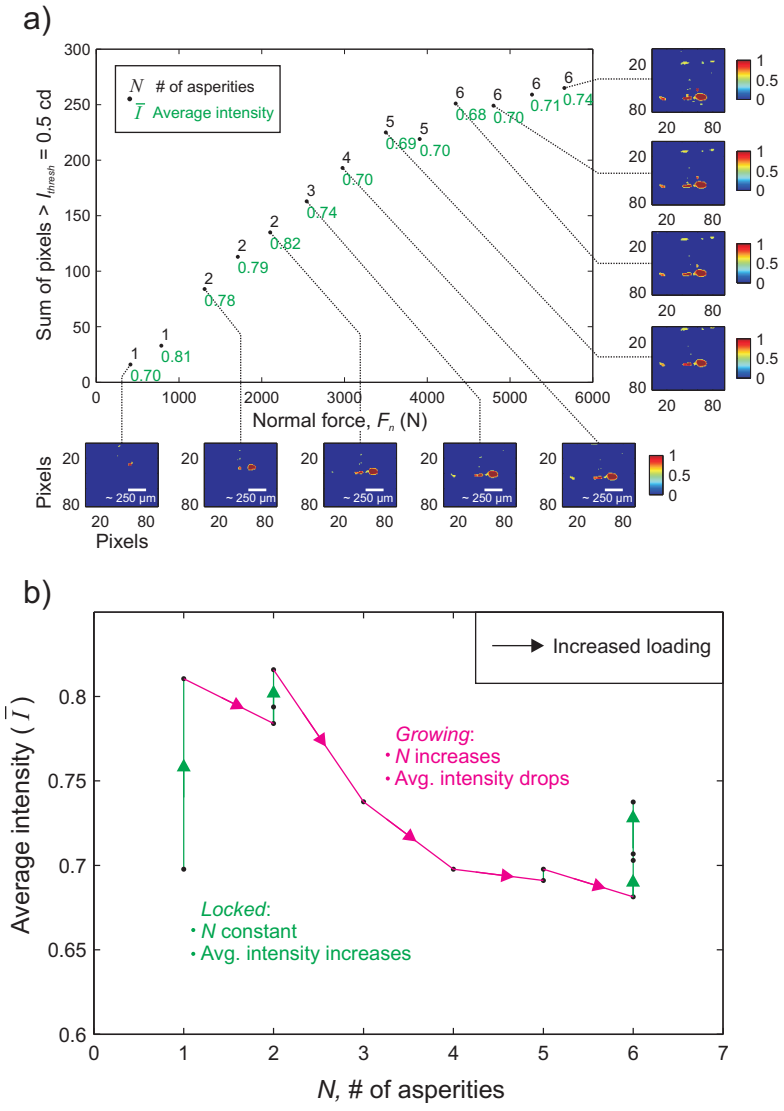

Figure 4.2: **(a)** Total pixels above the threshold light intensity I_{thresh} versus the applied far-field normal force F_n. The images along the axes are the processed images from the red box displayed in Figure 4.1(a) at various normal loads. For each loading step, the number of asperities N (black value) were calculated, using the image detection algorithm, and the average light intensity $\bar{I}$ over those asperities are given in green. **(b)** The average luminous intensity transmitted through the total population of N asperities versus the number of total asperities in the population.

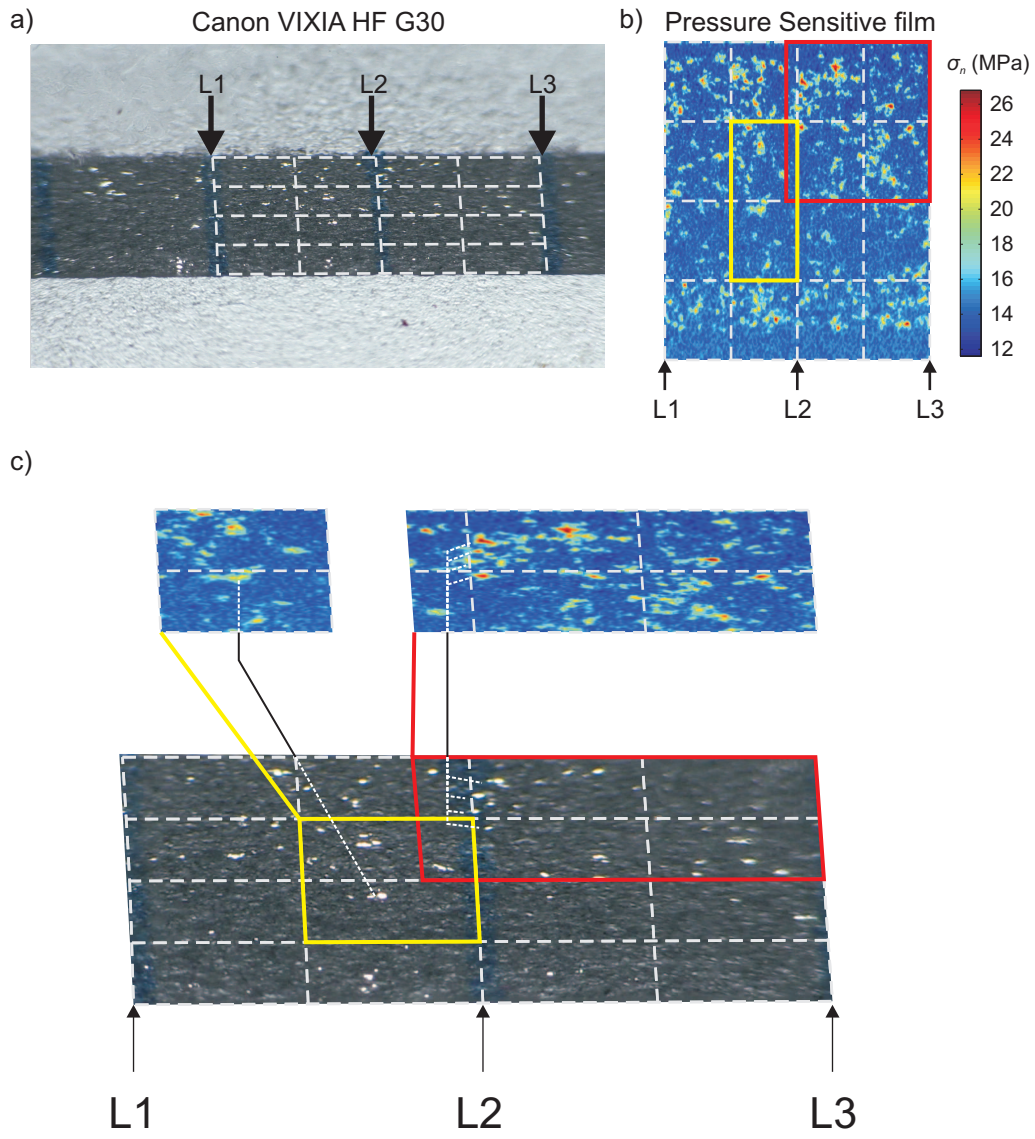

Figure 4.3: **(a)** A still frame obtained from the camcorder at one loading step. A grid was superimposed and followed the lines physically drawn on the interface. The lines L1, L2 and L3 were used for reference. **(b)** Results from the pressure sensitive film (converted to stress) in the same location as in (a). Reference lines L1, L2 and L3 are shown. **(c)** The pressure sensitive film was distorted using COREL DRAW to match the transformed coordinate system in the photograph (top left). In the highlighted boxes, we see that the pressure measurements and the light transmitted occur at similar locations along the grid (connecting lines).

ities were hand-picked since the process of locating identical asperity distributions using both measurement tools was not trivial. Figure 4.4(a) shows the normal stress distribution on a single asperity and the accompanying stress histogram. For the same asperity, we show the photometric measurement taken in Figure 4.4(b) with its accompanying luminous intensity histogram. For each histogram the maximum (red) and mean (black) normal stress and light intensity were recorded. Figure 4.4(c) shows the relationship between the normal stress and light intensity. Both the mean (black) and maximum (red) data points were plotted. Linear estimates of the maximum (R^2 = 0.82) and mean (R^2 = 0.75) relationship between the normal stress and light intensity were plotted. We used the fitted slopes to estimate the relationship between light intensity and normal stress. An increase of 1 MPa in normal stress caused the light intensity to increase 0.05943$\pm$0.0012 cd between the normal stress range of 23 to 32 MPa with an error of $\pm$1.45 MPa within a 95% confidence interval (dashed lines).

In similar studies [63, 64], the light transmitted was assumed to occur only on asperities that formed due to plastic contact, i.e. the stress levels were uniform over the entire asperity in accordance with the plastic contact limit P_f (from Archard [8] and Section 1.4.1). We clearly see in each histogram (Figure 4.4(a) and (b)) that the range varies – a phenomena that is better explained by elastic or elasto-plastic contact. Again plastically formed asperities do not seem to be present as was observed using the pressure sensitive film in Section 3.1.3.

Experimental errors could have been introduced when the pressure sensitive film was extracted; reconstituting identical asperity populations (in order to measure the light transmitted) was not fully achieved. In the author's opinion, more studies to further develop the catalog shown in Figure 4.4(c) are necessary, but this should not detract from the initial observations presented here. (NB: We noticed the light transmitted through the interface did saturate to a single value (I = 1) if too much light was applied through the base plate. As the source light was decreased, light fringes became visible. The sensitivity of the correlation curve to the uniqueness of our direct shear friction apparatus indicates the relationship between light intensity and normal stress should be recalibrated in independently.)

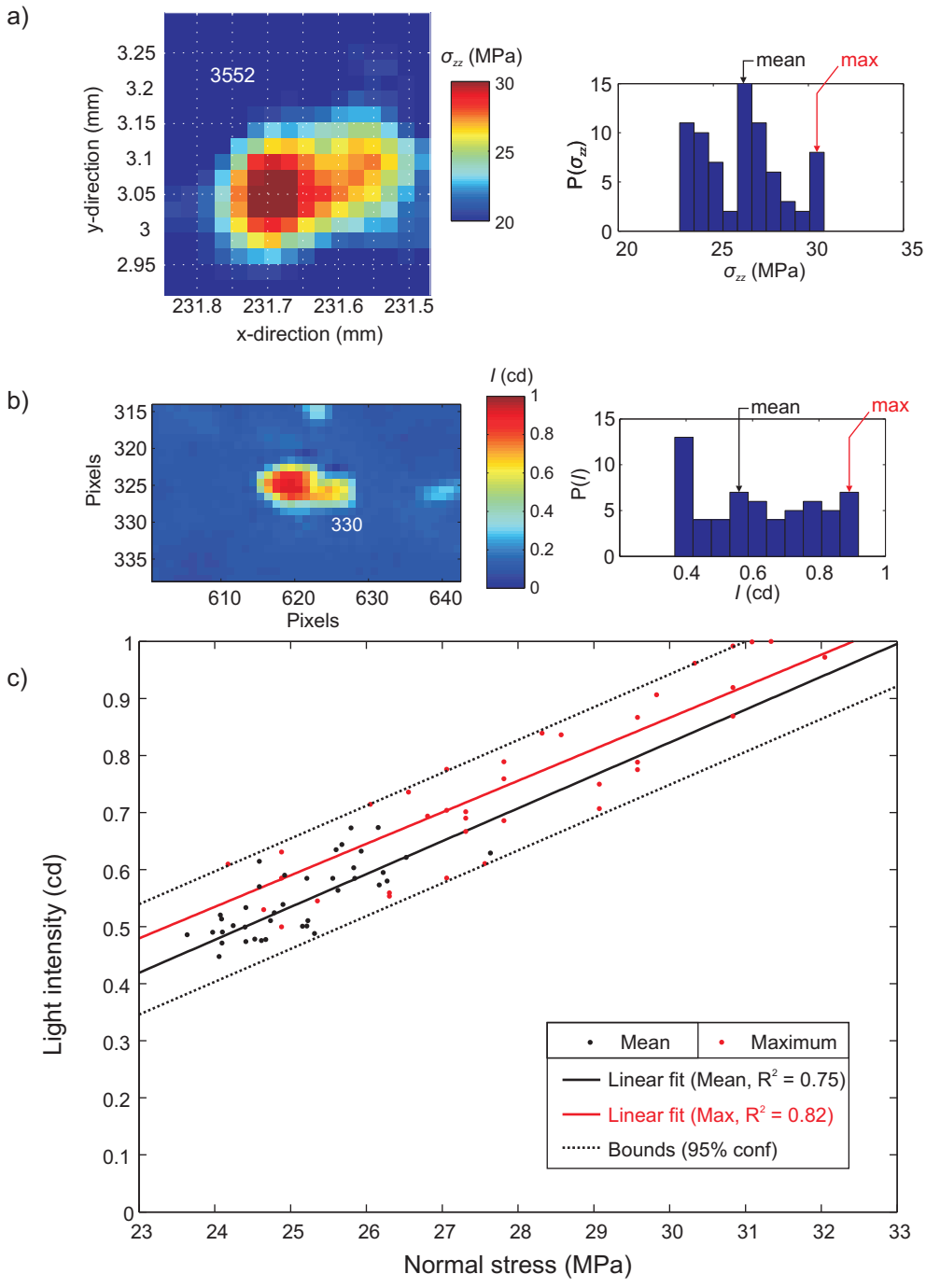

Figure 4.4: **(a)** Normal stress along an asperity measured using the pressure sensitive film (left). On the right is the histogram of the stress for the same asperity. **(b)** Light intensity transmitted by the asperity in (a) measured using the video camera. The histogram for the light intensity is shown on the right. **(c)** The relationship between thenormal stress and light intensity.

Chapter 5

Laboratory direct shear procedure

5.1 Background and motivation

A dry, mature and unlubricated polymethyl methacrylate (PMMA)-PMMA frictional fault was created in the laboratory in a direct shear configuration. The fault was sheared until failure. Prior to failure, slip δ (or the differential motion between the top and bottom surfaces) accumulated non-uniformly in what is referred to as the premonitory phase. During this phase, sliding velocities $\dot{\delta}$ along the interface were slow ($\sim$ µm/s) and also varied along the fault. The shear strain stored in the slider block away from the faulting plane (z direction in Figure 2.1(c)) and that stored along the fault plane (x-y plane in Figure 2.1(c)) was proportional to the amount of slip. Strains increased with higher levels of applied normal force F_n. A 'relatively locked' region resisted premonitory slip and showed a higher density of asperities than neighboring sections. Just prior to failure (milliseconds to tens of seconds) small high-frequency emissions were observed using the piezoelectric acoustic emission sensors. Using standard seismological data processing techniques we inferred that the size of the sources causing these emissions were similar to those of asperities measured using the pressure sensitive film (section 3). Photometric evidence 4 showed that some asperities within the relatively locked region remained in contact throughout the premonitory slip phase. Here we document the procedure used to reproduce the local precursory seismicity during the nucleation of dynamic frictional slip.

5.2 Procedure

5.2.1 Premonitory slip phase to gross fault rupture

Both the PMMA slider and base plate were machined and sandblasted as described in Section 2.3. In order to develop a mature surface the fault was loaded to the maximum normal force F_n = 4400N (corresponding to a nominal normal stress of $\sigma_0 \sim 0.9$ MPa) and the fault was driven slowly (V_{LP} = 0.003 µm/s) until it had accumulated a total of $\sim$ 36.1 mm of slip. The maximum travel of the slider with respect to the base plate was 10 mm (limited by the linear bearing seen in Figure 2.1(a)). The fault was only sheared in the direction of loading and was indexed to the datum location once it had reached its maximum travel distance. During the frictional surface preparation numerous gross fault ruptures were observed ($\sim$ 1 gross rupture / 600 µm of cumulative slip).

Both sides of the fault experienced wear from either adhesion or abrasion processes – ultimately changing the roughness profile. A major focus of this study was to examine precursory seismicity (e.g. foreshocks). Foreshocks only appeared on the mature faulting surface and, therefore, the wearing of the interface itself was not studied here. More detailed observations and a discussion of the mature surface roughness is presented in Section 6.2.

Tests were performed in two phases (Phase I and II) and at four levels of nominal normal force (F_n = 2000 N, 2800 N, 3400 N and 4400 N). Figure 5.1 shows a typical experimental result for a normal force of $F_n \approx 4400$ N. A strip of pressure sensitive film was used to characterize the interface, which was then removed and processed. The slider block was indexed back to its datum location and solid-solid frictional tests were carried out.

During Phase I, the fault, indexed to the datum location, was stress aged [26] for t_{hold} = 900 s using the same level of normal force employed to develop the pressure sensitive film. Phase II consisted of a slide-hold-slide [20, 113, 108, 95] test in which gross fault rupture was created by the far-field movement of the rigid loading platen (see Figure 2.1(c)). The loading platen was driven at a constant velocity V_{LP} = 0.010 mm/s for the tests reported here. This resulted in an increase in shear force (red in figure 5.1(a)) along the interface until instability or gross fault rupture occurred. Gross fault rupture occurred when the nucleation region grew to a critical size L_c given by equation (1.9); at this point slip accelerated and rapid sliding propagated over the entire interface. The term 'gross fault rupture' is also referred to as a global stick-slip event (SS). Stick-slip events were accompanied by a sudden shear force drop (ΔF_s) and a rapid increase in slip ($\Delta \delta_{seis}$) in the direction of the applied shear. Prior to SS, slow premonitory slip accumulated along the fault within a nucleation region, as described in Section 1.3.1. Slip accumulated non-uniformly and the reasons for this will be discussed in more detail in Section 6.3.1.

A total of three SS events were produced in Phase II (SS1, SS2 and SS3). Between each SS event the fault was momentarily held at t_{hold} = 900 s as in Phase I, thus allowing the fault to heal [64]. The arrows in Figure 5.1(a) show when the fault was held during Phase II. Local velocities at each slip sensor were determined by differentiating the decimated slip signal, over 1 second intervals, and applying a low pass filter at 10 kHz. The non-contact sensor trigger (NC trigger in Figure 5.1(b)) had a threshold V_{thresh} = 4 mm/s; this defined the slip rate observed before the fault produced a SS event – once any slip sensors breached this velocity threshold, gross fault rupture always ensued.

5.2.2 High-frequency emissions prior to a gross fault rupture

Figure 5.1(c) shows the slow slip measurements in the premonitory slip phase from sensor NC7 prior to gross fault rupture. Acoustic emission data (blue) was recorded on 15 channels (AE sensors PZ1-PZ15) at 10 MHz in 209 ms blocks using the *Multiblock* setting in the TracerDAQ data acquisition software. The AE amplitude trigger threshold was set to 6 picometers of fault normal displacement. We note that the AE sensors have been absolutely calibrated using the techniques described by McLaskey and Glaser [117, 116]. In Figure 5.1(c), a total of five AE signal blocks are shown. Within these blocks we noticed the presence of high-frequency acoustic emissions between a frequency band of 100 kHz-1000 kHz. We refer to the high-frequency emission as a 'foreshock' (FS). Detail A of Figure 5.1(c) shows some foreshock detections (green stars) for the final AE signal block. A total of 10 foreshocks were detected leading up to this particular stick-slip event (SS3 at a normal load of F_n = 4400 N).

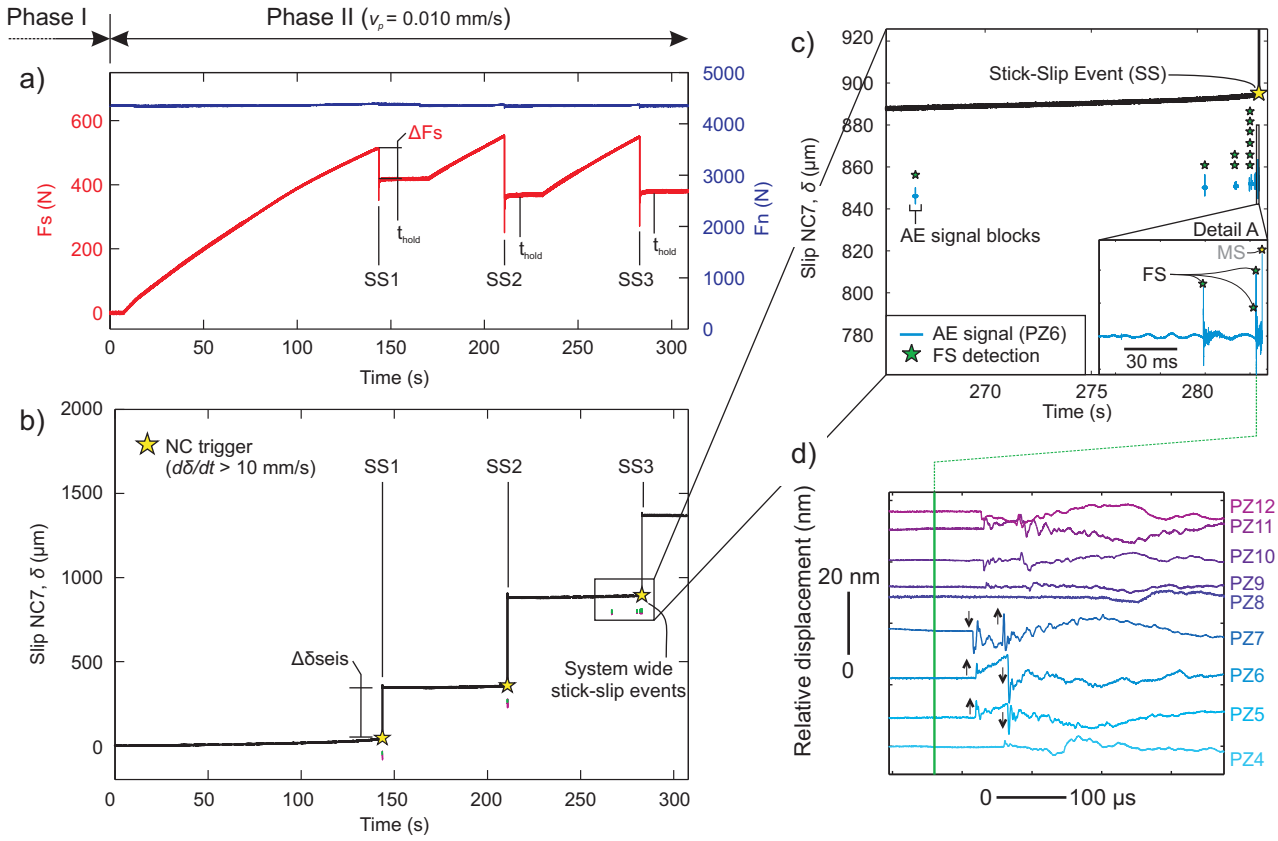

Figure 5.1: A typical result from the direct shear experiment performed at $F_n \approx 4400$ N. The test consists of a holding Phase I and a slide-hold-slide Phase II. **(a)** Measurements of the shear (red) and normal forces (blue) during the experiment. During Phase II, three Stick-Slip Events (SS1, SS2 and SS3) are created by increasing shear until rapid gross fault rupture ensued. **(b)** Slip measurements from sensor NC7 (black) show that stick-slip (SS) instability resulted in a shear force drop and a rapid increase of slip along the fault. **(c)** Enhanced view of slip prior to a SS3 from NC7. Acoustic emission (AE) signal blocks (blue) are shown in relation to the slow slip signal. Timing of the foreshocks for this SS are shown as green stars. In Detail A, an enhanced signal shows the 3 foreshocks (FS) detected in this window before the impending main shock (MS). **(d)** A foreshock, from the sequence shown in Detail A, showing the high-frequency nature of these signals as measured by the acoustic emission arrays (PZ4-PZ12).

5.2.3 Foreshock locations and timing

Figure 5.1(d) shows typical foreshock measurement over the 13 fully calibrated AE sensors. Each foreshock contained high frequency information including pulse-shaped wave arrivals associated with P and S wave phases of the radiated energy [e.g., 40, 89, 86, 3, 180]. Location of the hypocenter and timing of the events were estimated using a least-squares method, minimizing the error between the first arrival P wave information from a minimum combination of 5 sensors. Due to clustering of the foreshocks in the 'relatively locked' region (i.e. from $x \approx 150$ mm to 300 mm) sensors PZ5-PZ7 and PZ9-PZ12 were primarily used for this calculation. Arrival times of the P waves were determined using an amplitude criterion: the average amplitude of the differentiated signal within a small window y_2 (100 samples = 1 µs), was compared to that of a preceding larger window $\bar{y}_1$ (1000 samples = 10 µs). The mean of the larger window $\bar{y}_1$ was subtracted from the smaller window and normalized by the larger window standard deviation σ_1; this accounted for variations among different sensors during different runs, and is given as

$$z_2 = \frac{1}{\sigma_1}\left(y_2 - \bar{y}_1\right), \tag{5.1}$$

where z_2 was the transformed amplitude of the smaller window (standard normal deviate). An event was selected when the value of z_2 exceeded 4. Hypocentral locations were restricted to the fault plane and resolved to an approximate spatial resolution of 1 mm and temporal resolution of 1 µs. The assumption that fracture occurred on the faulting plane (but not off-fault; within the intact material) follows the previous findings on PMMA–PMMA frictional interfaces [128, 115]. We also note that visual microscopy (Section 6.2) did not show any off-plane fractures.

The current analysis that describes the overall size of a foreshock takes advantage of the absolute calibration of the AE sensors [116]. We assumed that the magnitude of a foreshock is related to the maximum peak ground displacements (PGD) occurring within the 100 µs from the first arrival, averaged about piezoelectric sensors PZ5, PZ6 and PZ7 (see figure 5.1(d)). In these tests, the AE sensors measured the fault normal displacements due to the sensor orientation. These sensors were located directly under the relatively locked 'region of interest' of the fault and at hypocentral distances ~ 50 mm from the majority of foreshock locations. At these sensor locations, we expected source-to-sensor attenuation to be minimal for both the amplitude and frequency content [178, 115]. We note that the more remote sensors (e.g. PZ4 in Figure 5.1(d)) were affected by attenuation and should be adjusted using methods similar to those given in McLaskey and Glaser [115]; however, the output of these AE sensors was not considered for the PGD measurements used in this study.

Chapter 6

Experimental results

6.1 Pressure sensitive film

Developing a map of the asperity locations, geometries and stress states along the fault was done using the pressure sensitive film described in Section 3. Asperities are formed due to the interaction of the two rough surfaces (see Section 1.4.5) but the pressure film allows us to know the asperity distribution independent of the surface roughness. These distributions were then used to study the properties of the asperities with a level of detail that was not previously attainable in the laboratory. Ultimately, we believe that the premonitory seismicity (Section 6.4) is directly related to the rapid localized failure of these asperities. Measurements, such as the normal stress and size of the asperity are important in understanding how resistive and prone to seismicity the asperities (or populations of asperities) are in the presence of a slowly expanding nucleation region. An intimate knowledge of asperities and their influence on precursory seismicity may help provide better estimates of seismic hazard in the field.

6.1.1 Asperity formation along the fault under normal loads

Contact measurements obtained from the pressure sensitive film are shown in Figure 6.1(a) for the four levels of applied normal force $F_n \approx$ 4400 N, 3400 N, 2700 N and 2000 N in decending order. Real contacts greater than 0.0448 mm^2 are shown as scaled circular patches with areas proportional to the actual measured contact area, enlarged 20 times for clarity. These larger asperities supported normal stresses above 18 MPa and had areas ranging from A_{film} = 0.0448 to 4.97 mm^2, which converted to an equivalent circular asperity representation, had radii between R_{film} = 0.06 to 1.25 mm. The center of the circular patch was located along the *x*–*y* plane using the geometric centroid of the true contact area calculated using image processing algorithms (see Section 3.1.3). Spatial histograms of the asperity distributions are shown in the margins and discretized into a grid of 2 mm and 0.5 mm along the *x*- and *y*-directions for visual aid. Figure 6.1(b) shows the precursory (foreshock) seismicity in the 'relatively locked' region of the fault (from x = 150 to 300 mm). This region is defined as the *seismogenic* region and is the primary focus of our contact measurements obtained from the pressure sensitive film.

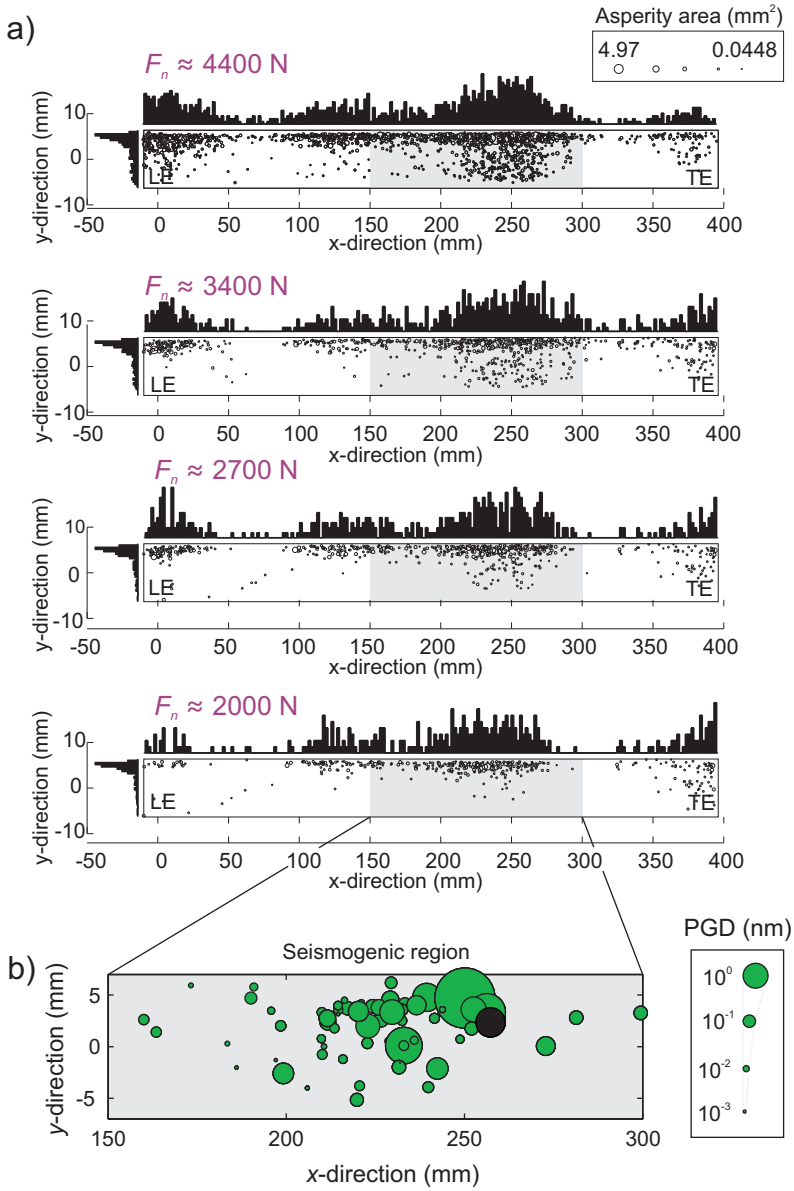

Figure 6.1: **(a)** Asperity contact area at various levels of normal force F_n, measured using the pressure sensitive film. Spatial histograms of asperities larger than 0.04 mm^2 are shown on the x- (discretized into 2 mm sections) and y- (discretized into 0.5 mm sections) margins. **(b)** Full foreshock catalogue from the *seismogenic* section of the fault (x = 150 mm to 300 mm). Sizes of foreshocks (green circles) are proportional to the peak ground displacement (see Section 6.4)

6.1.2 Macroscopic contact properties over multiple asperities

Using the pressure sensitive film we examined the number of asperities N formed in the *seismogenic* zone under various far-field normal loads F_n. We calculated the total reactive normal force F_r supported across the asperities in the *seismogenic* region (gray region in Figure 6.1(b)). The total reactive normal force F_r balancing the normal force in the *seismogenic* region was calculated by summing the reactive force on each i^{th} asperity,

$$F_r = \sum_{i=1}^{N} \bar{\sigma}_i \cdot A_i \tag{6.1}$$

where $\bar{\sigma}_i$ is the average normal stress and A_i is the area calculated using the post-processed pressure film. Figure 6.2(a) shows the linear trend between the number of asperities N (blue circles) and reactive normal force ($N = 0.6582 \cdot F_r$). The real contact area in the *seismogenic* region, i.e. $A_r = \sum_{i=1}^{N} A_i$, increased at 0.059 mm^2 per Newton of increased normal force (R^2 = 0.999). The mean asperity area was calculated by dividing the real contact area by the number of asperities: i.e $\langle A \rangle = A_r/N$. We observed growth of $\langle A \rangle$ as the total reactive normal force was increased (blue squares in Figure 6.2(b)). The average asperity normal stress remained relatively constant $\langle \sigma \rangle = F_r/A_r \sim$ 16.53 MPa and insensitive to the normal force (green triangles in Figure 6.2(b)).

We can quickly examine our interface in the context of the Greenwood-Williamson (GW) model [78]. Using the model we see the expected relationship that the real contact area A_r is proportional to the normal load and independent of the nominal contact area A_0, which also satisfies Amontons second law (see Section 1.4). The average contact radius $\bar{a}^2 = \langle A \rangle / \pi$ increases with the level of applied normal force. The average normal stress remained relatively constant suggesting that growth in average asperity area was likely due to local 'plastic flow'. Using the pressure sensitive film, we measured the plastic flow pressure P_f, or indentation hardness, in two independent ways. If asperities form plastically, the linear relationship between the real contact area and normal force can be used to determine the bulk flow pressure P_f [see 18] and is given as:

$$A_r \simeq (1/P_f) \cdot F_r. \tag{6.2}$$

We can apply equation (6.2) using the results in Figure6.2(a), i.e. $A_r = 0.059 \cdot F_r$. The flow pressure is estimated at $P_f \sim$ 16.95 MPa and is almost identical to the constant average asperity normal stress ($\langle \sigma \rangle \sim$ 16.53 MPa) seen in Figure 6.2(b).

Plastic asperity formation is an underlying assumption in most geophysical studies [e.g. 59]; however, we also see evidence of other contact processes – not simply plastic flow on the asperities. This becomes apparent when we examine normal stress distribution on individual asperities, as shown in Figure 6.3. While bulk features of asperity formation appear to form plastically, at the flow pressure P_f described by the relationships in Figure 6.2, we would expect constant normal stress across individual asperities. This is not the case; as seen from Figure 6.3, the normal stress varies on individual asperities, which complicates our initial plastic understanding. The manner in which normal stress is supported across a foreshocking asperity may determine the radiated seismicity if the shear strength of the asperity is related to the normal stress as described by adhesive friction theory.

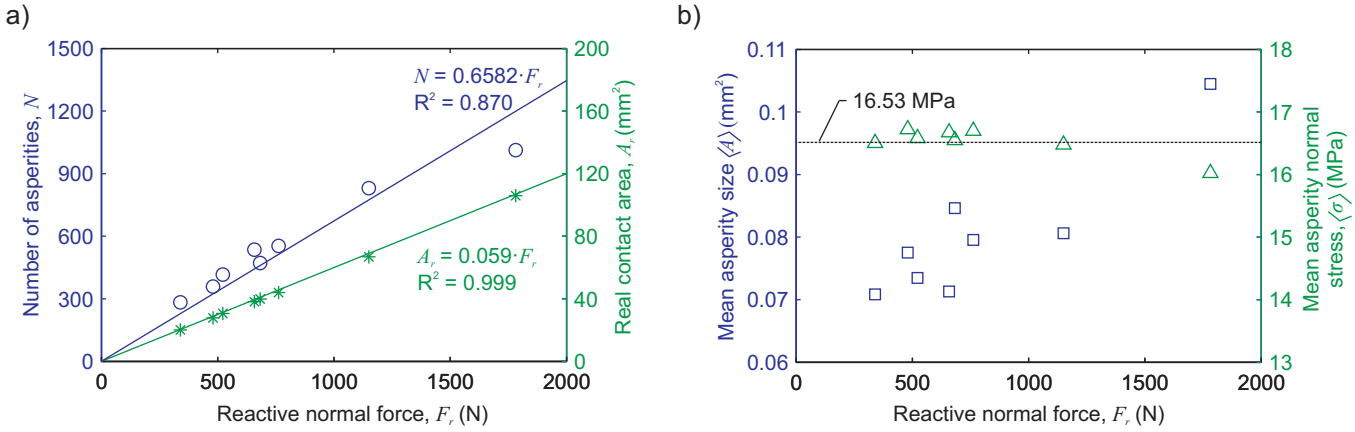

Figure 6.2: **(a)** Changes in the number of asperities N (blue circles) and real contact area A_r (green stars) as the reactive normal force F_r increased within the *seismogenic* region (x = 150 to 300 mm). Reactive normal force was calculated using equation (6.1). **(b)** Changes in the mean asperity size $\langle A \rangle$ (blue squares) and mean asperity normal stress $\langle \sigma \rangle$ (green triangles) as the reactive normal force F_r in the *seismogenic* region was increased.

6.1.3 Local contact properties over individual asperities

The size and location of the asperities formed during the initial contact between the slider block and base plate are shown in Figure 6.1(a). Figure 6.3 shows a section of the interface (x = 270 to 290 mm, y = -2 to 6 mm) for two different far-field normal forces (F_n = 4400 N (top) and 2700 N (bottom)). The inset of each image shows an enlarged view of a few asperities at the two different load levels and the manner in which asperities grew with the application of normal force. As highlighted in Figure 6.3, for each i^{th} asperity we measured the (*i*) the full normal stress field σ_i, (*ii*) the average of the normal stress field $\bar{\sigma}_i$, (*iii*) the asperity area A_i and (*iv*) the coefficient of variation $cv_i = std(\sigma_\mathbf{i})/(\bar{\sigma}_i)$. Null normal stress conditions were prescribed for non-contacting regions as per Persson et al. [148]. We examine individual asperity metrics from a *seismogenic* section of the fault from x = 150 to 300 mm where precursor seismicity was observed.

For each i^{th} asperity, we measured the normal stress field $\sigma_\mathbf{i}$ and found the scalar mean of the normal stress field $\bar{\sigma}_i$ (denoted with the over line) within the *seismogenic* region (x =150 to 300 mm). Catalogs were created at the four levels of applied load F_n. Figure 6.4(a) shows the probability density functions (PDF) of $\bar{\sigma}_i$ for various levels of far-field normal force F_n. The average normal stress level $\langle \sigma \rangle$ was $\sim$ 16.53 MPa and was also plotted. The number of asperities supporting lower levels of normal stress (i.e. $\bar{\sigma}_i < \langle \sigma \rangle$) increased with an increase in the level of normal force F_n. The asperities supporting higher levels of normal stress (i.e. $\bar{\sigma}_i > \langle \sigma \rangle$) did not vary significantly with variations in F_n. It is evident that no single value of mean normal stress (i.e. P_f or $\langle \sigma \rangle$) is sufficient to characterize the distributions of $\bar{\sigma}_i$ on all asperities – as would be the case if the asperities formed plastically. The heterogeneity described by the distributions suggests that asperities form under more complex conditions (e.g. elastic or elasto-plastic). An increase in normal force F_n appears to favor the development of asperities at lower than average normal stress levels.

In Figure 6.4(b) the variations in the mean asperity pressure $\bar{\sigma}_i$ versus the size of asperities for

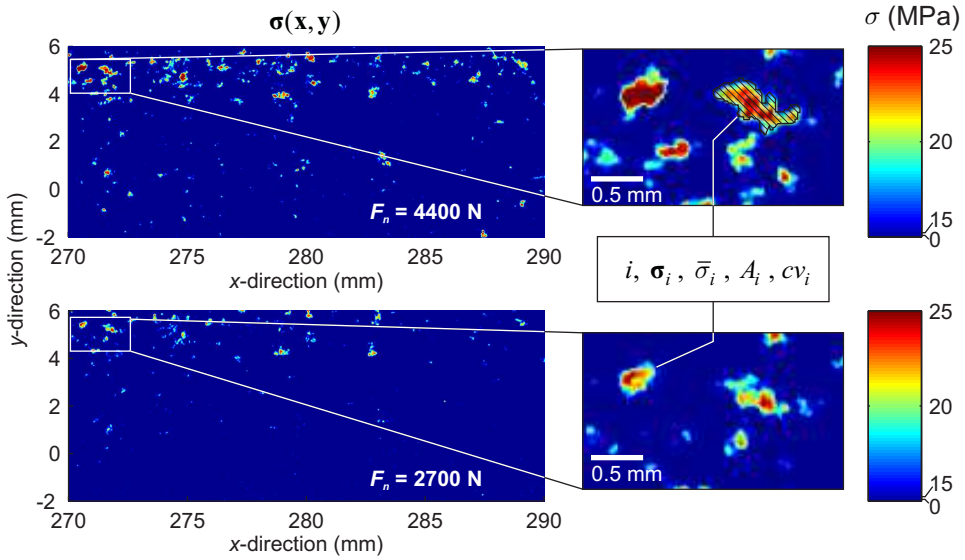

Figure 6.3: Normal stress distributions recorded from the pressure sensitive film for a small section (x = 270 to 290 mm, y = 6 to -2 mm) of the interface at a normal force F_n = 4400 N (top) and 2700 N (bottom). The inset shows how the asperities vary as the normal force F_n is changed over the mature faulting surface. For each i^{th} asperity, we measured the normal stress field $\sigma_\mathbf{i}$ (MPa), the mean normal stress $\bar{\sigma}_i$ (MPa), the asperity area A_i (mm^2) and the coefficient of variation cv_i.

each i^{th} asperity are plotted. The color scheme is indicative of the applied normal force. Foreshock source areas are estimated in Section 6.4.2; their spatial size was determined using Brune's relationship [40] from the AE data. Source dimensions were inferred from the pulse-like time duration of rupture determined from the P and S wave arrivals. The circular source radii of the foreshocks translated into asperity areas and ranged from $A_{FS} = 0.14$ to 3.73 mm^2, which is highlighted by the gray shaded regions in Figures 6.4(b) and (c). The relationship of asperity area versus the mean normal stress formed a cluster of smaller asperities ($A < 10^{-1}$ mm^2) that supported lower levels of normal stress ranging from $\bar{\sigma}_i = 14.9$ to 18.9 MPa. Smaller asperities were also more abundant, making up $\sim$ 57 % of all i^{th} asperities formed for all applied load levels. Larger asperities ($A > 10^{-1}$ mm^2) supported higher levels of normal stress ranging from $\bar{\sigma}_i = 15.4$ to 20.6 MPa.

A similar clustering of asperity sizes versus the coefficient of variation cv_i is seen in Figure 6.4(c). Asperities with lower values than $\bar{\sigma}_i$ showed a more uniform normal stress distribution (i.e. lower coefficient of variation). Larger asperities tended to have a higher coefficient of variation, which describes a higher degree of normal stress heterogeneity. Figure 6.4(c) indicates that both large and small asperities exhibited a broad range of variation cv_i. However, asperities smaller than $A_i < 0.14$ mm^2 had an average $cv_i \sim 0.072$ (7.2 %), while larger asperities $A_i > 0.14$ mm^2 had an average ~ 0.133 (13.3 %).

Figure 6.4(d) examines the coefficient of variation cv_i in terms of the average asperity normal stress $\bar{\sigma}_i$, which is described by a linear relationship (R^2 = 0.9017). The reason for the increased dispersion on highly stressed asperities is due to the local contact processes of asperities formed between the rough-rough interfaces; we will discuss this in more detail in a subsequent section.

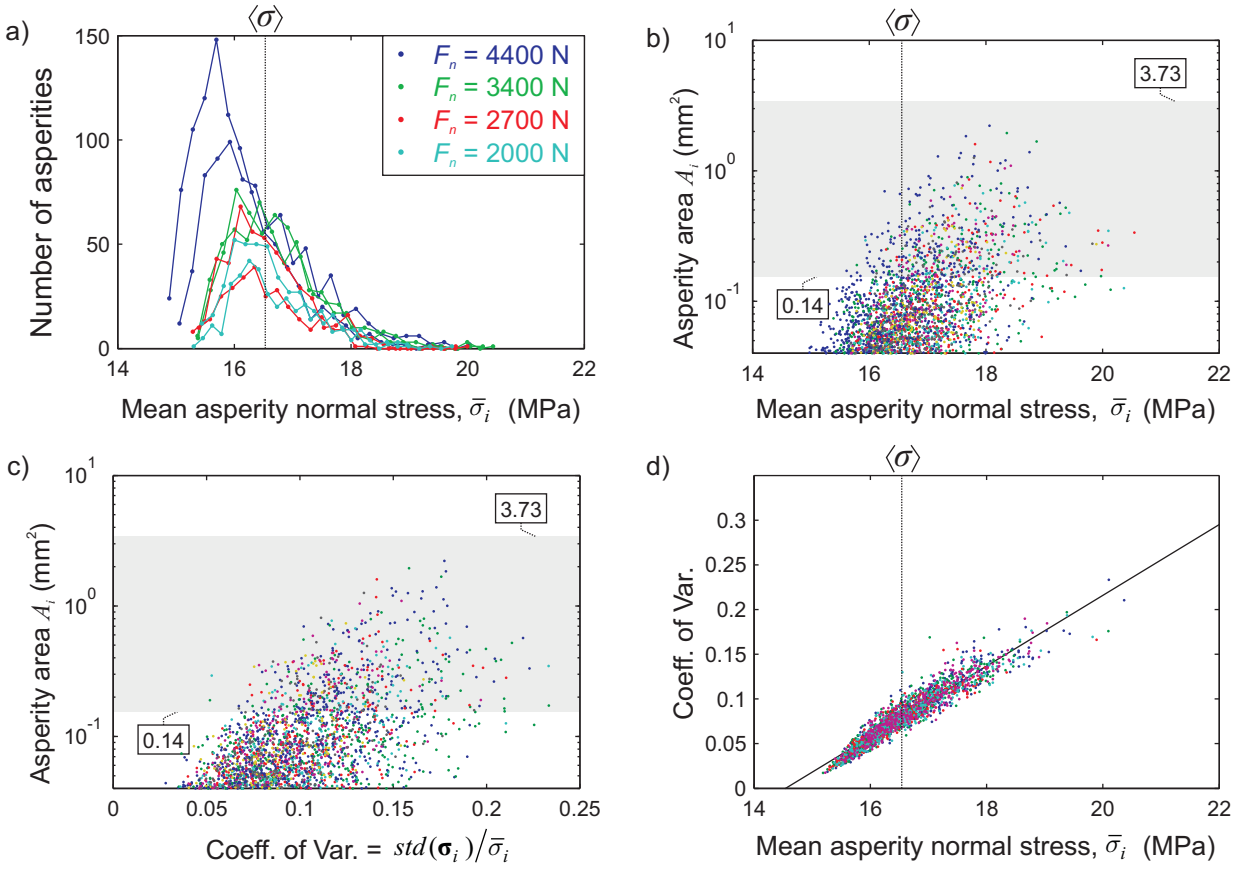

Figure 6.4: **(a)** Normal stress measurements taken from the *seismogenic* region of the fault (x = 150 mm to 300 mm) were compiled into a catalog for various levels of far-field normal force F_n. The probability distribution function (PDF) characterized the normal stress field $\bar{\sigma}_i$. **(b)** Average mean normal stress $\bar{\sigma}_i$ on each i^{th} individual asperity versus asperity size A_i. **(c)** Coefficient of variation cv_i on each i^{th} individual asperity versus asperity size A_i. **(d)** Average mean normal stress $\bar{\sigma}_i$ on each i^{th} individual asperity versus coefficient of variation cv_i.

The predominantly larger asperities (Figure 6.4(b)) form along the interface by coalescing with nearby asperities [see seminal work by Nayak, 133]. Asperities develop in a more convoluted manner as shown when the normal force was increased (Figure 6.3). The inset views in Figure 6.3 show that at higher applied load levels the hatched asperity seems to *grow* towards the asperity located just below it. Nayak's theory of coalescing asperities describes larger asperities coalescing with smaller asperities in the near field as the surfaces are pressed together with an increasing normal load. This type of asperity growth may be the reason for the relationships between asperity size, average normal stress and normal stress dispersion shown in Figure 6.4.

6.2 Microscopy of asperity surfaces

As mentioned in Section 5.2.1, precursory seismicity was only observed along a mature fault that has incurred an average cumulative slip $>\sim$ 36.1 mm. Surface roughness is used as an input parameter describing the random process models of two approaching rough surface in most (if not all) contact mechanics models. Most contact models infer the real contact area A_r from the roughness [146, 80, 145] and, although we directly measure this parameter with the pressure sensitive film, we felt it would be important to measure this parameter independently.

6.2.1 Digital photography of undeveloped and mature surfaces

In Figure 6.5 shows photographs of the fresh (left panel) and mature (right panel) faulting surface after cumulative slip $>$ 36.1 mm. An isometric and top view of the interface is shown. No experiments reported in this dissertation had unworn surface (left panels). The photographs were taken using a Lecia light microscope equipped with a digital camera. In the isometric view we see that large relatively flat sections were formed (see arrow). These surfaces show features (e.g. striations in the direction of sliding) similar to rock in a natural environment.

Figure 6.6 gives a closer image of the top view of the mature fault surface from the right panel in Figure 6.5. We used digital image processing [73, 114] to decompose the raw image into luminous intensity I as explained in Sections 3 and 4. Worn surfaces appeared darker; this caused the surface to become more translucent, reflecting less light back to the eye. PMMA is known to become translucent when heated past its glass transition temperature [11]. Frictional heating of the asperity may have lead to this change in surface appearance. Gouge and unworn surfaces appeared brighter. Figure 6.6(b) shows the enhanced image for pixels above the light intensity $I > 0.3471$; this highlights the gouge and unworn sections of the fault. Figure 6.6(c) shows the image for pixels above $I < 0.3471$, highlighting mature flat sections of the fault. In both cases higher luminous intensity is indicated by hotter colors. Details A and B show the high and low I images near a large flat section. It may be that the fault 'smears' during the wearing process due to friction. There appears to be deposits of gouge material ($I > 0.3471$) after the flat surface ($I < 0.3471$) in the direction of slip (see arrow in Figure 6.6 Detail B). Even though the fault was cleaned between each suite of experiments using pressurized air (at $\sim$ 60 psi) this gouge was solid and appeared crystalized, which can be seen better under higher magnification (see Section 6.2). Making a photographic record of the surface was crucial in driving this study to examine the roughness in greater detail; precursory seismicity must be controlled by these features and is the result of frictional processes in our experiments.

6.2.2 Optical profilometery

After the sequence of tests was performed (*postmortem* analysis), the slider block sample was examined using optical microscopy techniques. Figure 6.7(a) shows a typical asperity located at $x \approx 235$ mm and $y \approx 5.1$ mm on the slider sample using dark field illumination with an optical magnification of X 25.2. The asperity surfaces appeared flat on top as seen in the images presented in Figure 6.5), most likely due to wear processes that occurred during the preparation of the mature surface. We note that this asperity image was taken from within the *seismogenic* region shown in Figure 6.1(b). While we cannot be certain that this asperity was itself responsible for a

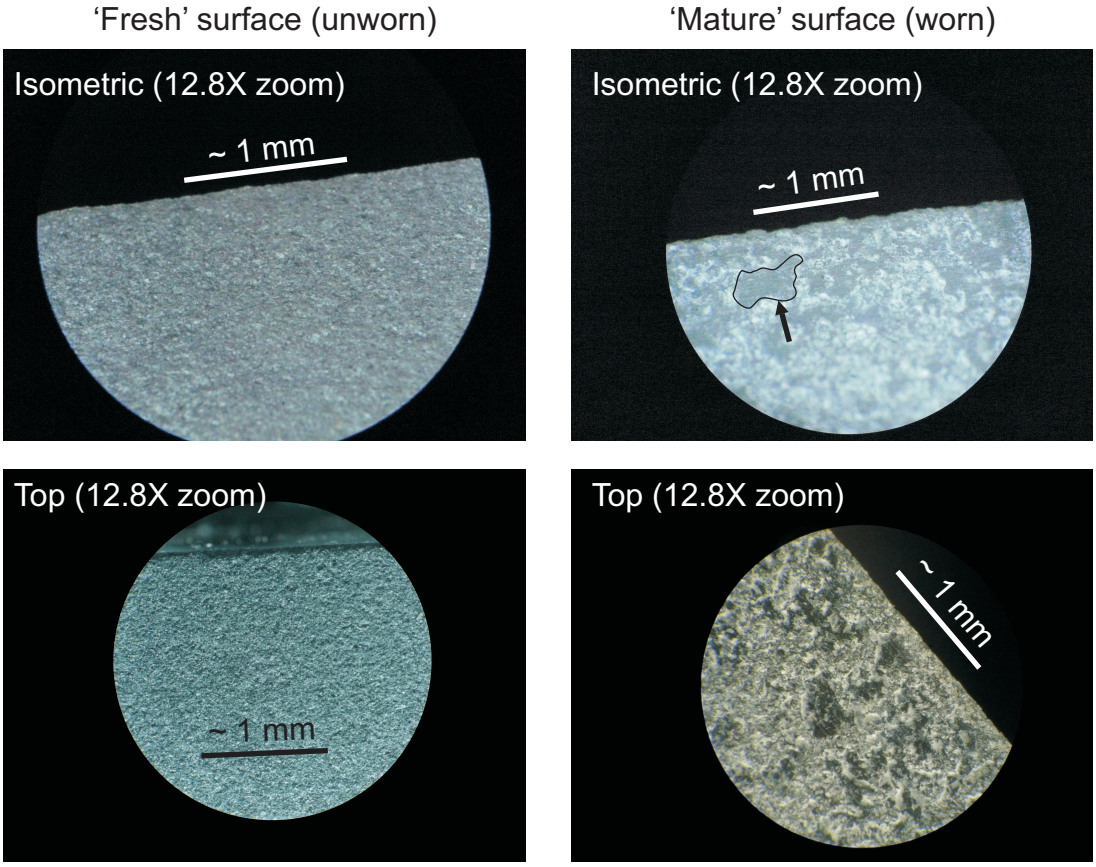

Figure 6.5: Isometric and top views of a fresh (left panel) and mature (right panel) faulting surface. We see that the mature faulting surface wears leaving 'flat-topped' asperities.

foreshock, we feel it is important to study surface roughness along the highly worn surfaces to better understand how asperity contact may have formed in this region.

At higher magnification interesting features were observed reminiscent of asperities on rock faults such as visual striations that align with the direction of slip and what appeared to be slickensides over portions of the asperity. A small section (256 µm x 196 µm) on a flat, translucent potion of the surface was analyzed using optical profilometry (ADE MicroXAM-100 Optical Profilometer). The results are shown in Figure 6.7(b). Transects of the roughness profile along slip (blue) and normal to slip (purple) are shown in Figure 6.7(c). The Hurst exponent H was calculated using the square of the modulus of the Fourier transform $P(k)$ [149, 43, 44]. In this study, we calculated H_{par} (along slip) and H_{per} (normal to slip) using

$$P(k) \propto k^{-(1+2H)} \tag{6.3}$$

where k is the wavenumber. To reduce noise associated with individual profiles, the spectrum was calculated by stacking all 1-D Fourier transforms. We observed noise from the experimental facilities at higher wave numbers and only used wavenumbers below $k \leq 5{\cdot}10^5$ µm^{-1} in each

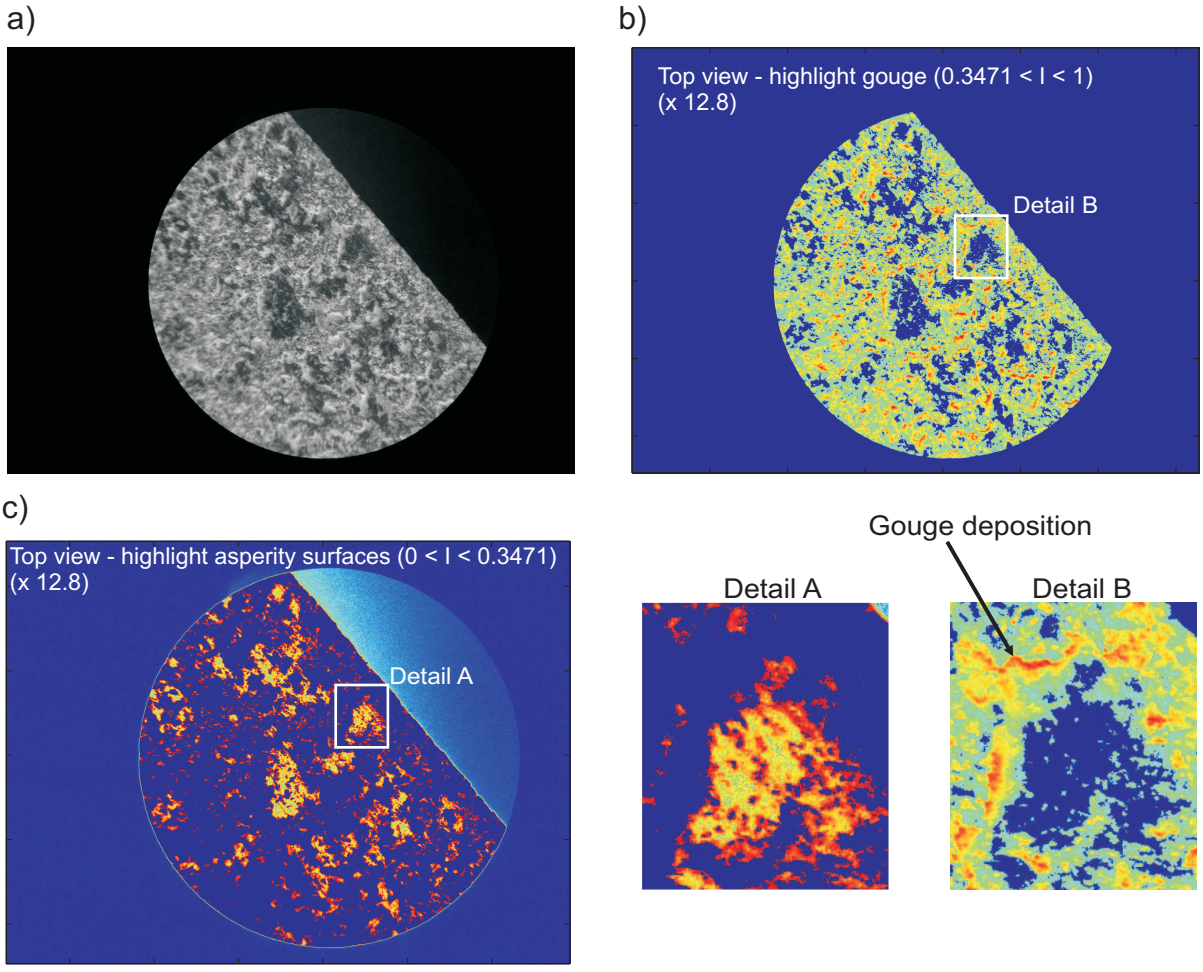

Figure 6.6: **(a)** Raw image of the mature faulting surface. **(b)** The image was converted to intensity I [114] and lighter pixels ($0.3471 > I > 1$) captured gouge and untouched surfaces. **(c)** Darker images ($0 > I \leq 0.3471$) were more indicative of a mature surface. Details A and B show dark and light pixels, respectively, enlarged for a prominent flat surface from the wearing process.

direction. The Hurst estimate of the roughness profile was taken on the flat, worn surfaces of the sample that were large enough to fit the window taken using the ADE MicroXAM-100 Optical Profilometer (i.e. minimum 256 µm x 196 µm). Linear regression was used to fit the log-log data between length scales of 5 µm to 196 µm in both normal to slip and along slip directions. Figure 6.7(d) shows the stacked Fourier power spectrum with estimates of H_{par} = 0.222 (along slip) and H_{per} = 0.324 (normal to slip).

Figure 6.8(a) gives measurements from the Nanovea PS50 Profilomter of a 25 mm x 12 mm section of the fault within the *seismogenic* region. Transects A and B are drawn through the lower (y = -4 mm) and upper (y = 4 mm) section of the fault, respectively. Figure 6.8(b) shows the probability density function (PDF) for the surface height for the entire surface shown in Figure 6.8(a). We note that the PDF is not Gaussian and seems to be display some skewedness. We assume that the PDF is isotropic (direction independent) but, as seen in Figure 6.7(d), there may to be some differences in the Hurst exponent (at least a short wavelengths), which we have attributed to the wearing process; this possible anisotropy of the PDF needs to be investigated in more detail in future studies. Figure 6.8(c) shows the height profile for the two transects A and B in Figure 6.8(a). We see that along the y = 4 mm Transect B the surface has wider, flatter surfaces that in the lower y = -4 mm Transect A. Transect A and B had RMS roughness of 4.85 µm and 5.31 µm, respectively. The smoother surfaces were also the region where larger foreshocks were observed (see Figure 6.1(b)).

In Figure 6.8(d) a small section from the upper Transect B was examined. The Hurst exponent was again calculated but for length scales that spanned the 'valleys' observed between the 'flat-topped' sections of the surface. We analyzed the Fourier Power Spectrum (FPS) between length scales of 5 µm to 780 µm and found that the Hurst roughness estimate increased to H_{low} = 0.595 (Figure 6.8(b)). The increase in the Hurst roughness exponent is attributed to the low-frequency content from the average height h (i.e. distance from the 'flat-top' to valley) of the asperities. The effect of surface roughness on the manner in which asperities are formed has been studied [78, 133, 80, 16, 160, 145]; these features may play an important role in determining how resistive a patch of asperities are to shearing when perturbed with a slowly growing nucleation front. The increased number of 'flat-topped' sections, measured on the upper ($y < 0$) portion of the *seismogenic* zone, may be a prerequisite for the generation of foreshocks in the preparatory phase. In Section 8, we discuss the necessary conditions for the spontaneous generation of localized rapid sliding the at asperity-level (foreshocks) with additional insight gathered from the both the pressure sensitive film and the roughness measurements presented here.

6.3 Non-contact slip sensors

6.3.1 Spatial slow slip distribution along the fault

Figure 6.9(a) summarizes the fault asperities for a normal load of F_n = 4400 N and the locations of the slip sensors (NC1-NC7). The time at which slow slip transitioned to rapid sliding (t_{fail}) was defined as the point at which the local slip rate breached V_{thresh} (= 4 mm/s) at any slip sensor during the loading cycle. Figure 6.9(b) shows the spatio-temporal profiles of slow slip along the x-axis at 1 second intervals leading up to t_{fail} (thick blue line). A piecewise cubic Hermite shape-preserving interpolation scheme [71] was used to calculate the slip profiles (black lines) across the

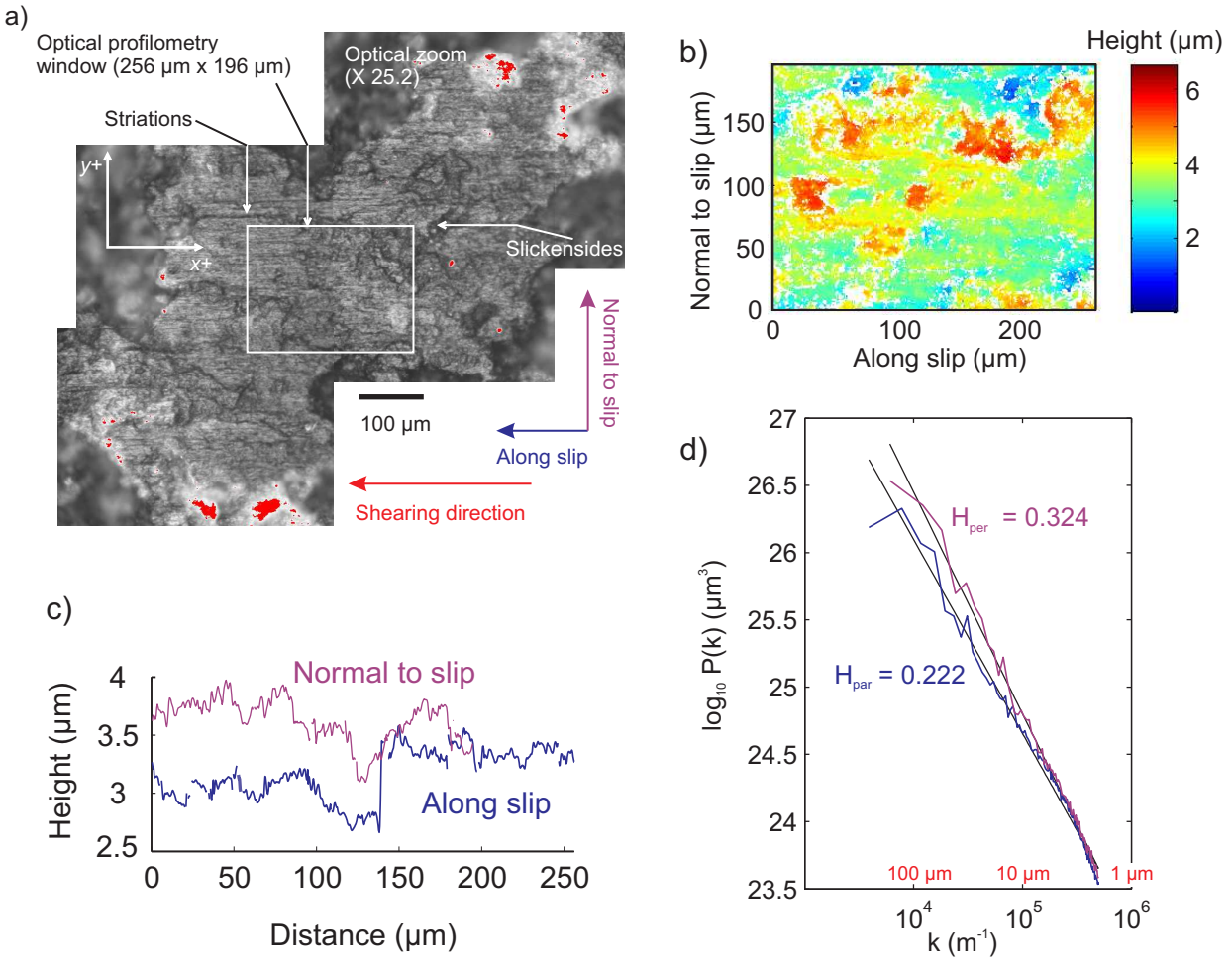

Figure 6.7: (a) Optical microscopy images of an asperity, on the slider block surface, located in the highly *seismogenic* region of the fault (approximately x = 235 mm and y = 5.1 mm) after the suite of experiments were performed. The image was created by stitching together four sub-images. We see evidence of features similar to geological features on natural faulting surfaces [44], such as striations and slickensides. (b) Optical profilometery measured 2-D surface profiles. (c) An example of the height profile along transects in the direction of slip and normal to slip. (d) Fourier power spectrum $P(k)$ of the stacked 1-D profiles in the direction and normal to slip on the interface. The Hurst estimate H (equation (6.3)) was used to measure the self-affinity of the surface in both directions (H_{par} and H_{per}).

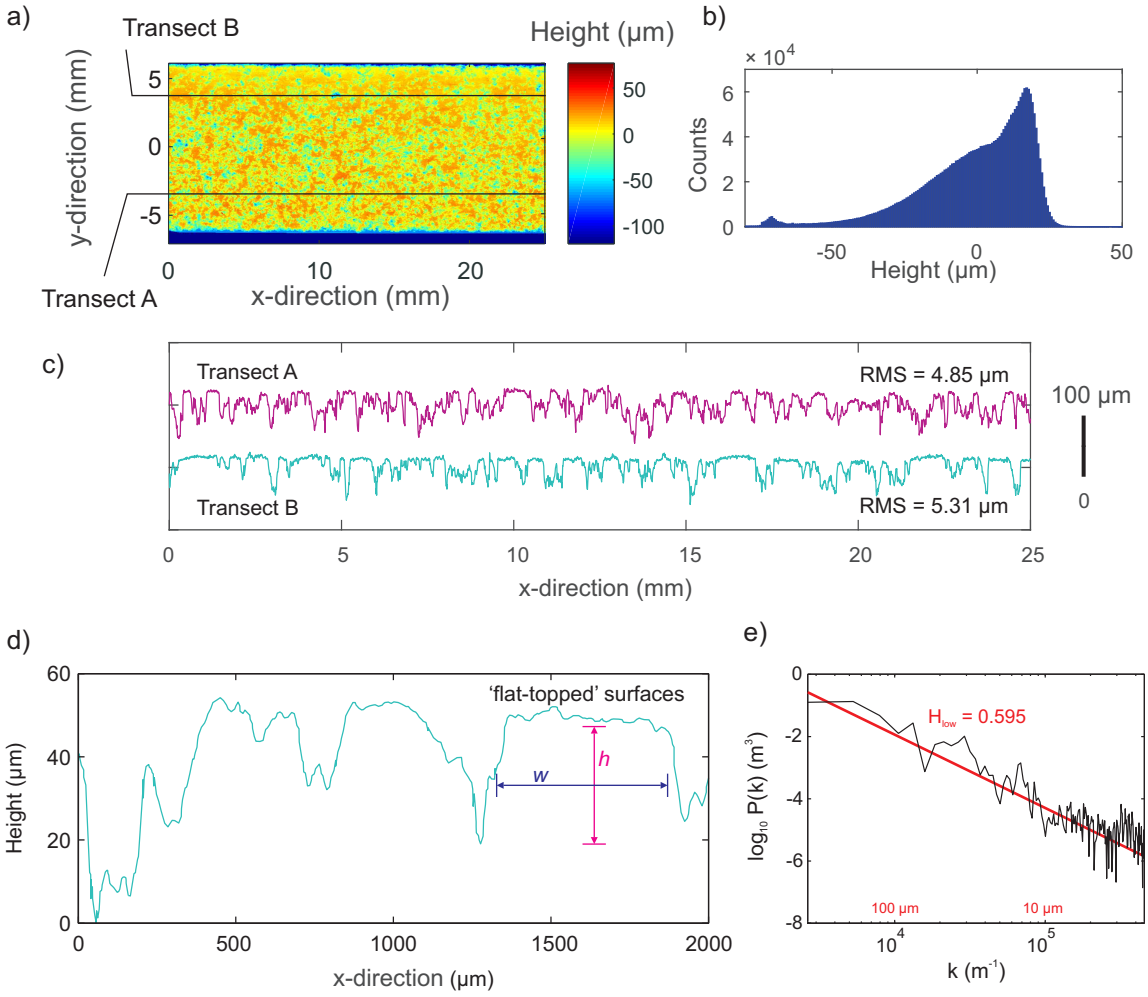

Figure 6.8: **(a)** A large section (25 mm x 12 mm) of the seismogenic region is shown. **(b)** The Power Density Function (PDF) of surface heights is shown for (a). **(c)** Surface profiles from Transect A (y= -4 mm) and Transect B (y= 4 mm) are shown for the section shown in (a). Transect B has more and larger 'flat-topped' surfaces than the lower region. **(d)** A small 2 mm section of Transect B was examined to better see the 'flat-topped' feature. We see that this feature has a width $w \sim 0.7$ mm and height $h \sim 0.03$ mm. **(e)** Hurst exponent estimates for the longer length scale measurements had additional low frequency content (H_{low}) added by the asperity heights h than those measured on just the 'flat-top' features seen in Figure 6.7.

sensors attached to the upper surface $y > 0$ (NC1, NC3, NC5, NC6 and NC7) at 100 mm separation distances.

Figure 6.9(b) and 6.9(c) show the slow slip accumulation along the fault for two levels of normal load (F_n = 4400 N and 2700 N) and two stick-slip events (SS2 and SS3), respectively. SS1 did not display any foreshocks and their slow slip profiles are not shown. Slow slip profiles along the fault at t_{fail} - 50 s or t_{fail} - 25 s before failure is shown as the thick red line. Accumulation of slip at different locations on the fault can be easily visualized: (i) sections of the fault that showed more compressed slip profiles indicate a relatively locked section of the fault and (ii) increased spacing between subsequent slip profiles indicated accelerating slip.

Slow slip initially accumulated relatively uniformly along the fault. This can be seen by the flat (low spatial slip gradient) red lines in Figures 6.9(b) and 6.9(c), which represent the slip profiles at 50 s and 25 s before failure, respectively. Over time (loading continues) the gradient becomes larger at the side near the thrust; the amount of gradient depends on the normal force F_n. The amount of slip across the fault forms an elbow with time and flattens out between 100 mm to 200 mm past the loaded edge, depending on the normal load. An example of the 'elbow' is shown for SSE 3 at F_n = 4400 N in Figure 6.9(b). As time to failure decreased, (i) the level of slip gradient (between the TE and LE) increased and (ii) the 'elbow' propagated away from the trailing edge (TE) into the region containing a more dense distribution of asperities (Figure 6.9(a)). We refer to the more densely distributed asperity region as the 'relatively locked' section of the fault. We estimated the speed at which the 'elbow' propagated into the relatively locked section by taking the approximate location of the 'elbow' at failure, we then assumed it began at the loading point edge and took 25 s or 50 s (depending on the normal load F_n) to propagate to the locked section. The estimates of the average 'elbow' propagation speed are shown as the dashed magenta lines depicted on the slip profiles at time t_{fail} (blue lines) in Figure 6.9(b). The location of the 'elbow' was used to define the location of the rupture tip of the nucleation region (Section 1.3.1); the sudden breakdown of shear stress behind the rupture tip resulted in an increase in slip as described by the slip-weakening model.

The average speed at which the rupture tip (or breakdown tip) moved into the relatively locked region ranged from 2 mm/s to 9.5 mm/s over the last 25 to 50 seconds before failure, and was dependent on the normal confining force F_n. At higher F_n, the breakdown tip did not penetrate as far into the locked region and moved at a slower speed than that measured at lower normal confining loads. Detail A in Figure 6.9(b) shows the increased detail used to estimate the location and propagation speed of the 'elbow'. Estimates show that the tip progressed $\sim$ 100 mm to 150 mm away from the TE at speeds between $\sim$ 1 mm/s – 3 mm/s for higher F_n and $\sim$ 150 mm to 200 mm away from the TE at speeds between $\sim$ 6 mm/s – 9.5 mm/s for lower F_n.

Examining the measured slip profiles at failure (t_{fail}) for the events shown in Figure 6.9(b) and (c), we can see that the gradient in slow slip along the x-direction increased (δ) with additional confining normal force F_n. The gradient in slip profiles ($\partial\delta/\partial x$) at failure due to higher F_n would, by definition, result in a proportional increase in the strain ϵ and the amount of locally stored strain energy. We examine the effects of strain energy (and its release with slip) and the resulting effects on the development of foreshocks using the numerical study presented in Section7.

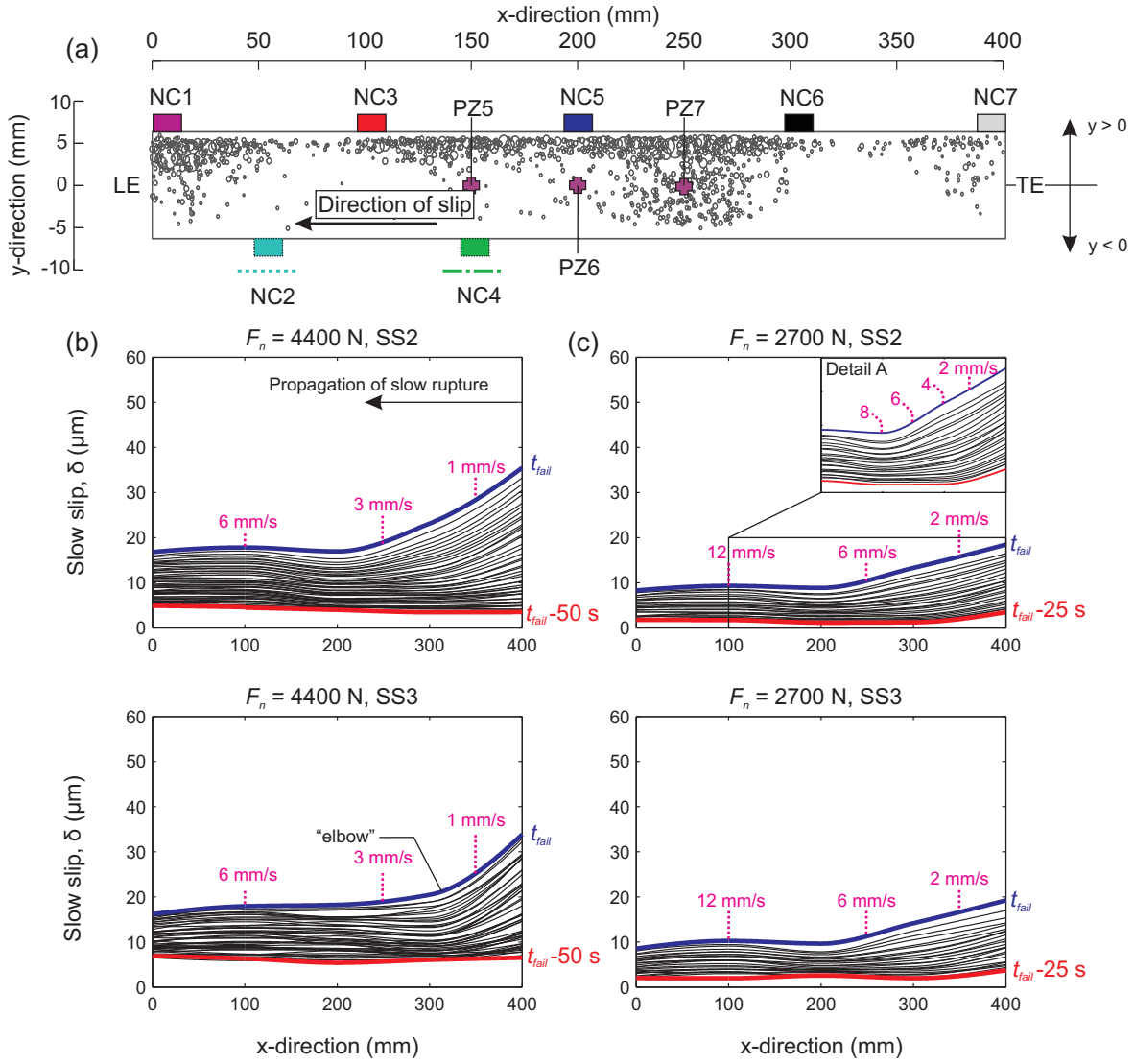

Figure 6.9: Slip profiles in the x-direction interpolated from the non-contact (NC) displacement sensors at times 25 s to 50 s before gross fault rupture (t_{fail}). **(a)** Contact estimates along the fault and locations of the slip sensors with respect to the upper (y>0) and lower (y<0) surface. **(b)** Interpolated slow slip data from upper surface (black) for the 50 s before rapid sliding for the stick-slip events SS2 and SS3 at F_n = 4400 N. **(c)** Interpolated slow slip data from upper surface (black) sensors for 25 s before failure for the stick-slip events SS2 and SS3 at F_n = 2700 N. Estimates of the 'elbow' propagation speed away from the trailing edge (TE) were calculated using the velocity measurements shown in magenta. The increased detail shown in Detail A is used to better estimate elbow location and propagation speed.

6.3.2 Shear strain approximation from slow slip measurements

Premonitory slip was observed in all experiments but the amount varied dependent on the normal force F_n (see Figure 6.9). The difference between premonitory slip at the leading edge, NC1 (x = 0 mm), and trailing edge, NC7 (x = 400 mm), was used to calculate the mean shear strain ϵ_s along the fault when normalized by the fault length L = 400 mm [167]: i.e.,

$$\epsilon_s = \frac{\delta_{(x=400\text{ mm})} - \delta_{(x=0\text{ mm})}}{L} = \frac{\delta_L - \delta_0}{L}. \tag{6.4}$$

Figure 6.9 shows an increase in shear strain across the fault with increased F_n; the fault had increased shear stiffness which increased its ability to accommodate premonitory slip. We attribute this to the creation of additional asperities and an increase in the size of preexisting asperities (see Figure 6.2).

From the slow slip data shown in Figures 6.9(b) and (c), breakdown of shear stress begins at the trailing edge (TE) as more slip accumulates in this region leading up to failure. We observed a slowly propagating slip front which grew between $\sim$ 1 mm/s to 9 mm/s into the central region of the fault – a region with a large clustering of asperities (Figure 6.9(a)). The amount of slow slip increased as the normal force F_n increased, as did the gradient in slip along the x-direction. From Figures 6.9(b) and (c) we see that the leading edge (LE, x = 0 mm) experienced similar amounts of slow slip at all load levels while the trailing edge (TE, x = 400 mm) experienced more slip at higher normal confining loads. Using equation (6.4) we found ϵ_s was $\sim$ 4.52 x 10^{-5} at F_n = 4400 N and decreased to $\sim$ 2.41 x 10^{-5} at F_n = 2700 N.

6.4 Piezoelectric AE sensors

6.4.1 Foreshock size versus applied normal force

Figure 6.10(a) gives details of the acoustic emission (AE) measurements for foreshocks observed from PZ6 during the loading cycle for the third stick-slip event (SS3) at all four normal load levels. Only the largest foreshock was plotted within each sequence. In general, we observed a dependence between the foreshock size, measured as the peak ground displacement (PGD is described in Section 5.2.3), and applied normal stress: for larger applied loads, we noticed an increase in the size (PGD) of the foreshock. In foreshock sequences at higher normal loads we still observed small foreshocks, but the numerical model (Section 7) offers an explanation for the potential of larger events due to the fault's ability to locally store more shear strain energy adjacent to larger asperities. Figure 6.10(b) shows the peak ground displacements (PGD) of all foreshocks observed during the preparatory phase for their respective normal load F_n.

6.4.2 Foreshock source radius

We use Brune's relationship [40, 39] to estimate the source dimension for individual foreshocks. The corner frequency of the radiated seismic energy was used to calculate the source radius R_0 of the given event using the relationship:

$$R_0 = \frac{2.34\beta}{2\pi f_0} \tag{6.5}$$

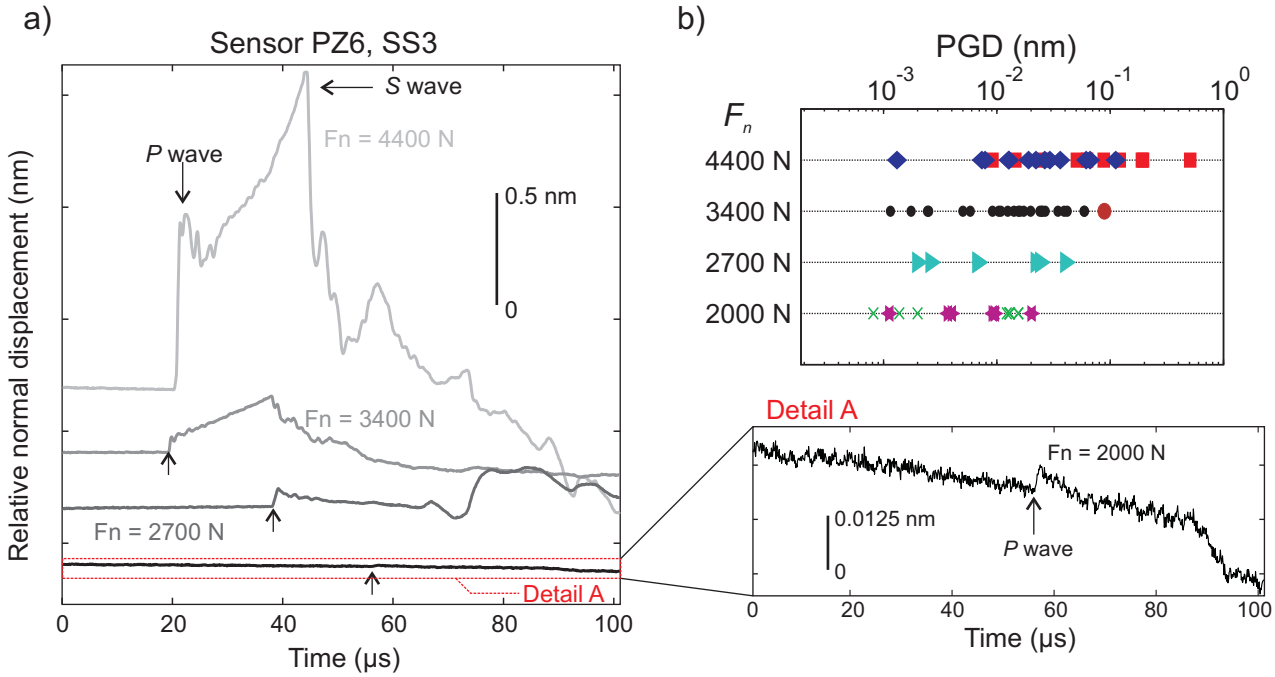

Figure 6.10: **(a)** Actual waveforms of the largest foreshock in the SS3 sequences (for all normal load levels), recorded from AE sensor PZ6. **(b)** Total catalogue of foreshocks size PGD with respect to normal force F_n

where β is the shear wave velocity of PMMA (1390 m/s), f_0 is the corner frequency given in kHz, and R_0 is the source radius in mm. The elasto-dynamic energy released, due to local rapid sliding on a single asperity, occurs over a finite time t_0 and is observed as foreshocks. The width of the S wave pulse, in Brune's relationship, describes the duration of the moment rate function and this can be used to approximate the corner frequency f_0. We used the duration of the first S wave pulse to determine the rupture duration t_0 whose inverse is approximately the corner frequency f_0 (i.e. $f_0 \sim 1/t_0$ [122]). Rupture duration ranged from 0.4 μs to 2.1 μs for the total catalog of 68 foreshocks. The source radii ranged from $R_0 \sim 0.21$ mm to 1.09 mm according to the Brune relationship (equation (6.5)). These estimates of source radii are similar to the actual measurements provided by the pressure sensitive film (Figure 6.1(a)) which ranged from $R_{film} \sim$ 0.06 mm to 1.25 mm. From the Brune relationship in (6.5) we can evaluate the corner frequency f_0 as a function of the circular asperity radius: i.e. $f_0 = 2.34\beta/(2\pi R_0)$ According to the Brune relationship, the range of asperity radii recorded from the film $R_{film} \sim 0.06$ mm to 1.25 mm may result in small earthquakes with corner frequencies ranging from $\sim$ 414 kHz to 8.6 MHz if the asperities were to fail dynamically. The smaller asperities (R_0 = 0.06 mm) fall outside of the flat broadband range of our acoustic sensors (100 kHz – 2.5 MHz) and we are therefore limited to observing asperity failure with minimum source radii of $R_0 \sim 0.21$ mm.

6.4.3 Foreshock spectral response

Figure 6.11(a) shows the S wave arrival from the largest foreshock along the interface. We see the peak ground displacement (PGD) occurs as the S wave passes the sensor, which is to be expected [3] at these hypocentral distances. We take advantage of the absolutely calibrated nature of the AE sensors between the frequencies of $\sim$ 5 kHz to 2.5 MHz [116]. The displacement spectral density was calculated for the S wave arrival using the fast Fourier transform algorithm [35] in MATLAB. The time domain of the signal is shown in Figure 6.11(a) and the spectral density in Figure 6.11(b) (black lines in both plots). The time domain signal was 190 µs (1900 samples), windowed starting at 20 µs after the P wave arrival. The windowed data was enveloped by a Blackmann-Harris window of the same length. Frequency content of the noise (black dots) was calculated using the signal 190 µs (1900 samples) long and centered 100 µs before the P wave picks given by equation (5.1). The noise spectrum was also enveloped using a Blackmann-Harris window of the same length.

The classical theory of seismic radiation from an earthquake source is based on the model of shear dislocation. In Brune's model [40, 22], the source occurs on a circular patch (in our experiment this is assumed to be the interfacial asperities) and shear displacement on the dislocation is given as

$$u(t) = u(\infty)\left[1 - \left(1 + \frac{t}{\chi}\right)e^{-t/\chi}\right], \tag{6.6}$$

where χ is the parameter governing the speed of the dislocation displacement from initial to final value $u(\infty)$. This leads to a low-frequency spectral plateau related to the corner frequency by,

$$\Omega(f) = \frac{\Omega_{0S}}{1 + (f/f_{0S})^2} \cdot \mathsf{Exp}\left[-\frac{\pi \cdot\cdot R_{ss}}{V_s Q_s} \cdot f\right] \tag{6.7}$$

where R_{ss} is the source to sensor distance, V_s is the shear wave velocity of PMMA, Q_s is the non-dimensional quality factor in PMMA (representative of intrinsic attenuation effects). From McLaskey [118], the quality factor of PMMA is Q_s = 80. The source to sensor distance was calculated as the Euclidian distance once the foreshock was located (see Section 5.2.3). The values of Ω_{0S} and f_{0S} were fitted to the displacement parameter between the frequency ranges shown in Figure 6.11(b). The seismic moment can be calculated from

$$M_{0s} = \frac{4\pi\rho\,(V_s)^3\,R_{ss}\Omega_{0S}}{F_s R_f} \tag{6.8}$$

where ρ is the PMMA density, F_s is the S wave radiation coefficient for a shear source (=0.63 from Das and Scholz [56]). Given that the sensors are coupled to a free surface, a correction was made for free-surface amplification (R_f) following Aki and Richards [3].

In the previous section, the assumption is that $f_0 \equiv 1/\chi$ and using this we can estimate the source sizes. Here we elaborate on this assumption and use equations (6.6) – (6.8) to estimate, from the seismic radiation, the seismic moment and moment magnitude generated from the asperity failure. By hand fitting, we can see that the corner frequency was f_{0s} = 375 kHz and seismic moment M_{0s} = 1.8 Nm (M_w = -5.9). We note that the experimentally measured spectral decay falloff was f^{-2}; following the classical theory of seismic radiation, this suggests that sudden shear dislocations of small laboratory asperities are similar to naturally occurring earthquakes.

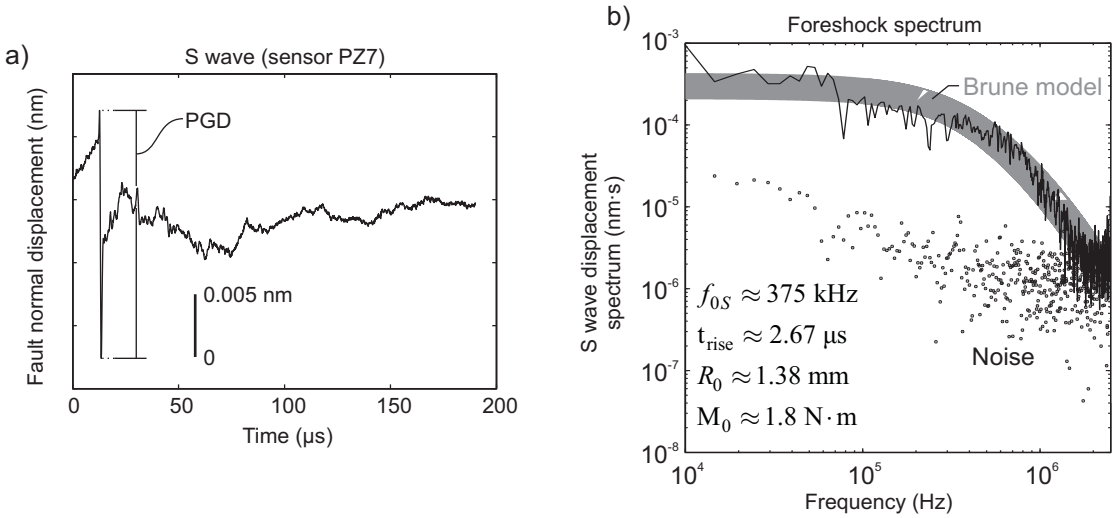

Figure 6.11: **(a)** Time domain of the S wave of a foreshock measured by PZ7. **(b)** Displacement spectrum (black line) and noise spectrum (black dots) of the S wave in (a). The model described by equation (6.6)–(6.8) is given by the gray curve.

This is the framework that should be implemented in future studies but there are some areas for concern with the measurements provided from the AE signals. The time domain signals (Figure 6.11(a)) shows an offset (specifically at times 0 to 10 μs) that are not present in similar laboratory AE studies that take advantage of the classical theory of seismic radiation defined by equations (6.6) –(6.8) [122, 74]. From Aki and Richards [3], we know far-field terms describing displacement at the sensors will be pulse-like following the moment-rate function (i.e. proportional to the derivative of equation (6.6)). Near-field terms will have a shape similar to the moment function (i.e. proportional to equation (6.6)) and will create a permanent offset at the sensor. The near-field term adds low frequency content to the signal, which increases the estimate of Ω_{0S}. It is likely that the seismic moment of this source is in actuality smaller than the estimate provided by equation (6.8). Near-field terms may provide information about the stress states (or shear strength) along the asperity as rapid breakdown occurs but this requires finite fault rupture modelling [e.g., 54, 55, 28, 153].

6.4.4 Spatio-temporal distributions of foreshock sequences

All the foreshocks were constrained to the *seismogenic* region shown in Figure 6.1(b). Figure 6.12 shows foreshock sequences recorded during the second stick-slip event (i.e. SS2) described in section 5.2.1. Figure 6.12(a) shows the slip (solid black) and slip rate (gray) measured from each slip sensor for all four load levels during SS2. The time history of the slip signal is differentiated numerically to obtain the slip velocity. The pulse characterized the shear rupture accelerating then decelerating along the interface; a process that took $\sim$ 4–6 ms. Once the fault decelerated, new populations of asperity contacts were formed along the interface. Full rupture was also measured acoustically, using the low sensitivity PZ15 AE sensor (light gray). These measurements are given

in voltage since the low sensitivity AE sensors had not been absolutely calibrated. Foreshocks were determined using the high sensitivity AE array (PZ1-PZ13) and their timings are plotted in Figure 6.12(b). Figure 6.12(a) shows only the foreshocks close to the main shock while Figure 6.12(b) shows the full foreshock catalog. No foreshocks were observed for SS2 at F_n = 2700 N and the reasons will be discussed in the section 6.4.7.

6.4.5 Foreshock recurrence rates

Figure 6.13(a) examines the timing of foreshocks from each SS (see legend on top right). In general, time between foreshocks decreased as the main shock drew closer, an observation that has been made in the field [93]. In tests F_n = 4400 N SS3 and F_n = 3400 N SS3 foreshock sequences began at upwards of 10 seconds prior to the mainshock. In all other tests, the locatable foreshocks (described in the next section) began at times of 1 s or less before the impending main shock.

6.4.6 Foreshocks distance in relation to main shock

Figure 6.13(b) shows the foreshock distance to the mainshock (L_m) in relation to the timing of the main shock for each sequence of foreshocks. Recent studies propose that the main shock (or subsequent foreshocks) may be triggered by foreshock after-slip which propagates in a diffusional manner from the hypocenter of the foreshock [5, 183]. In nature, post-seismic transients can result from processes associated with time-dependence such as viscoelasticity, creep and poroelasticity [14]. If post-foreshock transients are present in our experiment, these would only be caused by the fault creep (i.e. visco-elastoplastic deformations). Ando and Imanishi **[2011]** studied the 2011 earthquake in the Pacific Coast of Tohoku, Japan, and found that after-slip propagated away from the foreshock following the relationship:

$$L_m = (DT)^{1/2} \tag{6.9}$$

where T (seconds) is the event occurrence time and L_m (mm) is the distance of migration, and the constant D (mm^{2}s^{-1}) is a coefficient identified with underlying diffusional processes. The basic hypothesis is that after-slip from individual foreshocks propagate away from the source and slows down (in a diffusional manner). The main shock (or subsequent foreshocks) is then triggered when the diffusional wave reaches the main shock hypocenter. We do see, in some cases, that subsequent foreshocks can occur along a diffusional line: e.g. the final two foreshocks in the F_n = 4400 N SSE3 along the D = 104 mm^{2}s^{-1} diffusion line. While there seems to be little correlation, in field studies conclusions of diffusional slip triggering the main shock have been found from so few as one or two large foreshocks beforehand [5, 183] and the migrating swarms of smaller earthquakes. While diffusional slip may trigger subsequent foreshock (or main shock), the general disorder observation suggests that more processes are driving foreshocks.

6.4.7 Non-located foreshocks and additional seismic activity

The foreshock sequences described in Figure 6.12 (and Figure 8 from Selvadurai and Glaser [166]) are comprised of 68 total foreshocks over 8 full ruptures. Figure 6.14 details the raw AE signals from sensors PZ5-PZ7 directly below the central region for SS2 at $F_n \sim$ 2700 N (0 foreshocks) and SS2 at $F_n \sim$ 2000 N (9 foreshocks). The foreshocks are indicated by the green lines. The arrival

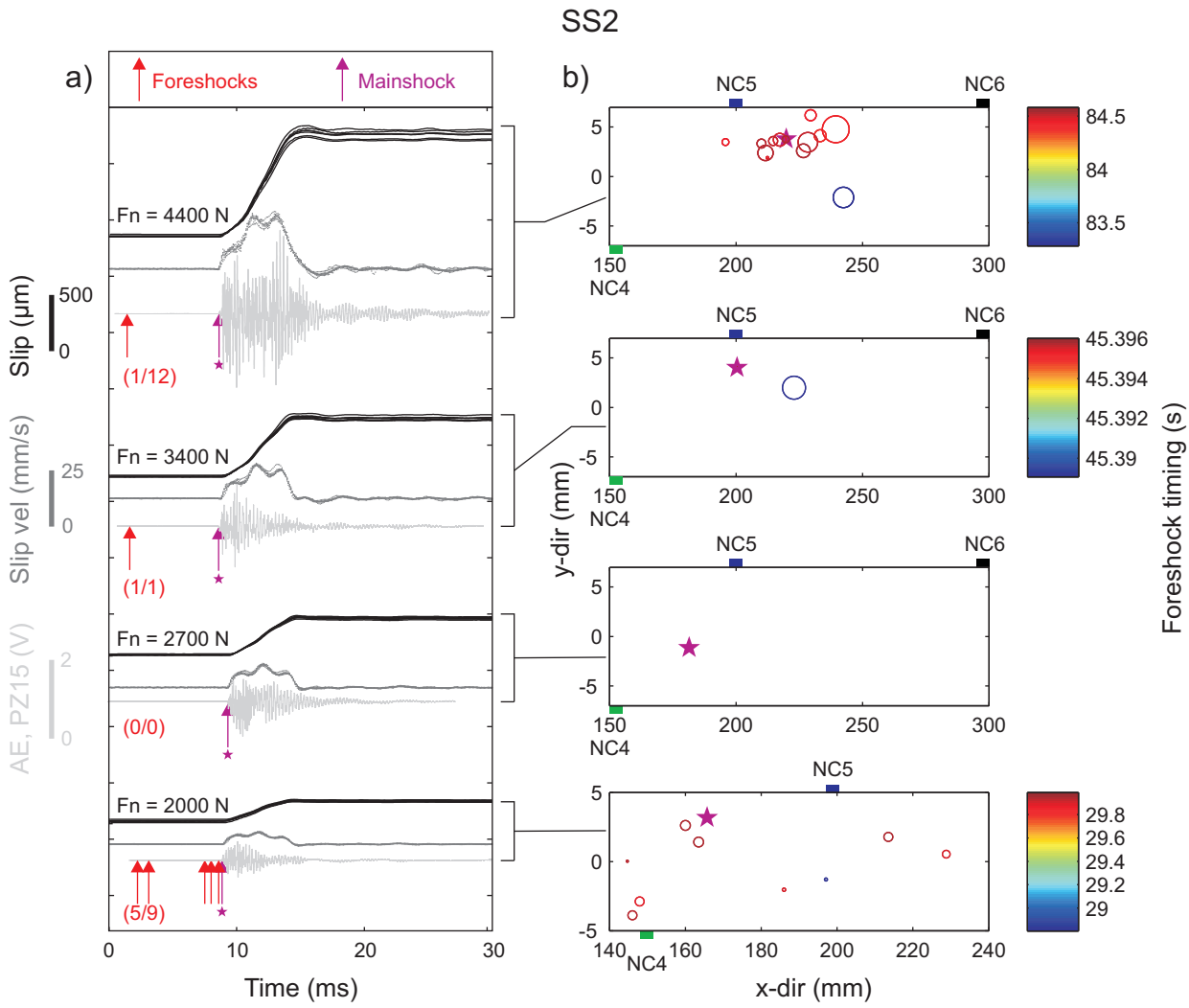

Figure 6.12: Spatio-temporal distributions of foreshocks during SS2 at various normal loads F_n. **(a)** Slip (black) and slip rate (gray) measurements calculated from displacement transducers prior to and during the rapid sliding phase and AE signals (light gray) of gross fault rupture captured using the low sensitivity sensor PZ15. Foreshocks (red arrows) and main shock (MS, magenta arrow) are shown for a window of ~10 ms before rapid slip. In most cases, the foreshock sequences began before this time window and the red fraction indicates the amount of foreshocks visible in (a). **(b)** Full foreshock sequences during SS2. The color code highlights the temporal evolution of the sequence (from blue to red) and the main shock hypocenter location is the star. Foreshocks are shown as circles with sizes proportional to Peak Ground Displacements (PGD).

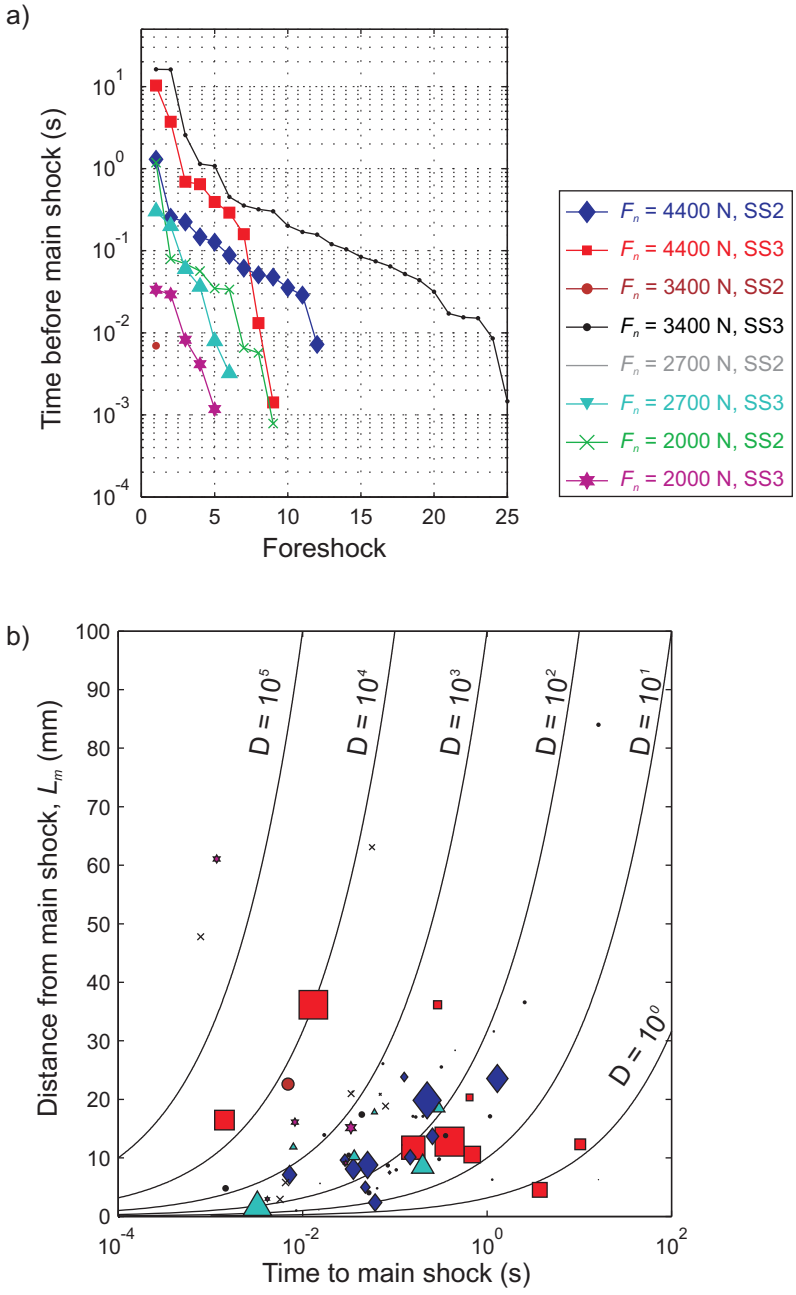

Figure 6.13: (a) Foreshock timing in relation to main shock. (b) The study of diffusional after-slip process that may have led to foreshock triggering

picking algorithm (equation (5.1)) detected additional events during the test (black circles). These events were very small in amplitude (see details A and B in Figure 6.14) and presented impulsive P- and S-wave arrivals similar to the larger events. The location algorithm, however, was unable to locate them due to the lack of manifestation over a sufficient number of sensors. These signals were referred to as 'foreshocks [which were] detected only'. (This lack of signal strength was most likely due to the amplitude attenuation in PMMA.) For all 8 gross fault ruptures, the number of events that could not be accurately located was 85 for PZ5, 59 for PZ6 and 133 for PZ7. This gives an indication of the variations in local activity at the leading and trailing edge of the seismically active region. PZ7, which was located at the trailing edge of the 'locked' region, accounted for $\sim$ 49% of the increased activity, while the central (PZ6) and leading edge (PZ5) sensors comprised 21% and 30%, respectively. We did not study these signals in great detail but they may be similar to swarm-like foreshocks noted on natural faults [96, 183, 37, 123]. We believe that more focus should be given to these signals that seem to exists near the edge of the nucleation zone. In future studies, these precursory seismicity signals could be studies by increasing the number sensors near the nucleation region tip (better locating constraints) or possibly reducing the thickness of the base plate (reduced attenuation of the signal).

6.4.8 Asperity interactions during slow slip phase

We used photometry to observe light changes along a small portion of the fault during the premonitory phase. The photometric results presented here were from experiments detailed in Selvadurai and Glaser [167] and performed before the results described in Section 4. These novel observations and potential importance for our understanding of the mechanisms controlling friction due to asperity level interactions [*personal communication with Allan Rubin*] is the reason for the inclusion of this result here.

While the visualization of asperities under normal loads is not a novel technique [63, 64], doing so under combined normal and shear loading (as in this experiment) is a relatively new development [132]. Figure 6.15 shows photographic frames taken from the slip-deprived region during the slow loading phase. At failure, the camera image becomes blurred due to the rapid motion along the interface. The first blurred frame was called the '$t_{fail} - 0$ frame' (Figure 6.15(d)). Figures 6.15(a), (b) and (c) represent images taken 300, 60 and 6 frames before the first blurred image. Images were converted to luminous intensity as explained in Section 4. The unmagnified image contains the interface (blue region) as well as portions of the base plate that reflect incident light from the room (appearing red). Magnifying the interface, we observe small bright spots that are indicative of asperity contact.

Using the photographic technique, Selvadurai and Glaser [165, 167] have begun to study the concomitant light changes and foreshock signals emanating from similar regions on the fault, between subsequent frames measured. Here the large asperity shown in the 20X magnified image is examined; the light intensity transmitted across the asperity decreased as failure drew closer (between Figures 6.15(c) and (d)). These images were not converted to normal stress; although they are presented here and are not meant for any quantitative analysis. We observed: (*i*) the larger asperities transmitted light relatively constantly for a large portion of the slow slip cycle and (*ii*) the light intensity decreased along the periphery of the large asperity as imminent failure approached. Using this information, we attempted to develop a numerical model that can captured these two phenomena.

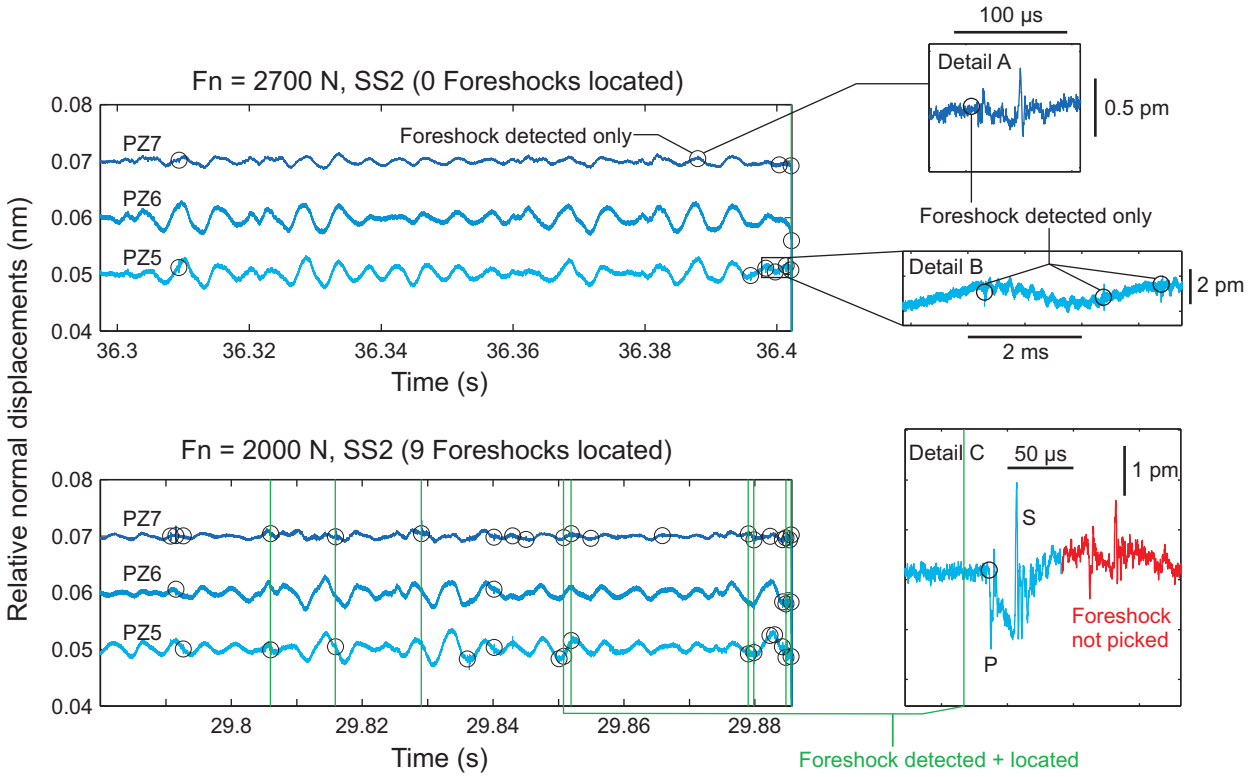

Figure 6.14: Increase in seismic activity measured for SS2 at F_n = 2700 N and SS2 at F_n = 2000 N. The former experienced no locatable foreshocks but the picking algorithm was able to detect events (black circles) which displayed similar pulse-like P and S wave characteristics (details A and B) to locatable foreshocks. SS2 at F_n = 2000 N experienced a total of 9 locatable foreshocks (green lines) and had 21 non-locatable foreshocks between sensors PZ5-PZ7. Detail C shows an enhanced view of a located foreshock that was quickly followed by an unpicked event (red).

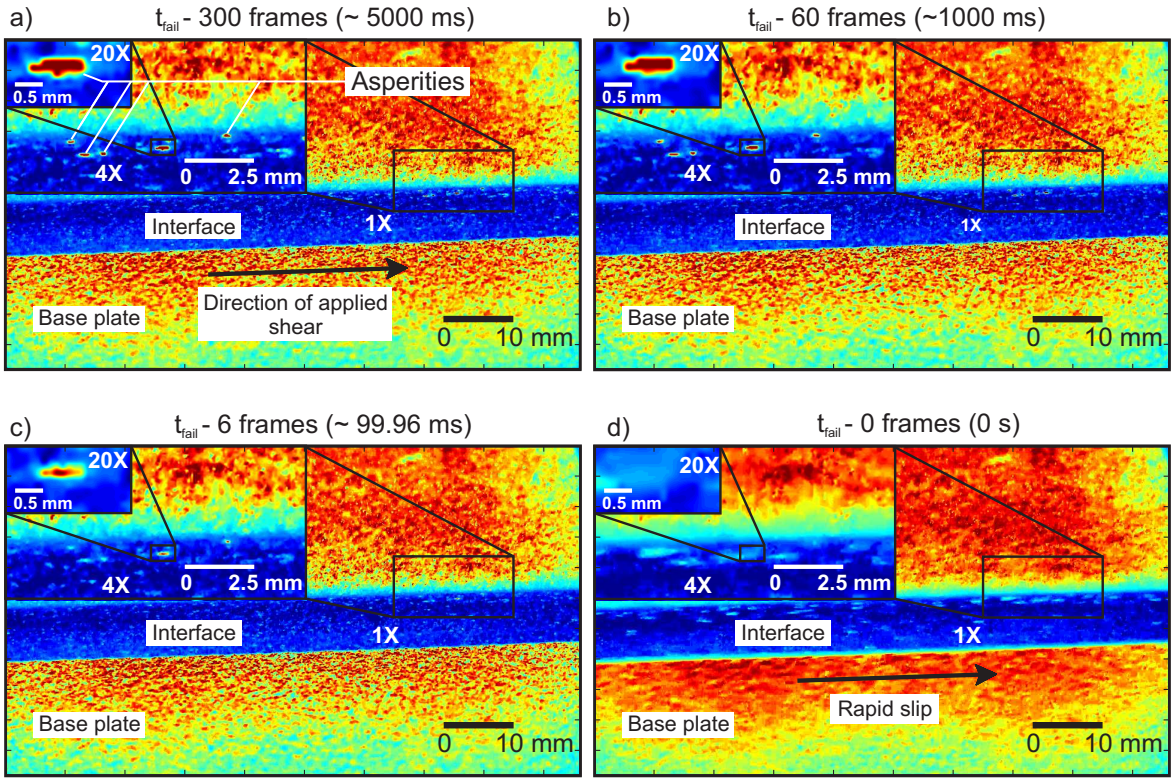

Figure 6.15: Photometric images obtained during the premonitory slip phase of the loading cycle from x = 200 to 241 mm. Frame shown in (d) represented the first image to become blurred – a characteristic we assumed to be representative of the onset of rapid sliding along the fault. Images in (a), (b) and (c) represent 300, 60 and 6 frames before the rapid sliding shown in (d). Image color is from blue to red, which translates to dark to light in physical terms. Unmagnified images contained both the dark (blue) interface and the light (red) base plate. Digital magnifications of 4X and 20X show 'bright spots' along the interface that we assume to be the light transmitted across an asperity. Larger asperities remained in contact throughout this portion of the loading cycle and light transmission varied in the later stages (differences between (b) and (c)).

Chapter 7

Partial slip asperity model

7.1 Background and motivation

Finite element (FE) modeling was performed using the implicit commercial software ABAQUS [1] to improve our understanding of the frictional response of an asperity population affected by the transition from slow to rapid sliding on the fault. The numerical model used the experimentally determined asperity sizes and locations from F_n = 4400 N in Figure 6.1(a)) to prescribe the geometric heterogeneity of the FE model. Asperities behaved as described by the partial slip asperity in Section 1.4.4. The reasoning behind implementing this contact model was from the observed similarities between transmitted light across the asperity as failure drew closer (Figure 6.15) and the shrinking 'partially-stuck' surface that was due to increased tractions on the asperity (see equation (1.17) and Figure 1.6(b)).

This partial slip asperity model within the FE framework enabled us to calculate heterogeneous slip distributions from a section of the fault where an experimentally observed nucleation front migrated into a 'relatively locked' section of the fault (Figure 6.9). We first studied the constitutive traction-slip relationship of a single frictional asperity within the framework of the FEs. We then modeled the interactions of multiple asperities (172 total) whose geometry and locations were prescribed by the pressure sensitive film. Our numerical study focused on the transient evolution of slow slip heterogeneity in relation to the applied normal stress within a small central section (x = 182.5 to 257.5 mm) of the fault. An understanding of how slow preslip accumulates may provide insight into the spatio-temporal foreshock distributions observed experimentally.

7.2 Single asperity response

7.2.1 Geometry and boundary constraints

Figure 7.1(a) shows the finite element domain which consisted of two areas: an elastic region (slider = $10a \times 10a \times 10a$) and a rigid base. We assumed a frictionless response, i.e. zero traction (τ = 0), for the interfacial region outside the circular asperity patch with radius a. Boundary conditions

along the interfacial surface are given in cylindrical coordinates ($r^2 = x^2 + y^2$) as follows:

$$\begin{aligned} \sigma_{zz}(r,\theta,0) &= -p; r \in (0,a); \theta \in (0,2\pi); \\ \sigma_{xz}(r,\theta,0) &= 0; r \in (a,\infty); \theta \in (0,2\pi); \\ \sigma_{yz}(r,\theta,0) &= 0; r \in (a,\infty); \theta \in (0,2\pi); \end{aligned} \tag{7.1}$$

where the pressure p is applied from the rigid base plate to the elastic slider region. The elastic region was prescribed a Young's modulus E and Poisson's ratio ν applicable to PMMA (Section 2.4). The analysis was performed in the following five steps: (*i*) the elastic region is brought into perfect/mated contact with the rigid base, (*ii*) a pressure p was applied within the circular boundary which simulated the pressure transferred normally between the contacting asperities, (*iii*) a far-field displacement boundary condition was applied in the x-direction at the top surface ($z = 10a$), and (*iv*) the side surfaces of the elastic region (Figure 7.1(a)) were prescribed traction free boundary conditions. The displacement boundary condition was applied in steps (Δ_{step}) of 1 micron from 0 to 100 µm and can be expressed as

$$\begin{aligned} u_x(x,y,10a) &= \Delta_{step}; \\ x &\in [-5a, 5a]; \\ y &\in [-5a, 5a]; \\ \Delta_{step} &\in 0,1,2,3,\ldots,100\,\mu m. \end{aligned} \tag{7.2}$$

7.2.2 Constitutive relationship for a single partial slip asperity

The elastic region was modeled as a classical Hookean isotropic elastic medium [177, 57, 13]. A total of 115,695 linear tetrahedral elements (C3D4) were used to model the elastic region. The incremental elastic strains are given by equation (3.1). Contact elements were given two types of constitutive responses. These relations, shown in Figure 7.1(b), accounted for the frictional shear stress (τ) response and are defined through the relative tangential slip (δ) and a shear stiffness (k_s). Elements interior to the asperity domain were given a Coulomb-type frictional response, whereas the surrounding regions were maintained at zero frictional shear stress. The ABAQUS code adopted a finite sliding computational algorithm to calculate the slip displacements occurring along the interface. The relationship between the contact shear stress and relative shear deformation was

$$\tau = k_s \delta \tag{7.3}$$

for

$$\tau < \mu\sigma^*, \tag{7.4}$$

where σ^* is the normal stress on the individual element and the shear stiffness $k_s = \mu\sigma^*/\gamma_{crit}$. The local coefficient of friction μ (see adhesive theory in section 1.4.1) was chosen to be 0.5 and the maximum elastic slip distance γ_{crit} was specified to be a function of the characteristic length of the element (length scale). In our model, maximum elastic slip distance (γ_{crit}) was set to 0.005 times the element characteristic dimension (i.e. length scale of an element [1]). Asperities were constrained to have 20 elements along the periphery. The maximum elastic slip distance was, therefore, a function of the asperity size. Unloading a frictional element that had previously experienced sliding; i.e. the element observed a decrease in shear stress levels below the threshold

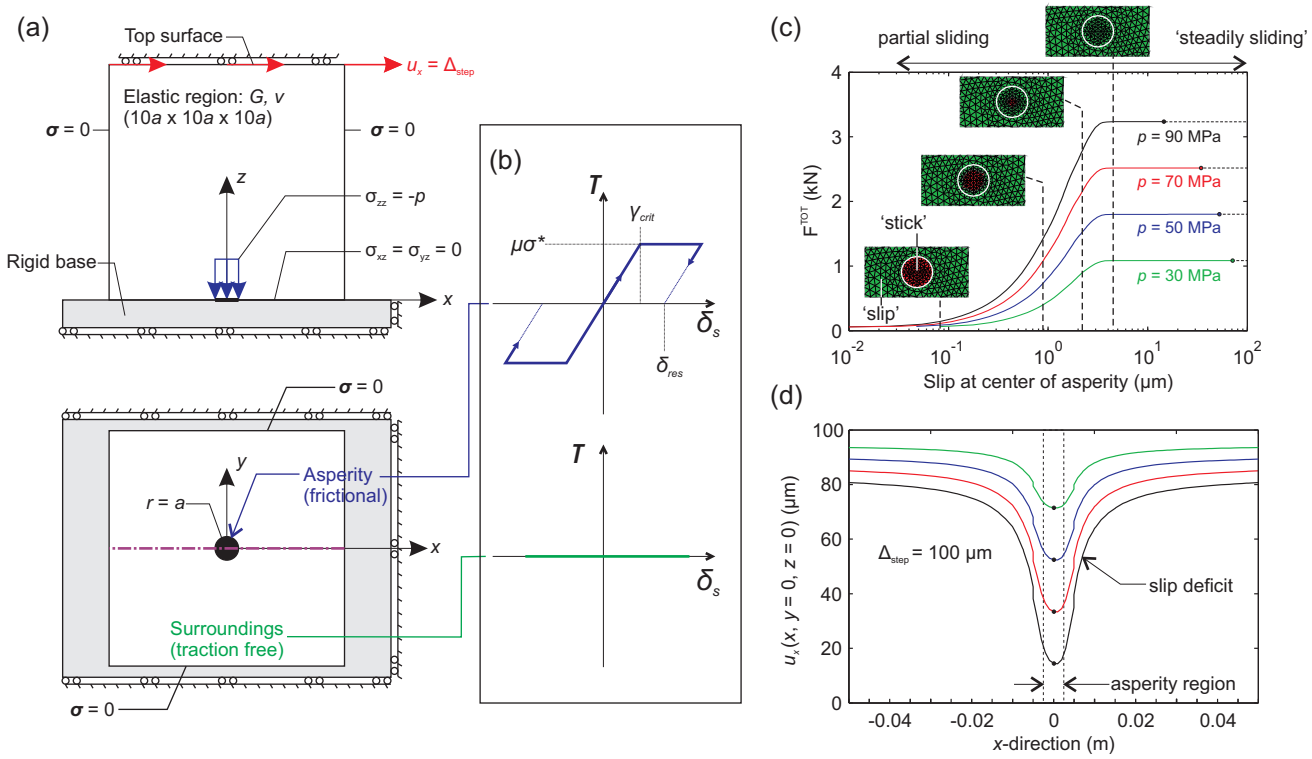

Figure 7.1: Discrete quasi-static asperity calibration model. (a) A circular asperity was prescribed a finite frictional relationship and the surroundings were frictionless. Normal pressure p (blue arrows) was applied to the asperity followed by the quasi-static far-field displacements (red arrows). (b) Constitutive frictional relations prescribed within the asperity (blue) and the surroundings (green). (c) Constitutive response for a circular asperity composed of 20 elements along its periphery for various levels of normal stress. As the far-field displacement Δ_{step} increased, so did the total shearing force F_{TOT} and the asperity experienced partial slip from its periphery to the center. (d) Slip deficit caused by the asperity due to Δ_{step} = 100 μm for a variety of applied normal pressure.

given by equation (7.4), would allow for the retention of a residual amount of slip δ_{res} (Figure 7.1(b)). For simplicity, deformations experienced along the interface were constrained to movements only along the interface (x- and y-directions) with out-of-plane deformations (z-direction) were set to zero (i.e. no dilatation).

7.2.3 Results for calibration model

According to planar contact theory [46, 51, 50], when a shear force is monotonically increased along the discontinuity, a circular asperity under a constant normal load experiences partial slip beginning at the outer edge of the contact circle and propagating inward as the shear stress is increased [46]. In Figure 7.1(c) contact elements initially remain unloaded and in a 'stuck' (red) regime. As the far-field displacement (Δ_{step}) is increased, the total force supported by the asperity

increases and, based on equation (7.4), when the element shear stress exceeds $\mu\sigma^*$, that element enters a 'sliding' (green) regime. Due to the geometry and loading conditions on the asperity, elements entered the 'sliding' regime from the periphery towards the center. Once all elements had entered the 'sliding' regime, the asperity was considered to be in 'steady sliding' and a further increase in the far-field displacement would not result in increased shear stress along the contact region. We therefore defined the 'partial sliding' regime to be when an asperity had any element that remained 'stuck'. For Figure 7.1(c), slip at the center of the asperity was measured versus the total shear force integrated along the fault. A total of four levels of pressure were applied and the corresponding shear responses recorded. As expected, increased asperity pressure resulted in increased asperity stiffness, similar to the potential energy that is stored in a spring. We measured the energy stored by the asperity as the area under the curve in Figure 7.1(c). As the normal pressure increased the potential energy stored by the asperity grew linearly. The asperity under p = 70 MPa, 50 MPa and 30 MPa stored 77.17 %, 54.7 % and 32.5 %, respectively, of the energy that could be stored by the asperity when subjected to p = 90 MPa. As an estimate for the validity of the model, the total force supported in the 'steady sliding' regime was compared to the maximum theoretical shearing force of a uniformly loaded asperity of radius a subjected to a squeezing pressure p (i.e. $\mu p \pi a^2$) which varied between 4.2 and 1.5%. Figure 7.1(d) shows the displacements along the transect bisecting the contact region (y = 0 mm), at the final loading step (i.e. Δ_{step} = 100 µm). At this step, the asperity had entered the 'steadily sliding' regime for each level of normal pressure. The asperity caused a slip deficit due to its ability to support shear loads, both of which increased as a function of the normal pressure.

7.2.4 Asperity size and shear response

The effect of asperity size is examined in this section and asperities with radii of r = 2.5 mm and r = 0.25 mm are compared in Figure 7.2. The maximum elastic slip distance γ_{crit} was 0.005 times that of the characteristic surface dimension and the coefficient of friction was μ = 0.5 for both cases. Figure 7.2 shows the log-log result between the slip at the center of the asperity versus the total shearing force F_{TOT}. We defined the critical slip distance, R_c, as the amount of slip sustained at the center of the asperity in order for it to enter the 'steady sliding' regime. Smaller asperities experienced a scaled response to their respective applied pressures: (*i*) they accommodated less shear force, (*ii*) they caused less slip deficit and (*iii*) they entered the 'steady sliding' regime at lower levels of shear displacements.

7.2.5 Multiple asperity interface

The computational mesh used for the multiple asperity model is shown in Figure 7.3(a). It was composed of 201,726 linear tetrahedral elements (C3D4). As in the calibration model, the interface was not allowed to separate from the rigid base (not shown in Figure 7.3(a)). Shear stress along the fault was increased by driving the far-field displacement ($u_x = \Delta_{step}$) shown by red arrows in Figure 7.3(a). The model had the same elastic properties as in the single asperity calibration models (E and ν) and incremental strains were again computed using equation (3.1).

Information on the geometry and locations of asperities measured from the pressure sensitive film was used in the model, specifically the distribution from F_n = 4400 N in Figure 6.1(a). A small section from these asperity measurements was imported directly into ABAQUS. Individual asper-

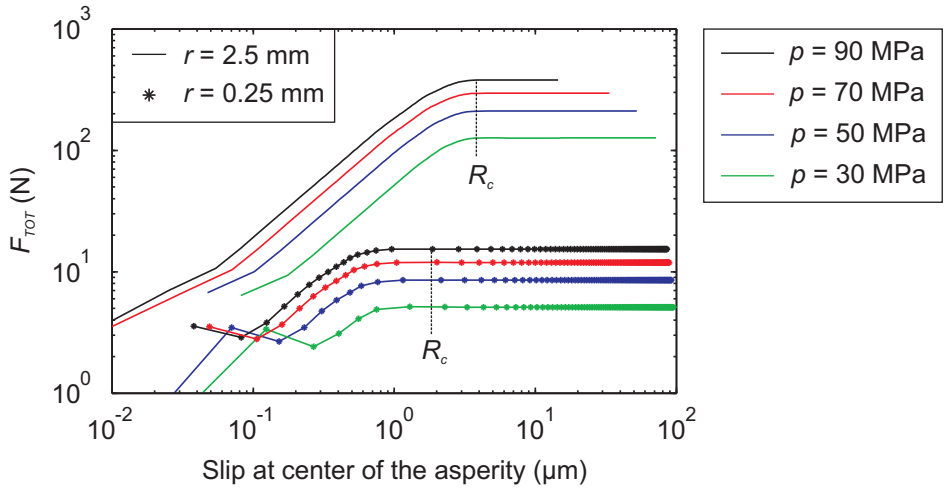

Figure 7.2: Separate numerical results for two asperities of different sizes at various normal pressures p and subjected to the far-field displacements defined by equation (7.2).

ities were given an 'equivalent circular area' representation. Due to computational constraints, only a small section of the interface (dimensions L = 75 mm x W = 12.7 mm) was numerically modeled. The off-fault distance in the z-direction was B = 100 mm. Pressure sensitive film measurements of the initial contact distribution between x = 182.5 mm to 257.5 mm were used to define the asperities in the computational model.

The interface shown in Figure 7.4(a) is composed of 172 circular asperities (black) surrounded by the frictionless interface (white). Due to computational restrictions only larger asperities with areas exceeding 0.2 mm^2 were modeled. Simulations for a range of normal asperity pressures were conducted (p = 50, 70, 90 MPa) where each asperity had the same prescribed pressure across the whole interface. For each applied normal stress level, we were able to induce 'steadily sliding' conditions (i.e. no 'stuck' elements) by increasing the far-field displacement Δ_{step} from 0 to 100 μm in 1 μm increments.

7.3 Numerical results

7.3.1 Local quasi-static transition from 'stick' to 'slip'

Figure 7.4(b) shows snapshots of the quasi-static evolution of contact patches from *stick* (red) to *sliding* (green) for various levels of far-field displacements (Δ_{step}) at a contact pressure p = 90 MPa. These simulation are strictly quasi-static and we defined a transient portion of the simulation as loading steps where any interfacial element remained in the *stuck* (red) state. Steady state was defined when all elements on all asperities experienced pure *sliding*, i.e. satisfied equations (7.3) and (7.4), discussed previously. Once the system had attained steady state, no changes in the deformation gradient [177] were observed. This meant that any increase in far-field displacement resulted in no change in the shear force and an increased in slip along the interface.

Locations and sizes of asperities were taken directly from the pressure sensitive film; smaller

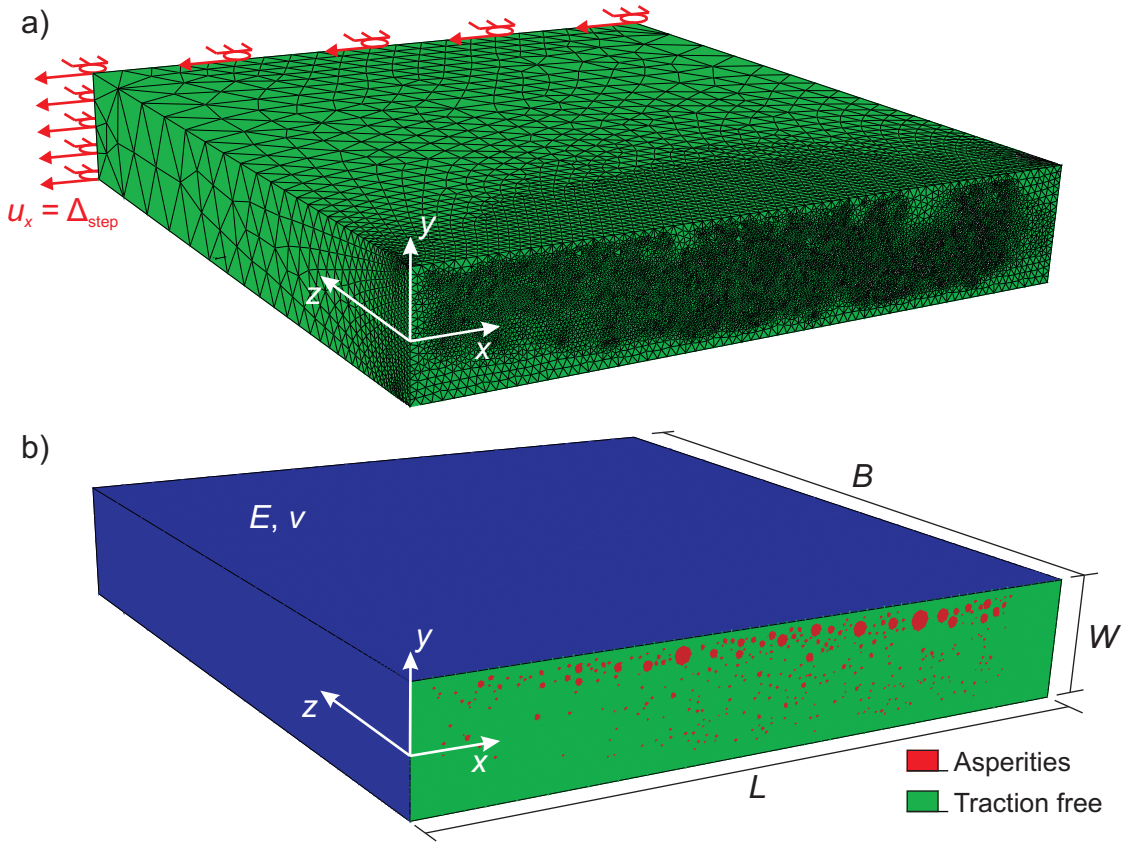

Figure 7.3: (a) The computational mesh and far-field loading conditions (u_x) use to increase shear stresses along the frictional interface. (b) The frictional interface with asperity sizes and locations taken from the pressure sensitive film.

asperities occupied the lower ($y < 0$) section of the fault. From section 7.2.4, we know that smaller contacts exhibit smaller critical slip distances, R_c, and these asperities entered a steadily *sliding* regime before the larger asperities, which dominated the upper section of the fault ($y > 0$). For the loading step corresponding to Δ_{step} = 36 µm, the lower section of the fault had entered the *sliding* regime while the upper section remained partially locked. At this time, the 'locked' upper section of the fault was loaded by two mechanisms: (*i*) the increase in far-field displacement Δ_{step} and (*ii*) the increase in slip across the asperity populations along the lower section (described by the contour lines in Figure 7.4(b)). As the far-field displacement increased, individual contacts in the upper 'locked' region entered the steady sliding regime. The numbered asperities in Figure 7.4(a) represent the ascending sequence of the last 10 asperities to enter the steady sliding regime as the far-field displacement was increased. In this model, the spatial ordering did not align itself sequentially in the direction of shear loading due to the heterogeneity of asperity distributions (sizes and locations) – a possible indication of the elastic, off-fault communication occurring between the leading and trailing region of the asperity population shown here.

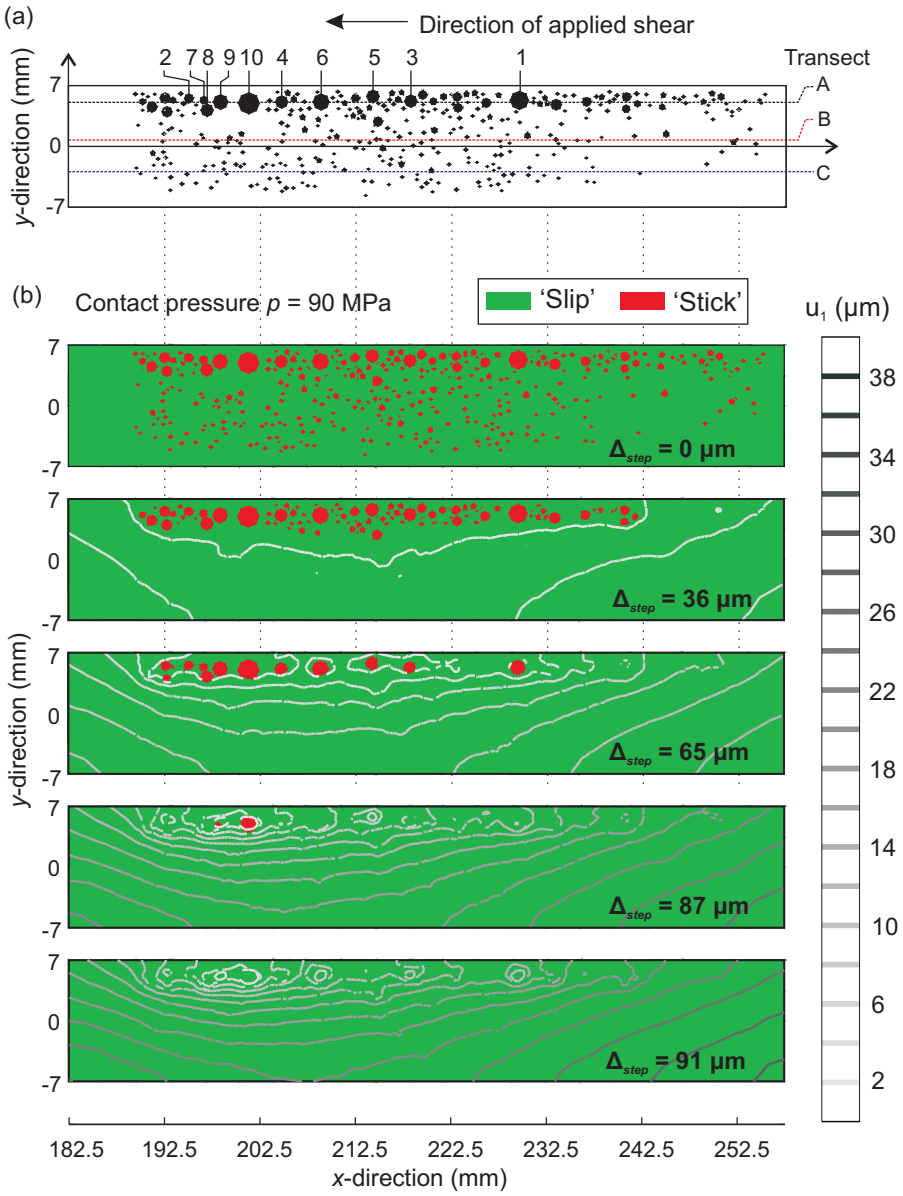

Figure 7.4: Results from the multiple asperity simulation in which locations and sizes of asperities were defined using the contact information obtained from the pressure sensitive film. **(a)** The model consisted of 172 equivalent-area circular asperities along the interfacial region between x = 182.5 to 257.5 mm. The numbered asperities correspond to the final 10 asperities that transitioned from partial to steady sliding in ascending order with increasing quasi-static step displacements. **(b)** Results of the simulation calculated at a constant contact pressure of p = 90 MPa. Contour lines define the displacement field at four far-field displacement steps (Δ_{step}).

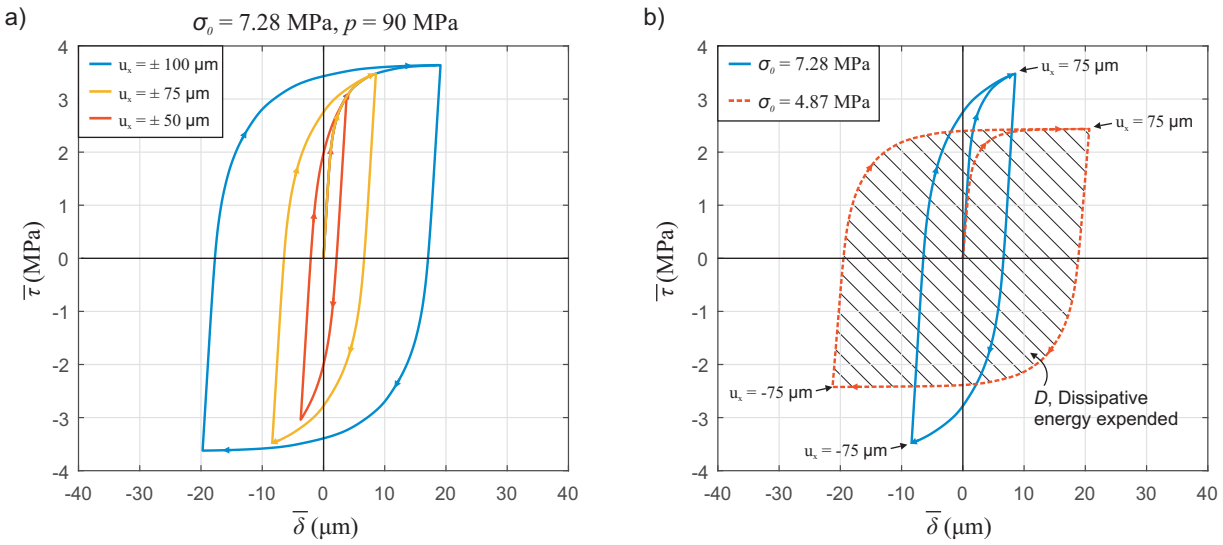

Figure 7.5: **(a)** Traction-slip relationship for the fault confined to the same normal stress but cyclically loaded to $u_x = \pm$ 100 µm (blue line), $\pm$ 75 µm (yellow line) and $\pm$ 75 µm (yellow line) **(b)** The effect of normal stress (i.e. asperity pressure) on the traction-slip relationship for identical levels of cyclical loading.

7.3.2 Bulk constitutive relationship for a population of asperities

The non-linear constitutive relationship between average shear stress $\bar{\tau}$ to average slip $\bar{\delta}$ is discussed for multiple asperities that were examined during a cyclical loading cycle. The average slip $\bar{\delta}$ was calculated as the average magnitude of slip between the x- and y-directions (i.e. $\bar{\delta}^2 = \bar{\delta_x}^2 + \bar{\delta_y}^2$) for every integration point along the interface. We assumed that there is no dilatation and $\delta_z = 0$. The average shear stress $\bar{\tau}$ was calculated as the average magnitude of tractions between the zx- and yz-directions (i.e. $\bar{\tau}^2 = \bar{\tau}_{zx}^2 + \bar{\tau}_{yz}^2$) for every integration point along the interface.

The interface was loaded in a cyclical manner; the far-field was first displaced to u_x = 75 µm, then unloaded to u_x = - 75 µm and, finally, re-loaded to u_x = 75 µm by 1 µm increments per time step. Figure 7.5(a) shows the relationship between average shear stress and average slip along the fault for a nominal normal force (σ_0 = 7.28 MPa) caused by an asperity pressure p = 90 MPa. For the case where cycling occurs between $u_x = \pm$ 100 µm (blue line), the slope of shear stress with respect to sliding becomes zero (i.e. $d\bar{\tau}/d\bar{\delta}$ = 0) at the end of the first loading cycle. This is indicative of 'full-sliding' conditions over the entire fault: i.e. all asperities along the interface have entered sliding. The level of residual slip δ_{res} was increased when the fault was loaded to a greater extent in the far-field. The traction-slip response follows a hysteresis loop where the bounding area D represents the dissipative energy expended (see hatched region in Figure 7.5(b)). Larger values of D are apparent when more frictional sliding occurs along the interface. Figure 7.5(b) shows the traction-slip relationship when the fault was confined to lower normal stresses σ_0 and the same amount of far-field loading was applied. The fault at the lower normal stress (dashed-line in Figure 7.5(b)) entered full sliding, incurred more residual slip and expended more dissipative energy.

7.3.3 Improvements to multi-asperity numerical model

The non-sequential transition of asperities from *sitck* to *slip* in the direction of shear loading showed attributes similar to the spatio-temporal distributions of foreshocks shown in Figure 6.12. This is also seen with foreshock distributions such as those presented in Figure 7.6(a). Here a foreshock sequence was superimposed over the measurements of normal stress taken from the pressure sensitive film. Figure 7.6(b) gives the acoustic emission data from multiple sensors showing the delay times between foreshocks while Figure 7.6(c) shows the slight variation in foreshock signals. In Figure 7.6(c), each foreshock has been aligned about the P wave arrivals. The inset image of Figure 7.6(a) shows that the foreshock sequence does not propagate sequentially in the direction of slip (i.e. top to bottom). Foreshocks also clustered on the side of the fault with larger asperities. In the numerical model, the side of the fault exhibiting larger asperities (i.e. $y > 0$) had asperities that transitioned to sliding in a similar manner (see numbering sequence in Figure 7.4(a)). For a foreshock to develop on an asperity, conditions must be appropriate to allow for local instability (e.g. equation (1.9)). While the numerical model described here cannot currently predict local dynamic effects from a foreshock (elastodynamic wave propagation), it can simulate the quasi-static stress evolution due to the interactions of multiple partial slipping asperities. Future work should attempt to explain the effects of the sudden removal of a shear stress bearing asperity in the numerical model. The stress perturbations from a foreshock on neighboring distributions of asperities may help explain: (*i*) whether a foreshock was triggered due to previous foreshock stress perturbations (i.e. the *cascade model*) or (*ii*) is the stress perturbation insufficient and the subsequent foreshock is due to the overall growth of the nucleation region (i.e. the *preslip model*). Comparison of numerical models with the observed experimental foreshock sequences (see Figure 7.6(a)) may help in deciding which model appropriately describes the nucleation seen in laboratory tests.

7.3.4 Variations in the slip displacement fields

Figure 7.7(a) shows values of slip δ_1, in the direction of applied shear, along three Transects: A (y = 5 mm), B (y = 0.5 mm) and C (y = -3 mm), at the contact pressure p = 90 MPa, for a far-field displacement step Δ_{step} = 91 µm. At this displacement step the fault was in the steadily *sliding* regime. The locations of transects A, B, and C are shown graphically in Figure 7.4(a). Transect C bisected the lower section of the fault composed of smaller contacts, which transitioned to steadily *sliding* conditions more rapidly than Transects A and B. Transect C also displayed a smoother distribution of slip and accrued more total slip. Transect A displayed a more tortuous distribution of slip u_x due to the larger slip shadow caused by larger asperities located along this transect. Figure 7.7(b) examines the effect of the normal pressure on the scalar valued function strain energy density ($SED = (1/E)\sigma^2$, where σ is the stress field and E is the Young's modulus) that accumulated along Transect A for asperity normal pressures (p = 50 and 90 MPa). These calculations were made once the interface had entered the steadily *sliding* regime. At this point the strain energy density could not change (deformation gradient was zero) and we computed higher levels of strain energy density for the larger contact pressure. This was expected since larger pressures result in more distortion to the displacement field (see section 7.2.3).

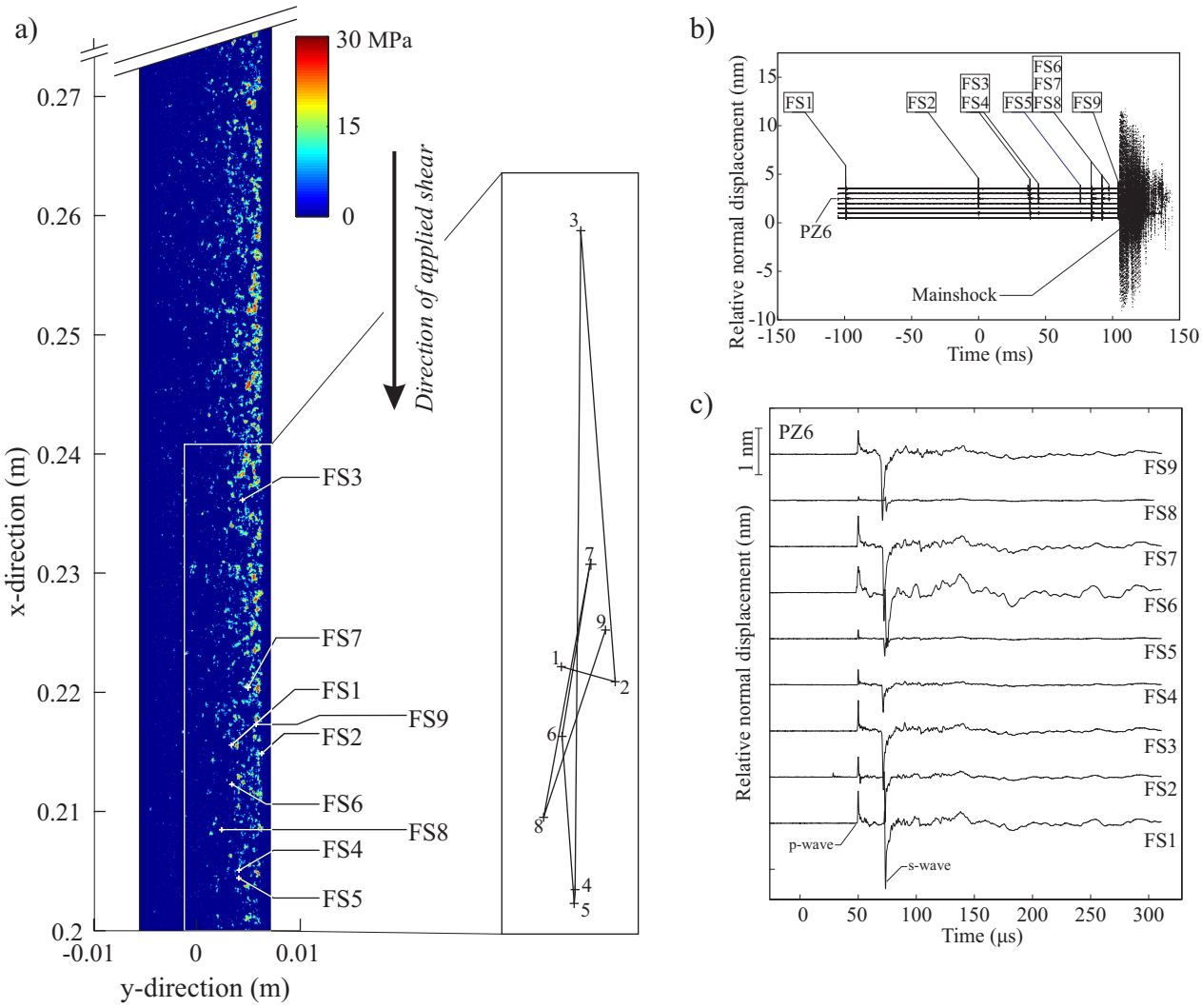

Figure 7.6: **(a)** Locations of the foreshocks determined using P wave travel times from AE sensors. The locations were superimposed on the pressure measurements obtained from the pressure sensitive film. Locations exhibiting higher normal stress appear red while the blue background assumes no normal stress was transferred (i.e. no contact occurred). The inlay shows an enlarged view of the spatio-temporal movement of the foreshock sequence where the distribution appears to be random in space. **(b)** Acoustic emission data showing the delay times between each foreshock over multiple sensors. **(c)** Foreshocks as observed on sensor PZ6. Signals have been aligned about their P wave arrival.

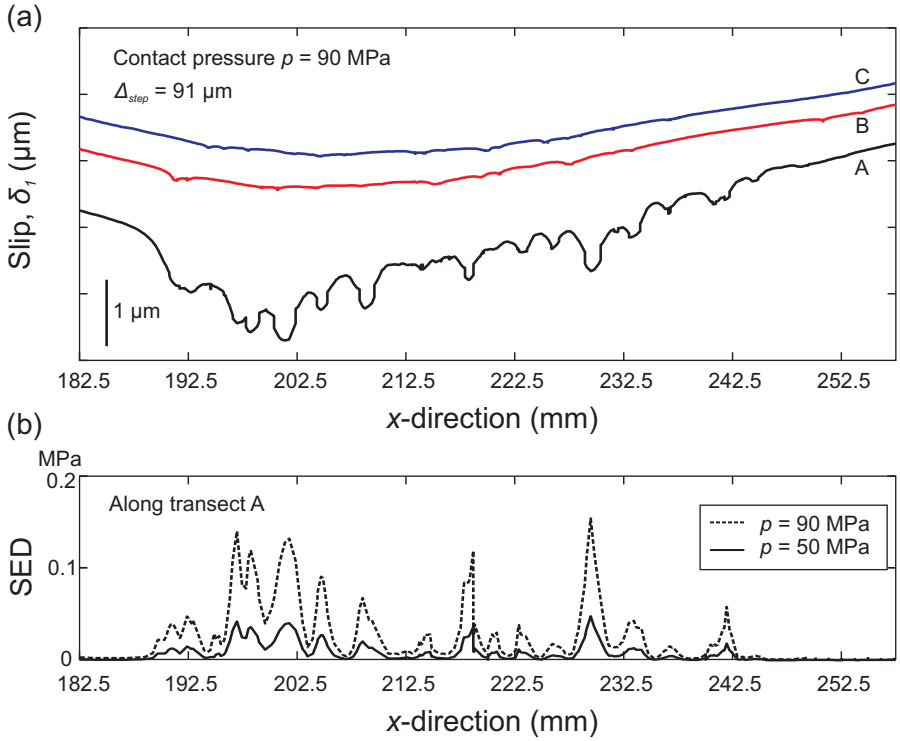

Figure 7.7: **(a)** Slip in the x-direction along three transects taken at Δ_{step} = 91 μm. **(b)** An increase in strain energy density (SED), in the x-direction along transect A, with an increase in applied normal pressure p.

Chapter 8

Discussion

We have proposed that the study of shear rupture in the laboratory is important in understanding the underlying characteristics of earthquakes and faulting in nature. A direct shear experiment was used to study the dynamic evolution of sliding along a frictional fault. Dynamic evolution can be explained using the nucleation theory presented in Section 1.3.1. The study of faulting and friction in the laboratory has not changed dramatically since the seminal studies [e.g., 61]. However, the new sensors employed here have enabled us to improve our understanding of the frictional processes, specifically premonitory seismicity. In the past, laboratory studies have given us a more refined understanding of fault stress states directly observed from field investigations. The concurrent nature of these two fields of study, i.e. rock mechanics and seismology, have been essential in better assessing seismic hazard along naturally occurring faults. Field studies can now find premonitory seismicity (foreshocks, swarm-like foreshocks, non-volcanic tremor, etc.) prior to the main shock, using better sensors and data processing that allow us to see premonitory features that were not previously detectable. Here we examine what appears to be similar preparatory seismicity in a laboratory setting.

We observed preparatory seismicity in the form of foreshocks that appeared at the fringe of a growing nucleation region. Foreshocks were generated by the rapid, localized failure of asperities within the breakdown region of the nucleation region. This was confirmed using direct observations from a video camera (Figure 6.15). To develop a better understanding of why asperities may (or may not) develop foreshocks we examine local asperity stresses using a pressure sensitive film. This allowed us to locate, size and measure normal stress on individual asperities in the breakdown region. In terms of contact mechanics, asperities form due to rough-rough surface interactions. We used microscopy (Figures 6.7 and 6.8) to further understand how asperities may form on a surface that exhibits a multi-scale roughness. If we have a better comprehension of how asperities form it will provide insight into the spatio-temporal distributions of foreshocks in sequences leading up to the main shock and their dependence on the normal loading conditions.

8.1 A standard shear stiffness calculation

Using the results from Figure 6.2 we investigated the manner in which asperities are formed in bulk (macroscopically) versus the applied normal force. From the pressure sensitive film we were able confirm that the number of asperities N along the interface grows linearly with the in-

creasing normal load F_n. Berthoude and Baumberger [25] found similar results and applied the Greenwood-Williamson (GW) [78] to provide estimates of shear stiffness due to multiple asperity interactions. Building from the single Hertzian contact in section 1.4.3, the elastic shear stiffness of a single circular contact patch is given as $\kappa_s = 4Ga/(2-\nu)$, assuming no-slip under the application of shear loads [125, 87]. (**NB**: This solution differs from the partial slip asperity described in Section 1.4.4 and modeled in Section 7.) As long as the micro-contacts are elastically independent, the total interfacial stiffness K_s can be calculated as the superposition of the individual stiffnesses: i.e.,

$$K_s = \frac{4G}{2-\nu} N \langle a \rangle \tag{8.1}$$

where G is the shear modulus, ν is the Poisson's ratio, N is the number of asperities and $\langle a \rangle$ is the average asperity radius. The shear modulus and Poisson's ratio were taken from Table 2.4 and the number of asperities N and the average asperity radius $\langle a \rangle$ were obtained from Figures 6.2(a) and (b), respectively. From equation (8.1), the shear stiffness ranged from K_s = 202 N/µm at normal force $F_r \sim$ 350 N and 923 N/µm for $F_r \sim$ 1550 N. These are comparable to estimates given in Berthoude and Baumberger [25] for PMMA. Extrapolating their results we found an interfacial stiffness of $K_s \sim$ 105 N/µm at $F_r \sim$ 350 N and $K_s \sim$ 465 N/µm for $F_r \sim$ 1550 N. The discrepancies in stiffness may be due to the abrasive media used condition the surfaces in the separate studies. The mean particle size in our abrasive media was $\sim$ 220-440 µm in diameter compared to 23 µm in Berthoude and Baumberger [25]. The RMS roughness found in our studied was $\sim$ 3.85 µm (for the mature faulting surface) compared to 1.3 µm. Next we examined the possible limitations of equation (8.1) in that the contacts must be elastically independent for superposition to be valid.

8.2 Potential limitations of the Greenwood-Williamson (GW) model

A major assumption in the GW model is that contacts are sparse and separated. Neighboring contacts must be much further away than the average asperity radius. From a visual inspection of the small section of the pressure sensitive film used in this study (Figures 6.1(a) and 6.3) it appears that this is not the case. To calculate the average asperity separation distance in the *seismogenic* region, we discretized the region into square cells with a side length of L_{grid} = 4 mm. Figure 8.1(a) shows the asperity distribution within the gray *seismogenic* region when the fault was loaded to F_n = 4400 N. The *seismogenic* region here was slightly larger, from x = 140 to 300 mm, for divisional purposes. In Figure 8.1(a), we see a square gridded region composed of 40 x 3 cells. Figure 8.1(b) shows a schematic view of the actual asperities distributed within a single cell. Each cell has two parameters: (i) the total number of asperities N_{grid} and (ii) the total sum of the real contact area A_{grid}. Using these values we can calculate the average asperity radius in the specified grid cell $\bar{a}_{grid} = \sqrt{A_{grid}/\pi N_{grid}}$. To calculate the average asperity separation distance we must distribute the N_{grid} equal sized asperities (having constant radius $\bar{a}_{grid}$) evenly throughout the square cell. This is achieved using optimization techniques. Optimal packing of equally sized circles into a square is a non-trivial problem and the solution is given by the *Travelling Salesman Problem* [e.g., 72]. Specht [169] has calculated the solutions to this problem up to N_{grid} = 10,000 in a unit square. Figure 8.1(c) shows the separation distance d_{sep}, which depends on the number of asperities N_{grid} – a known quantity from our measurements.

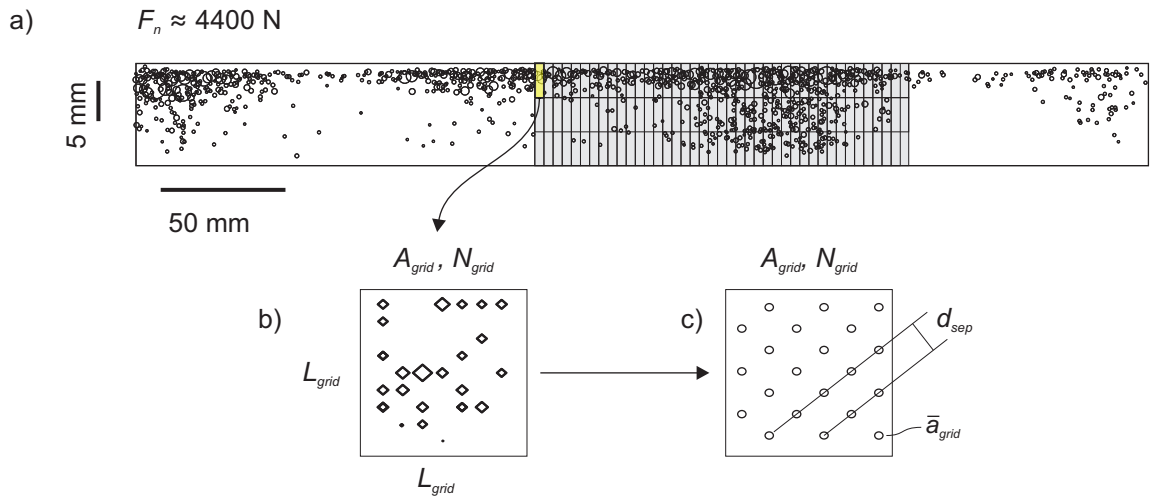

Figure 8.1: Average asperity separation distance calculation. **(a)** Asperity contact measurements from the pressure sensitive film are examined in the seismogenic zone (gray region). This is discretized into 40 x 3 square cells with side length L_{grid}. **(b)** One cell contains N_{grid} asperities with a total real contact area of A_{grid}. From this we can calculate the average asperity radius $\bar{a}_{grid}$. **(c)** Using the cellular packing solutions from Specht [169] we can calculate the optimal separation distance d_{sep} for each cell.

Using the metrics for each cell in the *seismogenic* zone, we calculated the asperity separation distances at normal forces of F_n = 4400 N. The average number of asperities over all cells was $\bar{N}_{grid}$ = 117, which ranged from 43 to 251 asperities. The average equivalent radius of the asperities in all cells was $\bar{a}_{grid}$ = 0.0553 mm, which ranged from 0.031 mm to 0.12 mm. Using this and the tabular packing data [169] we found $d_{sep}/\bar{a}_{grid}$ = 9.33 and it ranged from 3.95 to 19.75. At lower normal forces (F_n =2000 N), we found $d_{sep}/\bar{a}_{grid}$ = 14.66, with a range from 4.97 to 76.90. As expected, the ratio of separation distance to average asperity radius increased as the fault was unloaded.

Interactions between asperities through the off-fault material becomes an issue at small separation distances – the 'long-range' elastic interactions are apparent up to $\sim$ 16 asperity radii according to Yastrebov [184]. Asperity separation distances in the *seismogenic* region of our experimental fault, even at the lower normal loads, were (on average) insufficient to neglect the 'long-range', off-fault elastic interactions. Tribological study of the local interactions between closely packed asperities are being investigated more often [e.g., 52, 2]. These interactions may affect sliding dynamics during the premonitory phase and therefore cannot be ignored as is the case for the GW model (see Section 1.4.5). The work pioneered by Tabor [33] and Archard [7], suggest that typical separation distances for multicontact interfaces are much larger $\sim$ 100 radii – which has been confirmed by direct observations [63, 64]. Discrepancies between these studies and that presented here may be influenced by the surface roughness; surfaces in the aforementioned studies are much smoother ($\sim$ 0.1 µm RMS) than the long length scale roughness ($\sim$ 5 µm RMS roughness) seen in this study (see Figure 6.8). Whether asperities on the fault communicate elastically or are isolated will affect the local stiffness of the fault. Equation (8.1) may be insufficient in characterizing

surfaces that display the level of heterogeneity in asperities contact shown in Figure 6.1(a).

8.3 Improved understanding *effective heterogeneity* using contact measurements

Various models have been implemented to study nucleation processes along natural faults [70, 23, 68]. Rheological differences within a nucleation zone are believed to control this transition between two end-member models: the "preslip" and "cascade" models. McLaskey and Lockner [120] have studied the relationship between premonitory slip and foreshocks in terms of these nucleation models. Heterogeneity is considered to be an essential ingredient for the presence of preslip and aseismic transients in nature [24, 136]. Geologic heterogeneity may be influenced by a number of factors in the 'subduction channel shear zone' [144]. Characterization of the faulting structure and the degree of heterogeneity remains elusive to scientists. Within the rock mass physical quantities, e.g., temperature, fluid pressure, elastic/hydraulic properties, etc., cause differences in rheology that are necessary for aseismic transients. The total interaction between these quantities causes an *effective heterogeneity* [62]. Rheological differences in this study are due to stiffness gradients from heterogeneous distributions of asperities. The heterogeneous distribution of slip seen in the numerical model (Figure 7.4) shows the influence of both off-fault and on-fault asperity interactions in the context of the partial slip asperity framework. More numerical studies should be performed to understand how a variety of asperity distributions (with the same ratio of real to nominal contact area A_r/A_0) affect the bulk constitutive behavior (i.e. relationship in Figure 7.5).

8.4 Effects of multiscale roughness

The overall shape of our fault asperities are 'flat-topped' islands within a large flat sea, as seen in Figures 6.5 and 6.8, and are characterized over these longer length scales with a Hurst exponent of ~ 0.60. Along the tops of individual asperities themselves (e.g. Figure 6.7(a)) the surfaces were smoother, characterized by Hurst exponent ~ 0.27. It is possible that the asperities formed along our fault can be described using the two roughness-length scales (long and short length scales). Nayak [133] used two roughness wavelengths to define the formation of contacts along a fault: z_1 and z_2. Larger contact patches form based upon a rougher z_1-wavelength: i.e., the Hurst exponent given at longer (low frequency) spatial scales H_{low}. Higher frequency spatial fluctuations cause variations along actual asperities and is given by the Hurst exponents H_{per} = 0.32 and H_{par} = 0.22 determined from the optical profilometry (Section 6.2) on single asperities. Baumberger and Caroli [18] believe that individual asperities form due to smoother interacting surfaces, which they refer to as *nanometric* roughness, whereas separation distances (d_{sep}) between asperities are from rougher, *micrometric* range. 'Holes' (i.e., regions with lower to no normal stress) within larger asperities are due to the destructive interference of the two roughnesses. An example of a 'hole' within a larger asperity is shown in Detail B of Figure 2.2. If we presume that shear strength assumptions of adhesive friction apply (see Section 1.4.1), increased normal stress leads to stronger asperities (see equations (1.10) – (1.12)) capable of increased resistance to shear stress.

These two varying levels of roughness dictate the strength heterogeneity and may give insight into features surrounding precursory seismicity (e.g. foreshocks), slow slip accumulation and

asperity interactions (both static and dynamic stress perturbations) during earthquake nucleation. Normal stress fluctuations defined by the long length scale roughness, may prove important when understanding how asperities interact during the slow slip accumulation phase (see Section 8.2). Seismic radiation from foreshocks produced during the rapid failure of an asperity may carry information regarding fault strength that is controlled by the shorter wavelength roughness.

8.5 Seismicity in relation to strength heterogeneities

In this study, foreshocks are caused by the failure of an asperity. While we assumed a circular representation using the Brune relationship, in fact, asperities were formed irregularly. Acoustically, foreshock signals were not smooth at times, unlike the seismic radiation predicted by Brune's circular asperity model [see also, 54]. The incoming P wave pulse (e.g. for the foreshock marked as F_n = 4400 N in Figure 6.10) displayed irregular shaped displacements, whereas Brune's model (equation (6.6)) predicts that the incoming pulse-like P and S wave should be smooth. These additional features in seismicity in this laboratory experiment may be due to the local variations in strength and the general shape of the failing asperity. Across larger asperities, such as that depicted in Figure 2.2 Detail B, the asperities formed are not circular and do not exhibit normal stress distributions consistent with many theoretical studies that have analyzed the failure of asperities in the context of fracture mechanics [e.g., 91, 88]. It appears that the roughness on individual asperities, the so-called *nanometric* junction-level roughness [18], promote the idea of smaller asperities within asperities [8, 133, 145]. This junction-level stress field (Figure 6.3) causes variations in strength that may promote/suppress the amount of stress dropped during failure.

It is important to understand seismic stress drop since this directly relates to the amplitude of the high frequency content in the stress waves emitted during an earthquake – which causes the most damage to building infrastructure [121]. Even though foreshocks are not considered to be tremendously damaging (compared to the main shock), the level of stress perturbations may influence their relationship to nucleation of the main shock. A foreshock may have two types of stress perturbations upon failure: (i) static [91] and (ii) dynamic [90]. If static and dynamic stress perturbations from a foreshock lead to triggering of the subsequent foreshock, nucleation follows the *breakaway* model (Section 1.3.1). If a foreshock is unable to trigger the subsequent foreshock via its stress perturbations, and more foreshocks are still observed, nucleation is described by the *preslip* model. Nucleation processes are then results of a slowly growing of a nucleation region (see Section 1.3.1) described by the mechanical model presented in equations (1.3) to (1.9).

In our experiments, the foreshock's static and dynamic stress perturbations are likely to be influenced by the physical size (length scale) and strength of the asperity. Both features are controlled by the *nanometric* junction-level roughness (Figure 6.7). Conversely, asperity-asperity interactions, occurring due to longer length scale roughness (Figure 6.8), may control aspects of the overall growth of the nucleation region in the *preslip* model. The breakdown (cohesive) region is composed of asperities formed due to this longer roughness length scale. This concept is described schematically in Figure 1.4(b).

8.6 Foreshock magnitude and the dependence on normal stress

We see in Figures 6.10(b) and 6.12(b) that the peak ground displacement (PGD) for foreshocks are, for the most part, larger with the application of higher levels of normal force F_n. Acoustically determined foreshock source radii were calculated from the pulse duration of the foreshock signals, having values from $\sim$ 0.21 to 1.09 mm. As noted in Section 7.3.4, an increase in normal stress on an asperity would increase the local stiffness and its ability to store potential energy. Consider two asperities of identical radii, subjected to either a high or low normal stress. By forcing each asperity to identical ratios of 'partial sliding', the shear force F_{TOT} sustained along the interface would be less for the lower normal stresses p. Furthermore, the potential for an asperity to accommodate strain energy is proportional to the level of normal stress applied. If these two independent asperities suddenly failed at the same point, the asperity under higher normal stress would have stored more potential energy. Assuming that the seismic efficiency (i.e. the amount of potential energy transformed into dynamically radiated stress waves [3]), was equal in both cases, the asperities that stored more strain energy would release more energy during a seismic event.

8.7 Nucleation Processes

8.7.1 Experimental bulk rupture growth resistance

As noted in Section 6.3.2, we observed that the bulk shear strain ϵ_s increased with additional normal force F_n. At higher normal loads the bulk shear stress (i.e. the total shearing force over the nominal contact area F_s/A_0) along the fault increased. The additional increase in normal force resulted in proportionally higher levels of total bulk shear force (F_s) at failure while the nominal contact area A ($\approx$ 400 mm x 12.7 mm) remained constant. From Figures 6.9(b) and (c), we see that for an increase in applied normal force the gradient in slip increased. The gradient in slip is also a measure of the bulk shear strain ϵ_s from equation (6.4). The bulk shear stress τ_s (assuming a basic linearly elastic model) is given as $\tau_s = G \cdot \epsilon_s$, where G is the shear modulus. Under classical assumptions of frictional contact, the breakdown shear stress $\Delta\tau_b$ may be expressed as a function of the normal stress (σ) and the peak (μ_p) and residual (μ_r) coefficient of friction, i.e. $\Delta\tau_b = (\mu_p - \mu_r) \cdot \sigma$. Assuming constant coefficients of friction and shear modulus, the observed increase in shear strain within the breakdown zone can be attributed to the increase in normal stress divided by the shear modulus $\epsilon_s = (\mu_p - \mu_r) \cdot (\sigma/G)$.

It is likely that the elbow in the slip data is the location of the rupture tip of the quasi-stably growing nucleation zone (Figure 6.9). Again, the elbow in the curve indicated a normal force dependence as the tip propagated further into the relatively locked section of the slider block with a decrease in normal force. From our macroscopic observations, we expect that as the normal force was increased, the ability of the fault to resist shear rupture also increased. A schematic of the resistance of the fault to rupture, which captures the observed trends described above, is shown in Figure 8.2. For further insight into the location of the elbow, we look to the nucleation theory defined in Section 1.3.1. If we assume the simple slip-weakening model, the effective surface energy Γ (equation (1.8)) can now be expressed as a function of the normal stress (σ), the peak (μ_p) and residual (μ_r) coefficient of friction and the critical slip displacement (D_c):

$$G_c = \frac{1}{4}\Delta\tau_b \cdot D_c = \frac{1}{4}\left(\mu_p - \mu_r\right)\sigma D_c. \tag{8.2}$$

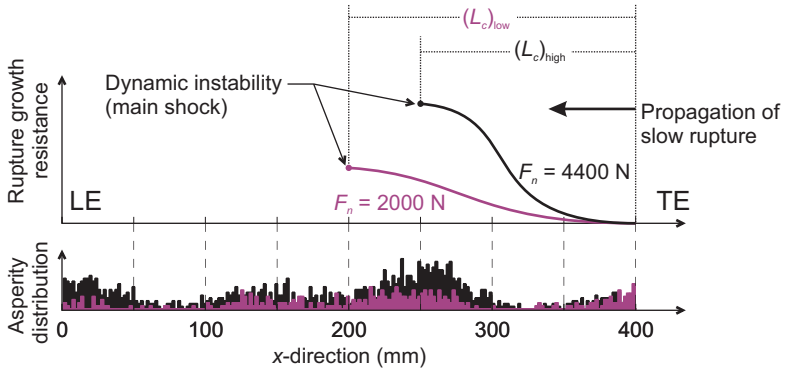

Figure 8.2: Qualitative variations in rupture growth resistance determined from the experimental observations. A slow shear rupture front propagated away from the trailing edge (TE) and its distance X_c, before the fault slipped unstably, depended on the applied normal force F_n. Below is the along-strike spatial histogram of asperities at the two normal load levels F_n = 4400 N (black) and 2000 N (magenta), taken from Figure 6.1.

We updated equation (1.9) describing the critical length scale L_c, for this particular version of the slip-weakening model. From previously, we know that peak and residual shear stresses can be represented in terms of the normal stress, i.e. $\tau_p = \mu_p\sigma$ and $\tau_r = \mu_r\sigma$. Substituting this into equation (1.9) we obtain a relationship for the critical nucleation length in terms of the normal stress, i.e.

$$L_c = \frac{1}{\pi}\left(\frac{G \cdot D_c}{\sigma}\right)\frac{(\mu_p - \mu_r)}{((\tau_i/\sigma) - \mu_r)^2}. \tag{8.3}$$

It should be noted that the critical nucleation length is inversely proportional to the normal stress, which explains why, at a lower applied normal force F_n, the elbow in the slip profiles (Figure 6.9) moved further along the interface.

While the bulk properties of the fault are characterized by the slip-weakening model, we are interested in detailed aspects that control the ability of the fault to resist rupture, specifically those at the asperity-level and their dependence on the normal force F_n. The quasi-discrete asperity model was used to link the two scales in this study. The ability of a single asperity to store potential energy is directly influenced by both its stiffness (which is controlled by the applied normal force) and the amount of slip that has accrued at that point of the loading cycle (Figure 7.1). Multiple asperities behaved in a similar fashion, as shown by the numerical simulation shown in Figure 7.4. The distribution of asperities was acquired from the pressure sensitive film in a region of the fault where the slowly propagating shear front (described above) would have had to penetrate a resistive patch of asperities.

Numerical results (Figure 7.4) show that slow slip accumulated non-uniformly across the fault; even when some larger asperities remained 'stuck', other sections of the fault experienced a bulk slip deficit of $\sim$ 36 µm (see Δ_{step} = 87 µm in Figure 7.4(b)). The maximum difference in slip along the interface once the fault had entered full sliding represents a slip deficit along the interface, which was controlled by the amount of normal force. Due to the unknown coefficient of friction μ at the asperity-level, the values of slip are somewhat arbitrary; however, the shear response

helps explain how populations of asperities resist shear rupture. When we decreased the asperity pressure to p = 40 MPa, we observed that asperities entered the sliding mode more easily (at Δ_{step} = 38 µm) and the slip deficit was reduced to 16 µm; the bulk stiffness of the fault was reduced as was its ability to resist the slow slip front. The bulk slip deficit measured in the multi-asperity model is similar to the critical slip distance D_c in the slip-weakening nucleation model. The ability of an asperity to create slip deficit (Figure 7.1(d)) is, in effect, its ability to resist shear rupture, which was dependent on the normal force.

The breakdown stress drop $\Delta\tau_b$ in the slip-weakening model is also well explained by the numerical model. As the normal pressure increased we observed an increased potential of the fault to store shear strain energy (Figure 7.7(b)). Consider two multi-asperity surfaces, with identical asperity distributions, subjected to high and low normal asperity contact pressures, respectively. To force all asperities along the interface into full-sliding, a larger amount of critical slip D_c is required and as a result, more strain energy (proportional to $\Delta\tau_b$) is accumulated along the fault at the higher normal pressure p. For a slow rupture to break down the 'stuck' asperities, a specific heterogeneous distribution of slip was required. As macroscopic slip increased, the potential for the fault to resist rupture decreased. Similarly, local potential to store shear strain energy also dropped as local slip increased.

8.7.2 Local rupture growth resistance and foreshock clustering

Local stress changes during nucleation are explained in more detail using the numerical model. Experiments showed that foreshocks were observed in a region of the fault close to where a slowly propagating shear rupture migrated into an asperity rich, 'locked' section of the fault. Foreshocks (FS) are assumed to be the local, dynamic failure of individual [115] or local clusters of asperities. While Figure 8.2 qualitatively depicts the fault resistance to rupture as smooth, in reality it is more likely to be irregularly shaped and determined by the heterogeneous distributions of asperity contacts. Numerically we observed that increasing the normal pressure on the fault increased the magnitude of potential energy stored in individual asperities (see Section 7.3.4). Once the fault was forced into the 'steady-sliding' regime, at lower pressure p, the magnitude and spatial distribution (i.e. degree of heterogeneity) in the shear strain energy field was lower. Consider a fault composed of asperities under similar levels of normal stress with similar material properties that behave as described by the quasi-discrete asperity model. If only one asperity within the asperity field failed, the static stress change [172] would cause local perturbations in the stress field [109]. The distance that these static stress perturbations propagate away from the source depends on the stress dropped, the radius (assuming a circular source), and on the ability of the fault to resist shear rupture – a normal force dependent parameter in the quasi-discrete asperity model. A fault exhibiting higher rupture resistance has the ability to support sharper gradients in the shear strain energy field, suggesting that closer populations of asperities would be able to accommodate static stress changes resulting from the sudden failure of a single asperity. Spatio-temporal foreshock distributions (Figures 6.12) support this idea; tighter clustering of foreshocks was observed at higher normal forces F_n.

8.7.3 Breakdown tip progression

Experimental evidence shows that a slow shear rupture propagated into a relatively locked region and was normal load-dependent (Figures 6.9(b) and (c)). At higher normal forces, the break-down tip velocity propagated at a slower velocity (1-3 mm/s over the last 50 s before t_{fail}) than at lower normal forces (6-9.5 mm/s at the last 25 s before t_{fail}). This observation is similar to the conceptual model put forward by Ohnaka [139] where the slowly growing crack has a nucleation length (L_c) that included a number of local asperities. We examine the manner in which foreshocks occurred and the information they convey in relation to the main shock.

Foreshock sequences have been studied as precursory phenomena to a larger main shock. Three predominant theories surrounding foreshock sequences have been postulated. In the cascade model, a small foreshock occurs which triggers the next event, eventually culminating into the main shock. In the cascade model foreshocks are triggered by static stress changes, pore fluid changes or dynamic effects. In the preslip model, nucleation occurs due an aseismic slippage region that grows until it reaches a certain size when failure occurs. Foreshocks are interpreted as localized failure within or along the fringe of the nucleating region that experiences shear stress perturbations. Our experimental observations appear to support preslip since the macroscopic motions show slip patterns that are well explained by the slip-weakening nucleation model – asperities within the growing breakdown zone fail locally based on the ongoing slippage around them [119]. In the preslip model, the stress changes from the foreshocks are incidental to the main shock failure mechanism [67]; the foreshock failure mechanism is likely to be similar to the main shock (in our experiment, foreshocks released stress in shear along the planar fault [115]). Relatively recent studies have examined the diffusional after-slip from foreshocks as a possible mechanism that triggers the main shock [84, 5]. Barbot and Fialko [14] discuss the time-dependent relaxation that controls after-slip subsequent to an earthquake (or foreshock) and find that post-seismic deformation may be due to a combination of poroelastic response, fault creep and viscous shear. In our dry-friction experiment, the poroelastic effects are absent (PMMA is a non-porous glassy polymer [11]) and any purely viscous processes would not allow for the generation of foreshocks. In our experiments any triggering of subsequent foreshocks (or main shock) due to post-seismic deformation would be due to fault creep. Fault creep following a foreshock is, in mechanical terms, localized visco-elastoplastic deformation. Ando and Imanishi [5] studied the foreshock sequence prior to the 2011 Tohoku-Oki, JA earthquake. They found that the Mw 9.0 main shock, March, 11, 2011, 14:46, was triggered by the diffusional after-slip from the Mw 7.3 foreshock, March 9, 2011, 11:45 (Japan Standard Time). The mechanism proposed was controlled by the ratio of brittle to ductile areas (i.e. strongly coupled patches to decoupled stable regions), which in our experiment would be analogous to ratios of the strong asperity patches to the non-contact regions.

In all foreshock sequences (except F_n = 2700 N, SS3) the first foreshock was located behind the main shock hypocenter in the direction of the slowly propagating rupture (Figure 6.12(b)). This is similar to the well analyzed foreshock sequences during the 2011 Tohoku-Oki, Japan earthquake [5] and the 2014 Iquique, Chile earthquake [37, 183]. Additional seismicity was recorded in our experiments; it was un-locatable but showed some spatial organization (Section 6.4.7). The majority of the additional seismicity ($\sim$ 48 % of the observed increased seismicity) originated within the trailing edge of the 'locked' section of the fault. We believe that this background seismicity in our experiment is similar to that which was present behind the Mw 7.3 foreshock, with respect to the direction of the diffusely expanding rupture front, in the Tohoku-Oki sequence [5]. These smaller,

un-locatable signals may be some form of background seismicity that is indicative of macroscopic slow slip of the relatively locked region. While this observation does not distinguish between the various mechanisms triggering foreshocks, it does show unique similarities to observations in nature.

Foreshocks increased in frequency and spatially coalesced towards the main shock hypocenter as the time to main shock decreased (Figure 6.13(a)). This observation is similar to that made by Jones and Molnar [93], who observed increased foreshock activity before major earthquakes (between 1914 to 1973). This observation supports the *preslip* model in that nucleation, characterized in part by the slip-weakening model, of the accelerating slow slip front (and larger shear stress gradients [119]) may promote foreshocks on individually stiffer asperities. Moreover, in Figure 6.12 we see that subsequent foreshocks span distances greater than 10 times their source radius. The largest source size, measured acoustically, was $R_0 \sim 1.09$ mm. Since the shear stress perturbation ($d\tau$) along the planar fault decays proportional to d^{-3} [3, 47], where d is the hypocentral distance between subsequent foreshock; shear stress perturbations ($d\tau$) are relatively weak at distances greater than $\sim$10 radii from the previous foreshock (i.e. $10 \cdot R_0 \sim 10.9$ mm). This detracts from the possibility of a cascading-style foreshock sequence. Furthermore, since the tip of the slowly propagating slip front only grows in the direction away from the trailing edge (Figures 6.9(b) and (c)), we would expect foreshocks to occur in a more organized manner if the cascade model was correct; i.e., expecting that the breakdown shear stress ($\Delta\tau_b$) across the breakdown zone (X_c) would drive the first foreshock and the subsequent foreshocks would appear further ahead of the slowly propagating rupture tip. In contrast, spatio-temporal observations of foreshock sequences (Figure 7.6(a)) show that foreshocks appear both ahead and behind the propagating slow rupture tip after the first foreshock was recorded. This observation is consistent with our numerical model, specifically the manner in which asperities enter a full sliding regime (Figure 7.4(a)). The ingress of slip into the locked region of the numerical model promotes the *preslip* model, and also demonstrates that stress shielding [98] is likely a contributing factor to the manner in which foreshock sequences are realized.

The evolution of the foreshock sequences impetus (or not) on how they impact the main shock are due to a variety of factors: the static (Coulomb) stress transfer from a foreshock (i.e. stress drop and source radius-dependent [172]), diffusional propagation of foreshock after-slip [5], the ability of small asperities to suppress slip (i.e. increased resistance to rupture [98]) and stiffness and density of asperities in the transitional 'crack-tip' region. These represent multiple mechanisms that may be driving the breakdown of shear stress (i.e. increase of slip) over the 'crack-tip' region. While observations in nature may promote one model relative to another, the reality is that numerous factors such as those mentioned above are likely to be fault-dependent and may occur concurrently. In the laboratory we are beginning to observe foreshock sequences and are able to discuss their relationship to the main shock – these mechanisms can be examined in a controlled environment.

Chapter 9

Conclusions

New development in sensors and data processing techniques have led to more refined observations of precursory phenomena leading up to earthquakes on natural faults. The previously developed phenomenological models successfully developed in the past to estimate seismic hazard are ill-equipped to accommodate some of the newer field observations. Preparatory seismicity (e.g., foreshocks, migrating swarm-like foreshocks, etc.) emitted from the boundary of a growing nucleation zone is becoming more frequently observed due to improved instrumentation of major intraplate earthquakes. We present findings from the laboratory that display isolate foreshocks with similar acoustic and spatio-temporal signatures as those observed in nature.

A mature fault was created by sliding two bodies of polymethyl methacrylate (PMMA) past each other under normal load in a direct shear configuration. The fault under normal force F_n and sheared until failure. Prior to failure, slow slip accumulated non-uniformly along the fault as measured by an array of slip sensors. These sensors captured the growth of a nucleation front (slow shear rupture) into a relatively locked region of the interface. As the normal force F_n was increased so did the ability of the fault to store shear strain due to increased shear stiffness of the interface. Shear stiffness of the interfaces was examined in the context of resistive patches of contacts (asperities) formed along the fault in a contact mechanics framework.

The rough-rough interaction of the two surfaces was characterized using contact mechanics. Local strength heterogeneities (asperities) formed were the rough-rough surfaces met. Location, size and normal stress at these contacting points were measured using a pressure sensitive film throughout the fault. At all normal load-levels, the fault displayed a region of densely distributed asperities. This region relatively 'locked' with respect to other sections of the fault – it resisted the ingress of the slowly propagating shear rupture due a stiffness gradient. At higher normal loads F_n, more asperities were measured in this region and higher amounts of shear strain accumulated along the fault. Acoustic emission sensors recorded high-frequency stress waves emitted from this relatively 'locked' section in the moments before gross fault rupture. The emission from the *seismogenic* region showed similar spatio-temporal and seismic signatures as foreshocks before a main shock. Foreshocks were the isolated, rapid failure of asperities within the breakdown region of the nucleation front – a feature that was confirmed using asperity photometry (i.e. direct observation). Within a sequence of foreshocks leading up to failure, we noticed an increase in magnitude and clustering from an individual foreshock as we increased the normal force F_n.

To develop an understanding of the relationship between F_n and the resistance of the fault to

the slow shear rupture front, a quasi-static finite element (FE) model was developed. The model used distributions of asperities directly measured from the pressure sensitive film in a small section of the interface where foreshocks coalesced; i.e. the 'locked' section of the fault, specifically the region where the slowly propagating slip front met the more dense distribution of asperities (x = 182.5 to 257.5 mm). Physics from the numerical model followed the qualitative observations made using photometry of asperities along the interface, which visualized asperities in the 'locked' region – larger asperities remained stuck throughout the loading cycle and the light transmitted through individual asperities constricted throughout the loading cycle. The numerical partial slip asperity quantified the potential energy stored by the asperity increased relative to the normal pressure p. Multiple asperities were modeled along the interface using a quasi-static analysis. Progression of slip into the asperity field was inhibited as the normal confining force F_n was increased. The computational model provided an explanation as to why an increased confining force F_n would result from both an increased resistance to slow rupture as well as an increased potential for larger foreshocks within the resistive, relatively 'locked' section of a fault. In all, the numerical and experimental results imply the validity of Ohnaka's slip-weakening nucleation model.

Appendix A

Experimental facilities details

This page is intentionally left blank.

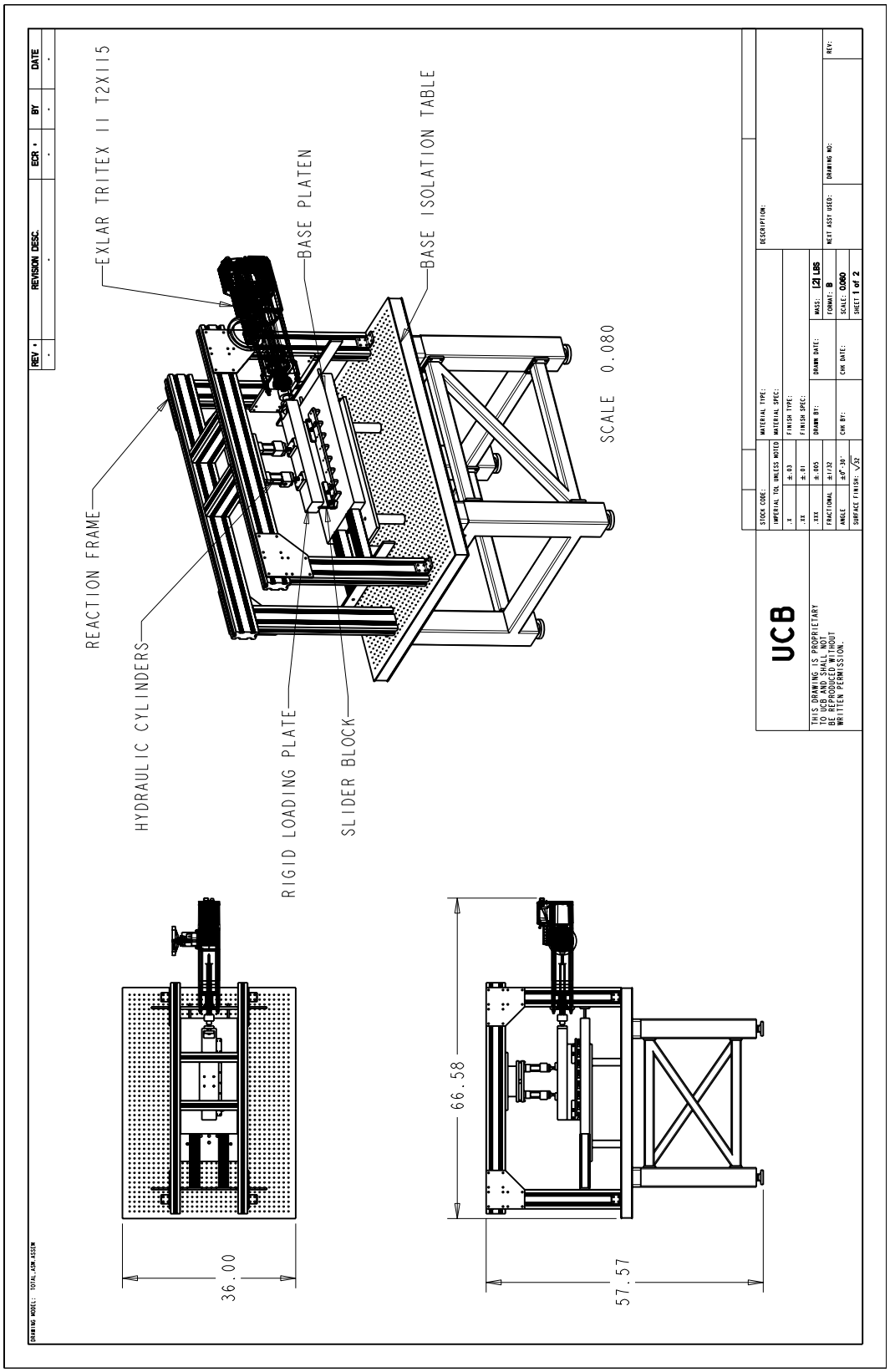
EXLAR TRITEX II T2X115
BASE PLATEN
BASE ISOLATION TABLE
REACTION FRAME
HYDRAULIC CYLINDERS
RIGID LOADING PLATE
SLIDER BLOCK
SCALE 0.080
36.00
66.58
57.57
UCB

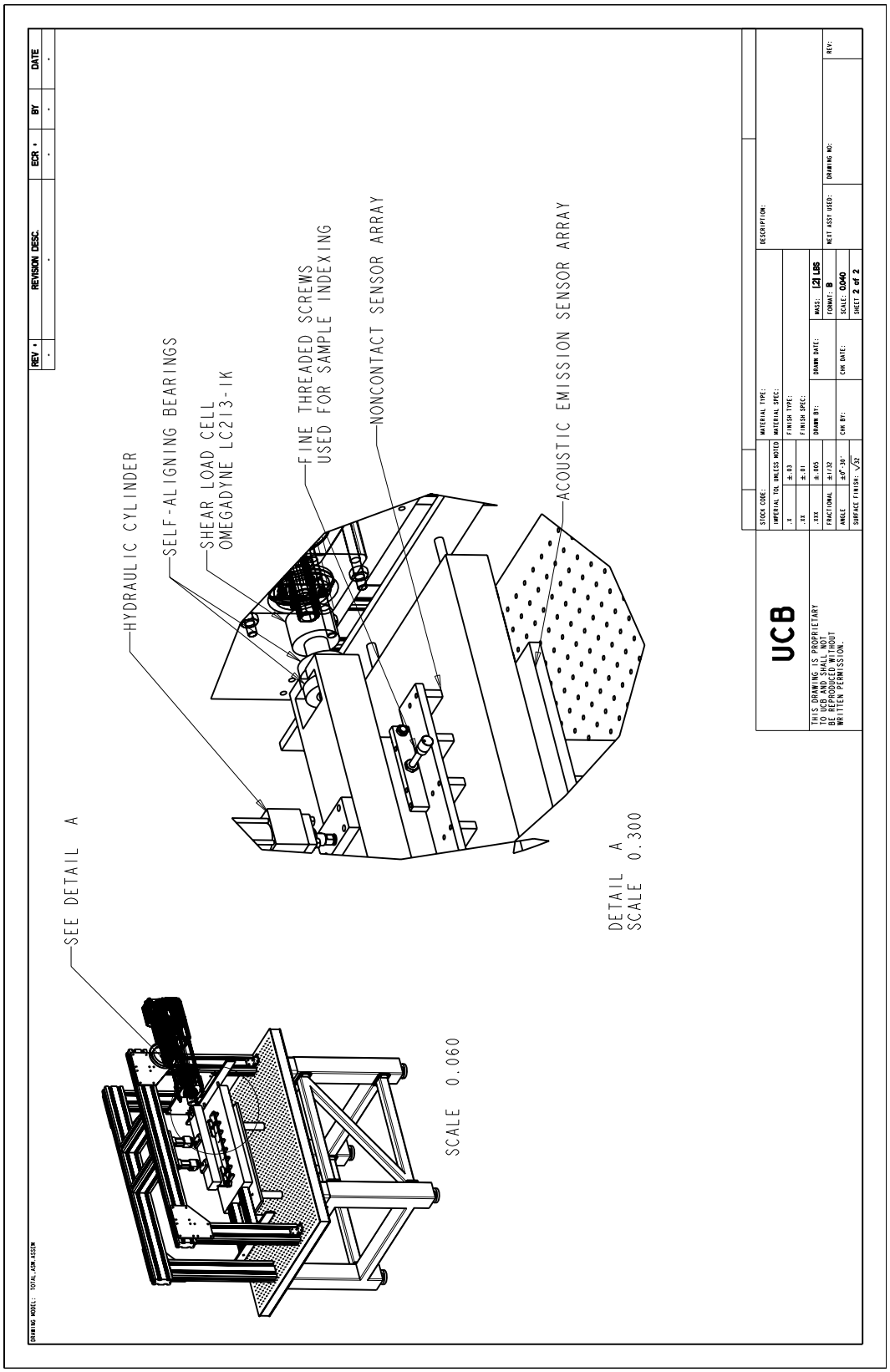
HYDRAULIC CYLINDER
SELF-ALIGNING BEARINGS
SHEAR LOAD CELL
OMEGADYNE LC213-1K
FINE THREADED SCREWS
USED FOR SAMPLE INDEXING
NONCONTACT SENSOR ARRAY
ACOUSTIC EMISSION SENSOR ARRAY
SEE DETAIL A
SCALE 0.060
DETAIL A
SCALE 0.300
UCB
THIS DRAWING IS PROPRIETARY TO UCB AND SHALL NOT BE REPRODUCED WITHOUT WRITTEN PERMISSION.
DRAWING MODEL: TOTAL_ASM.ASSEM
REV
REVISION DESC.
ECR #
BY
DATE
DESCRIPTION:
STOCK CODE:
MATERIAL TYPE:
MATERIAL SPEC:
FINISH TYPE:
FINISH SPEC:
IMPERIAL TOL UNLESS NOTED
.X ± .03
.XX ± .01
.XXX ± .005
FRACTIONAL ± 1/32
ANGLE ± 0° 30'
SURFACE FINISH: √32
DRAWN BY:
CHK BY:
DRAWN DATE:
CHK DATE:
MASS: [2] LBS
FORMAT: B
SCALE: 0040
SHEET 2 of 2
NEXT ASSY USED:
DRAWING NO:
REV:

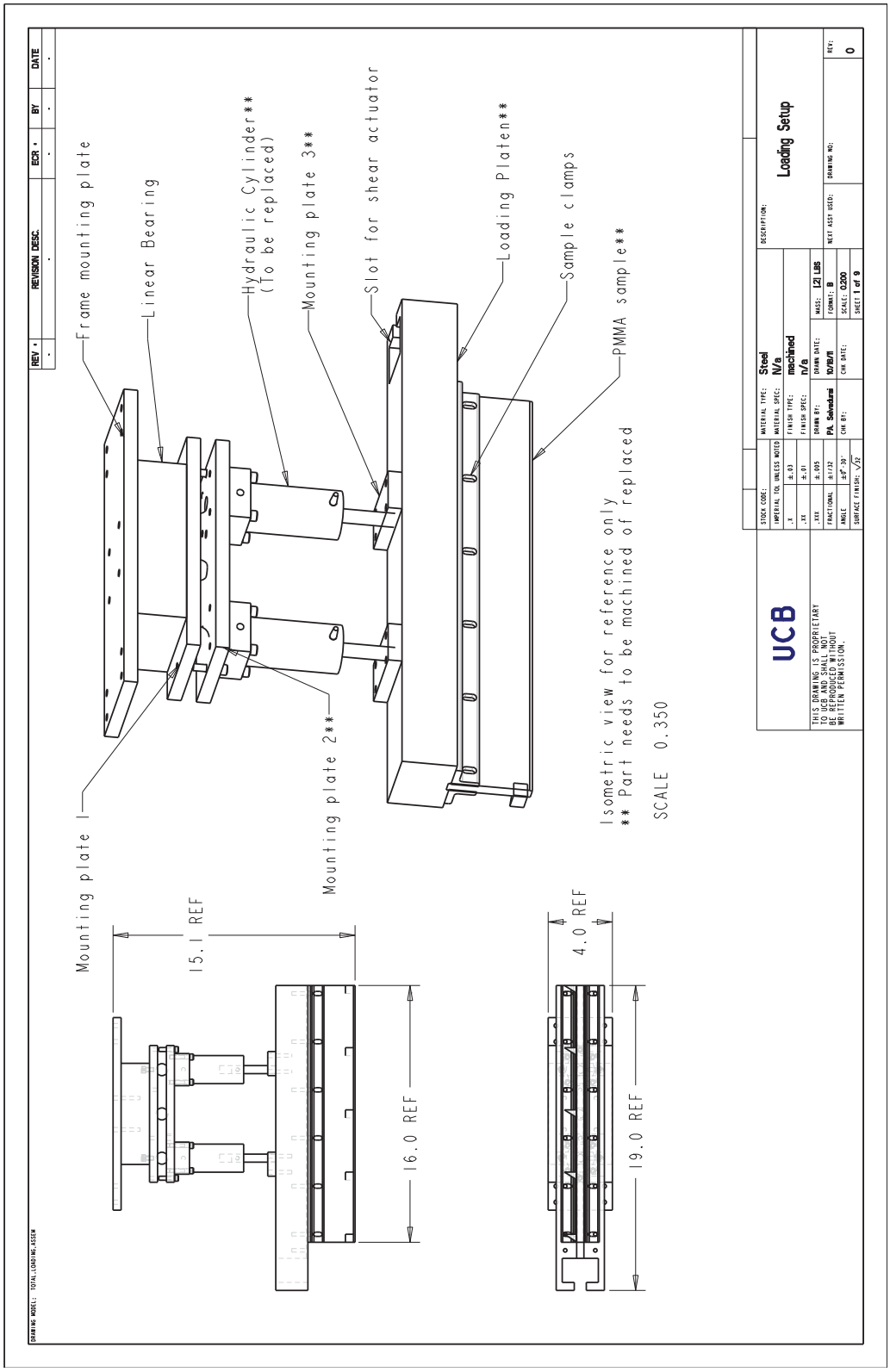
Frame mounting plate
Linear Bearing
Hydraulic Cylinder**
(To be replaced)
Mounting plate 3**
Slot for shear actuator
Loading Platen**
Sample clamps
PMMA sample**
Mounting plate 1
Mounting plate 2**
Isometric view for reference only
** Part needs to be machined of replaced
SCALE 0.350
15.1 REF
16.0 REF
4.0 REF
19.0 REF
Loading Setup
UCB
Steel
N/a
machined
n/a
[2] LBS
B
0.200
1 of 9
0

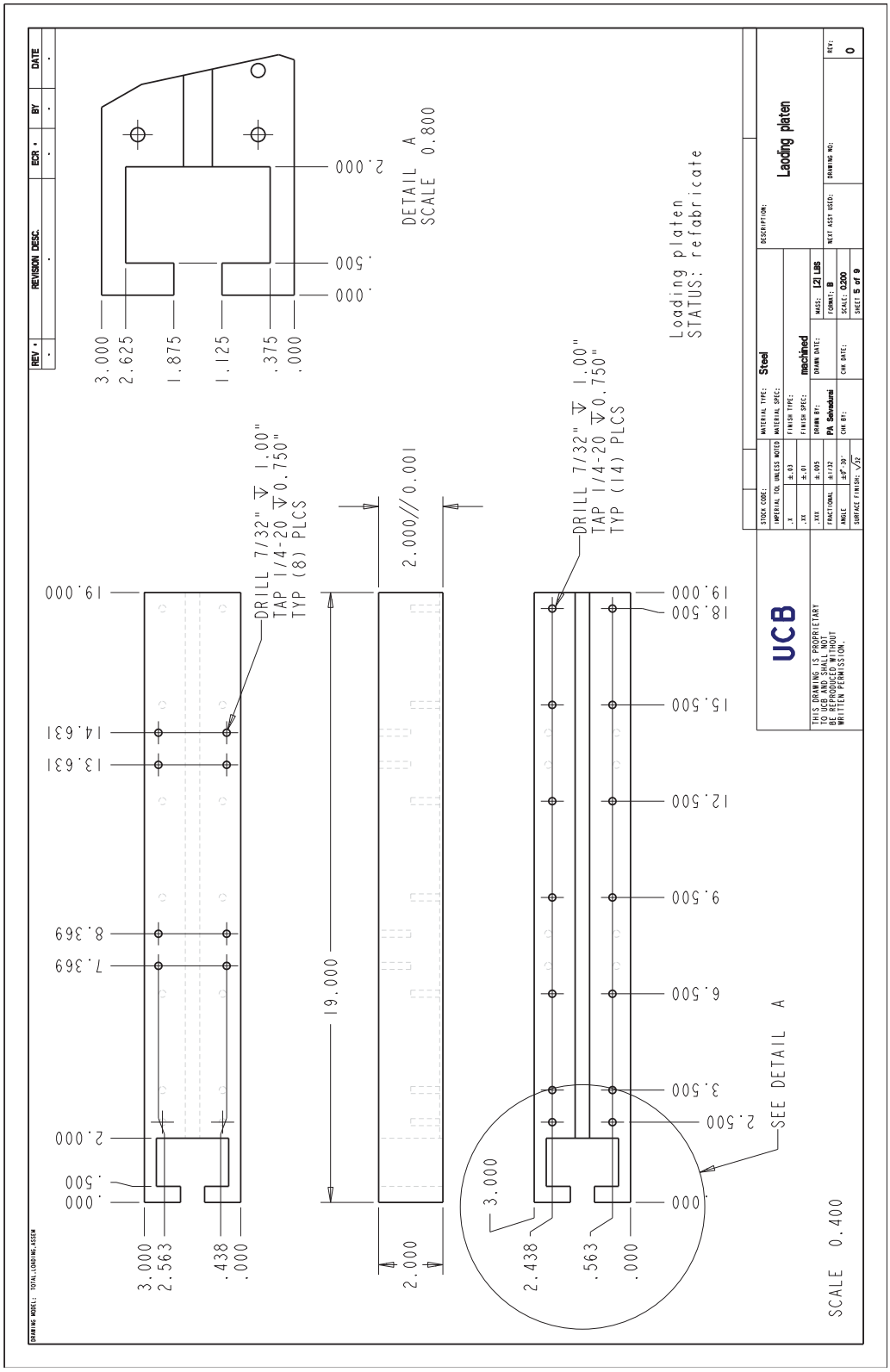
Loading platen
STATUS: refabricate
DETAIL A
SCALE 0.800
3.000
2.625
1.875
1.125
.375
.000
2.000
.500
.000
DRILL 7/32" ⊽ 1.00"
TAP 1/4-20 ⊽0.750"
TYP (8) PLCS
19.000
14.631
13.631
8.369
7.369
2.000
.500
.000
3.000
2.563
.438
.000
2.000//0.001
19.000
2.000
DRILL 7/32" ⊽ 1.00"
TAP 1/4-20 ⊽0.750"
TYP (14) PLCS
19.000
18.500
15.500
12.500
9.500
6.500
3.500
2.500
.000
SEE DETAIL A
3.000
2.438
.563
.000
SCALE 0.400
REV
REVISION DESC.
ECR
BY
DATE
UCB
THIS DRAWING IS PROPRIETARY TO UCB AND SHALL NOT BE REPRODUCED WITHOUT WRITTEN PERMISSION.
STOCK CODE:
IMPERIAL TOL UNLESS NOTED
.X ±.03
.XX ±.01
.XXX ±.005
FRACTIONAL ±1/32
ANGLE ±0°30'
SURFACE FINISH: √32
MATERIAL TYPE: Steel
MATERIAL SPEC:
FINISH TYPE: machined
FINISH SPEC:
DRAWN BY: PA Sahebani
CHK BY:
DRAWN DATE:
CHK DATE:
DESCRIPTION: Laoding platen
MASS: 12 LBS
FORMAT: B
SCALE: 0.200
SHEET 5 of 9
NEXT ASSY USED:
DRAWING NO:
REV: 0
DRAWING MODEL: TOTAL.LOADING.ASSEM

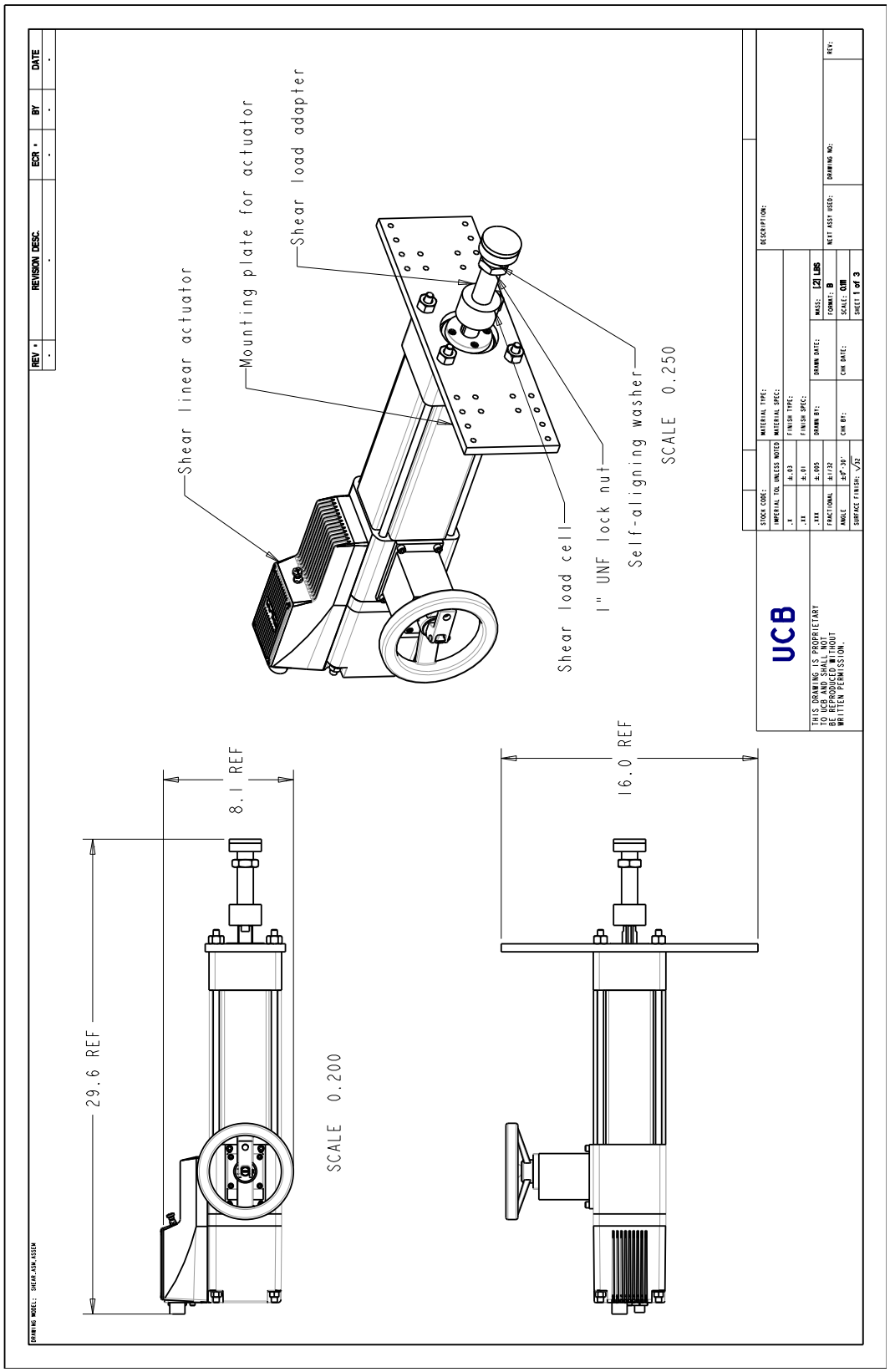
Shear linear actuator
Mounting plate for actuator
Shear load adapter
Shear load cell
1" UNF lock nut
Self-aligning washer
SCALE 0.250
8.1 REF
29.6 REF
SCALE 0.200
16.0 REF
UCB
THIS DRAWING IS PROPRIETARY TO UCB AND SHALL NOT BE REPRODUCED WITHOUT WRITTEN PERMISSION.
REV
REVISION DESC.
ECR #
BY
DATE
DESCRIPTION:
STOCK CODE:
MATERIAL TYPE:
MATERIAL SPEC:
FINISH TYPE:
FINISH SPEC:
DRAWN BY:
DRAWN DATE:
CHK BY:
CHK DATE:
MASS: [2] LBS
FORMAT: B
SCALE: CUR
SHEET 1 of 3
NEXT ASSY USED:
DRAWING NO:
REV:
DRAWING MODEL: SHEAR_ASM_ASSEM

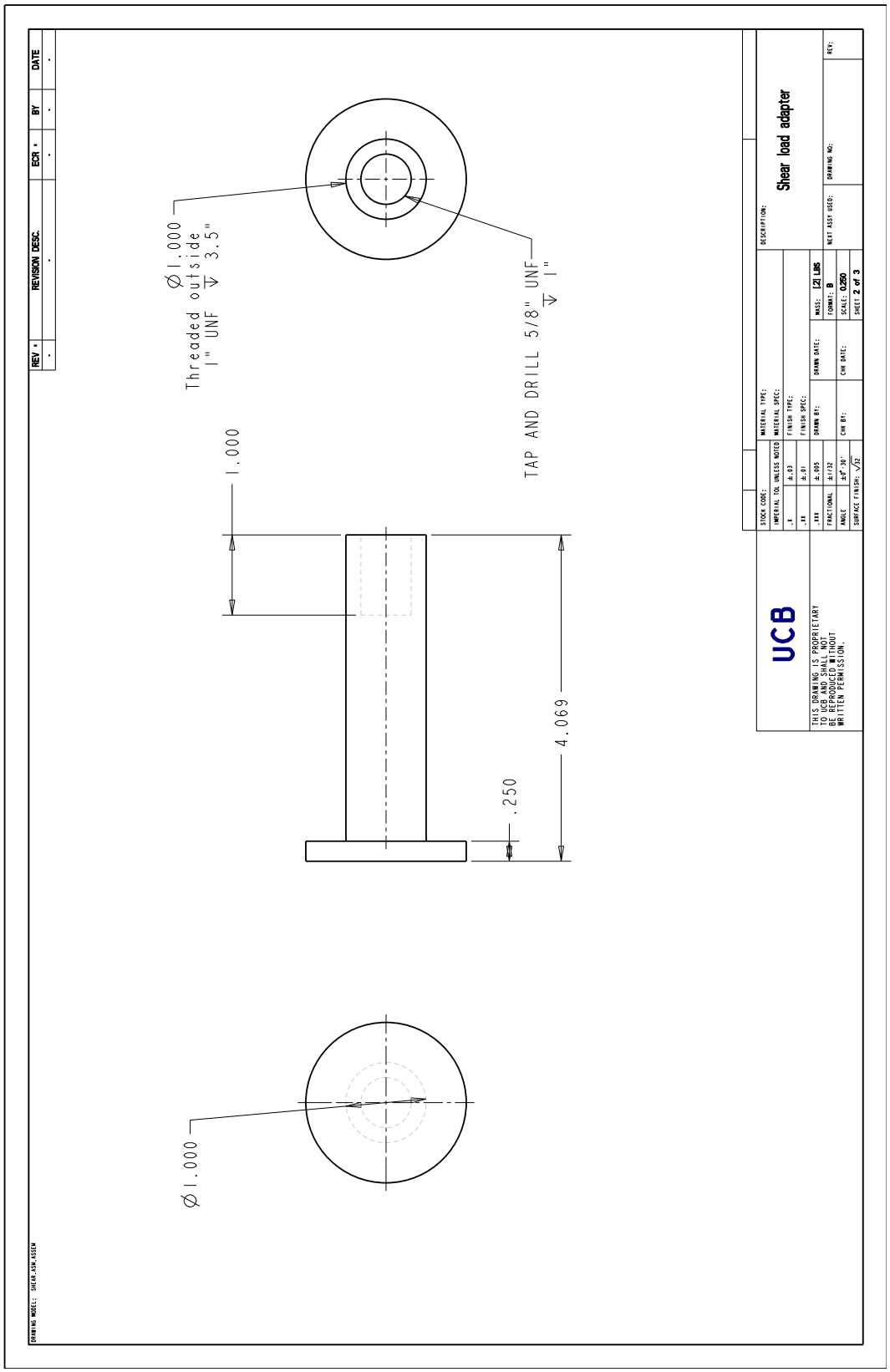
REV
REVISION DESC.
ECR #
BY
DATE
Ø1.000
Threaded outside
1" UNF ↧ 3.5"
TAP AND DRILL 5/8" UNF
↧ 1"
1.000
.250
4.069
Ø1.000
UCB
Shear load adapter
DESCRIPTION:
STOCK CODE:
MATERIAL TYPE:
MATERIAL SPEC:
FINISH TYPE:
FINISH SPEC:
IMPERIAL TOL UNLESS NOTED
.X ±.03
.XX ±.01
.XXX ±.005
FRACTIONAL ±1/32
ANGLE ±0° 30'
SURFACE FINISH: √32
DRAWN BY:
CHK BY:
DRAWN DATE:
CHK DATE:
MASS: 12] LBS
FORMAT: B
SCALE: 0.250
SHEET 2 of 3
NEXT ASSY USED:
DRAWING NO:
REV:
THIS DRAWING IS PROPRIETARY TO UCB AND SHALL NOT BE REPRODUCED WITHOUT WRITTEN PERMISSION.
DRAWING MODEL: SHEAR_ASM_ASSEM

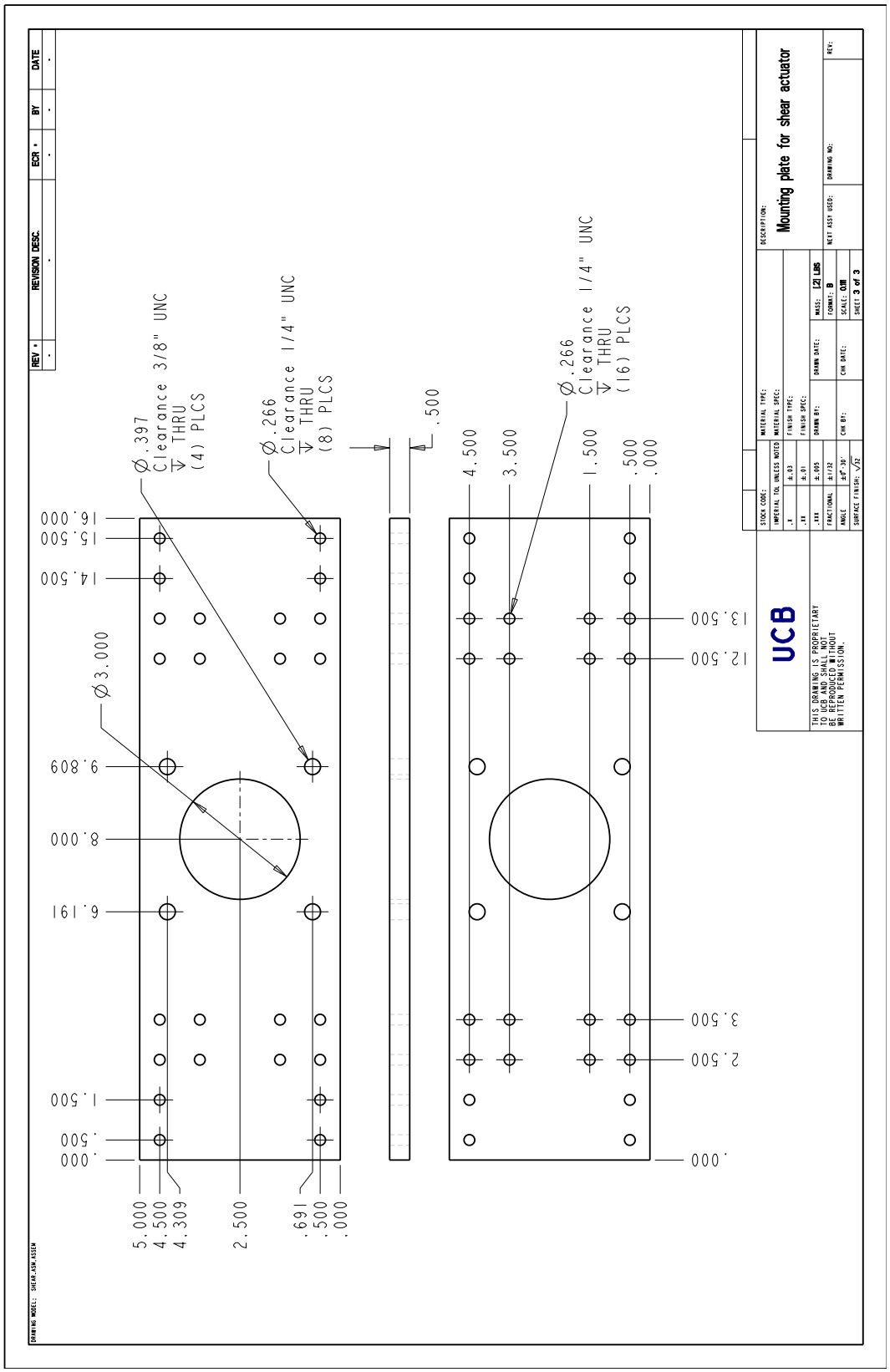
Mounting plate for shear actuator
UCB
Ø.397 Clearance 3/8" UNC ⊽ THRU (4) PLCS
Ø.266 Clearance 1/4" UNC ⊽ THRU (8) PLCS
Ø.266 Clearance 1/4" UNC ⊽ THRU (16) PLCS
Ø3.000
.500
4.500
3.500
1.500
.500
.000
16.000
15.500
14.500
9.809
8.000
6.191
1.500
.500
.000
13.500
12.500
3.500
2.500
.000
5.000
4.500
4.309
2.500
.691
.500
.000

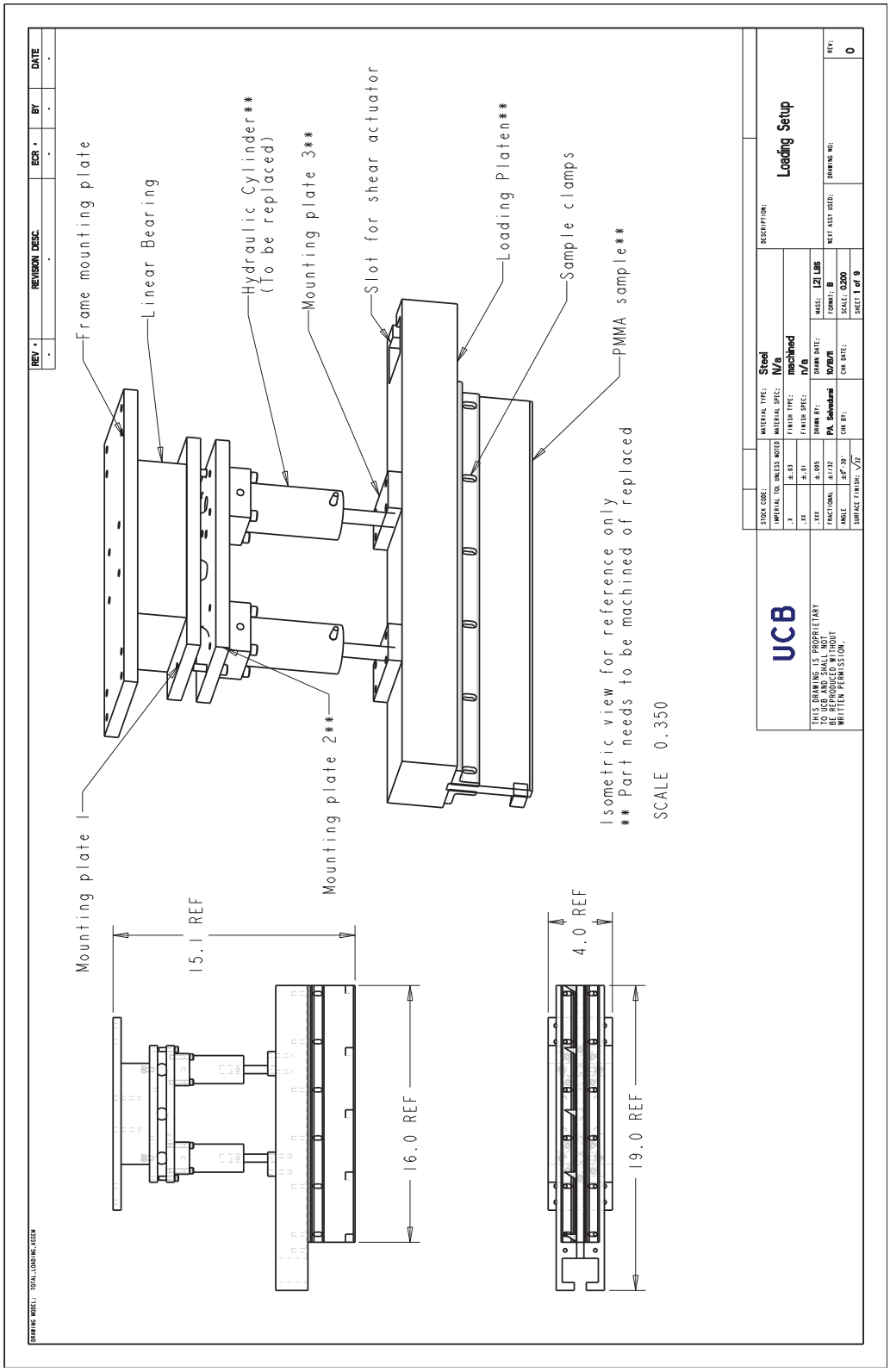
Frame mounting plate
Linear Bearing
Hydraulic Cylinder**
(To be replaced)
Mounting plate 3**
Slot for shear actuator
Loading Platen**
Sample clamps
PMMA sample**
Mounting plate 1
Mounting plate 2**
Isometric view for reference only
** Part needs to be machined of replaced
SCALE 0.350
15.1 REF
16.0 REF
4.0 REF
19.0 REF
REV
REVISION DESC.
ECR
BY
DATE
Loading Setup
UCB
Steel
N/a
machined
n/a
DRAWING MODEL: TOTAL_LOADING_ASSEM

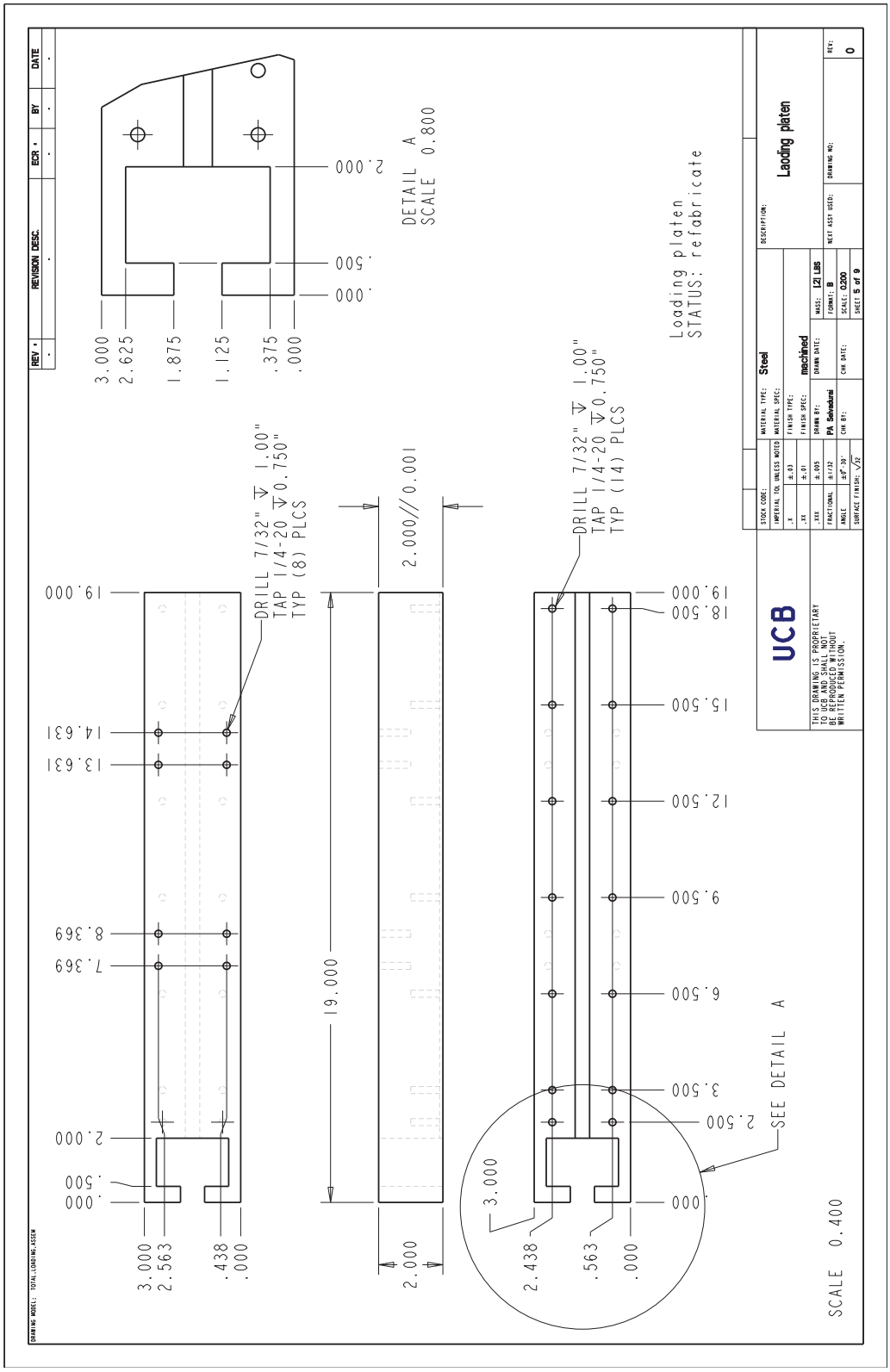
Loading platen
STATUS: refabricate
DETAIL A
SCALE 0.800
3.000
2.625
1.875
1.125
.375
.000
2.000
.500
.000
DRILL 7/32" ⌀ 1.00"
TAP 1/4-20 ↧0.750"
TYP (8) PLCS
19.000
2.000// 0.001
DRILL 7/32" ⌀ 1.00"
TAP 1/4-20 ↧0.750"
TYP (14) PLCS
19.000
18.500
15.500
12.500
9.500
6.500
3.500
2.500
.000
14.631
13.631
8.369
7.369
2.000
.500
.000
3.000
2.563
.438
.000
SEE DETAIL A
3.000
2.438
.563
.000
SCALE 0.400
UCB
THIS DRAWING IS PROPRIETARY TO UCB AND SHALL NOT BE REPRODUCED WITHOUT WRITTEN PERMISSION.
STOCK CODE:
IMPERIAL TOL UNLESS NOTED
.X ±.03
.XX ±.01
.XXX ±.005
FRACTIONAL ±1/32
ANGLE ±0°-30'
SURFACE FINISH: √32
MATERIAL TYPE: Steel
MATERIAL SPEC:
FINISH TYPE: machined
FINISH SPEC:
DRAWN BY: PA Sahebani
CHK BY:
DRAWN DATE:
CHK DATE:
DESCRIPTION: Laoding platen
MASS: 12 LBS
FORMAT: B
SCALE: 0.200
SHEET 5 of 9
NEXT ASSY USED:
DRAWING NO:
REV: 0
REV • REVISION DESC. ECR • BY DATE
DRAWING MODEL: TOTAL.LOADING.ASSEM

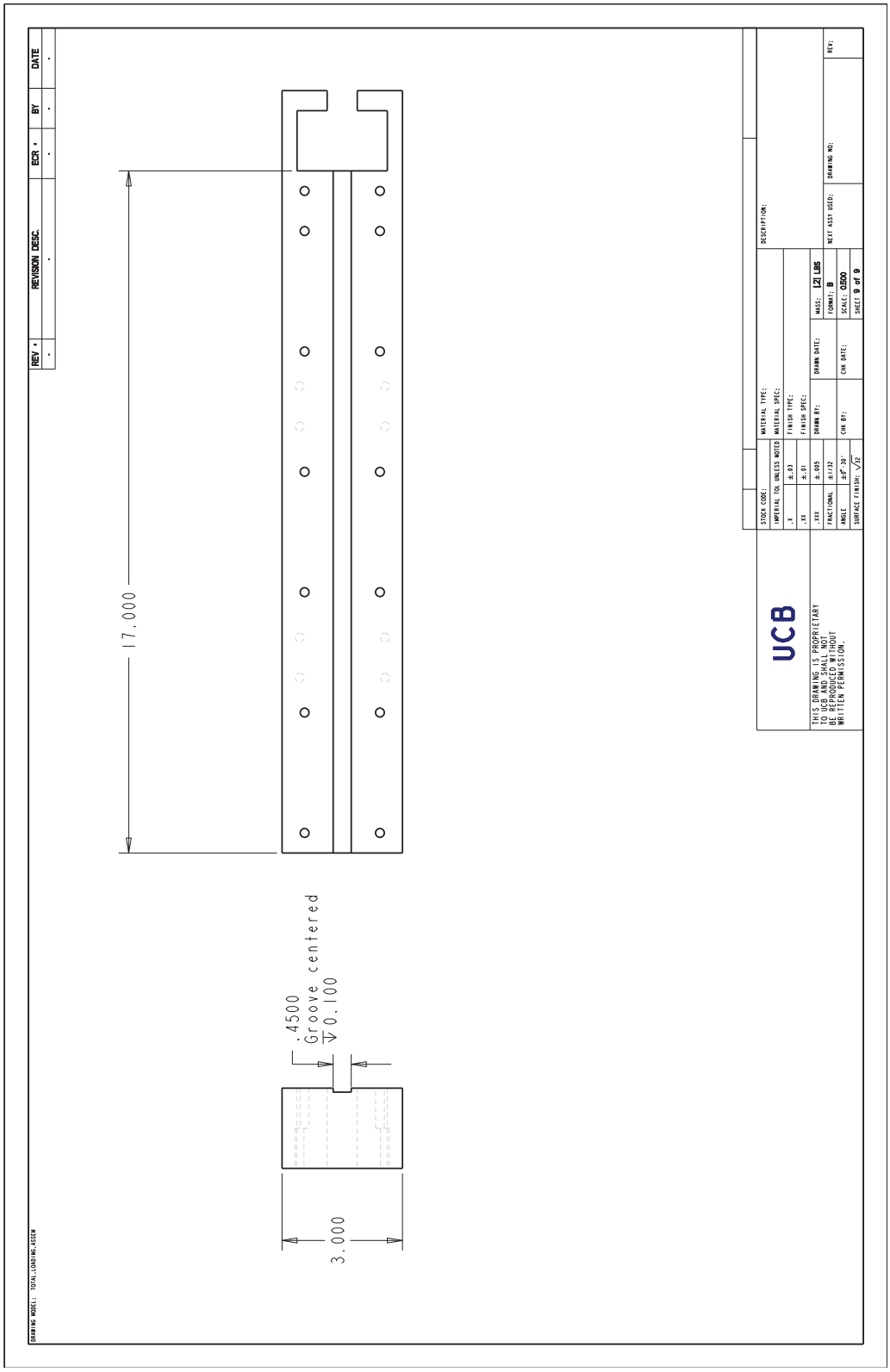
17.000
.4500
Groove centered
0.100
3.000
UCB
THIS DRAWING IS PROPRIETARY TO UCB AND SHALL NOT BE REPRODUCED WITHOUT WRITTEN PERMISSION.
REV
REVISION DESC.
ECR #
BY
DATE
DRAWING MODEL: TOTAL_LOADING_ASSEM
STOCK CODE:
IMPERIAL TOL UNLESS NOTED
.X ±.03
.XX ±.01
.XXX ±.005
FRACTIONAL ±1/32
ANGLE ±0°30'
SURFACE FINISH: √32
MATERIAL TYPE:
MATERIAL SPEC:
FINISH TYPE:
FINISH SPEC:
DRAWN BY:
CHK BY:
DRAWN DATE:
CHK DATE:
MASS: 12 LBS
FORMAT: B
SCALE: 0.500
SHEET 9 of 9
DESCRIPTION:
NEXT ASSY USED:
DRAWING NO:
REV:

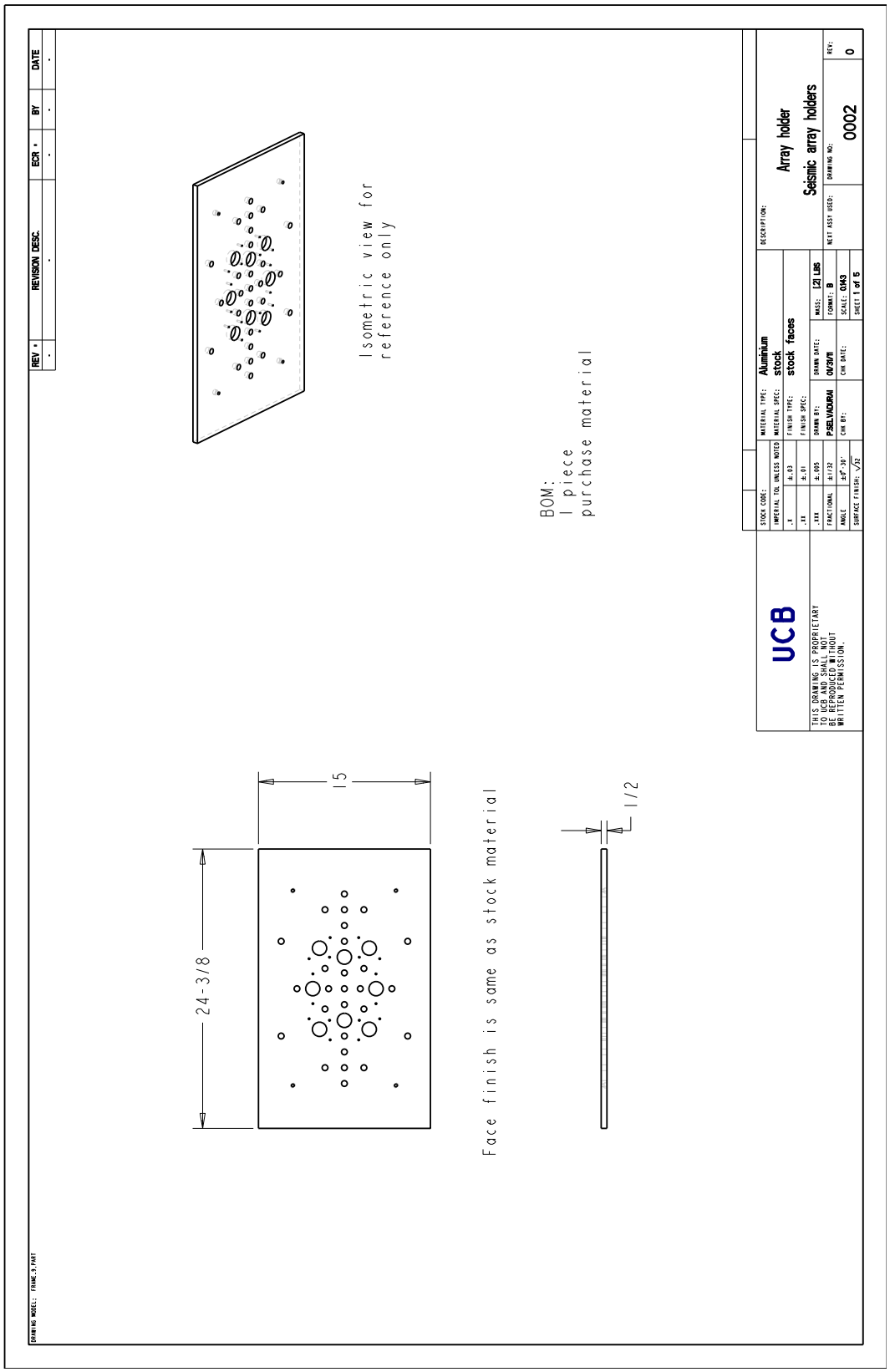
REV
REVISION DESC.
ECR #
BY
DATE
Isometric view for reference only
BOM:
1 piece
purchase material
24-3/8
15
Face finish is same as stock material
1/2
UCB
Aluminium
stock
stock faces
Array holder
Seismic array holders
0002
0
SHEET 1 of 5

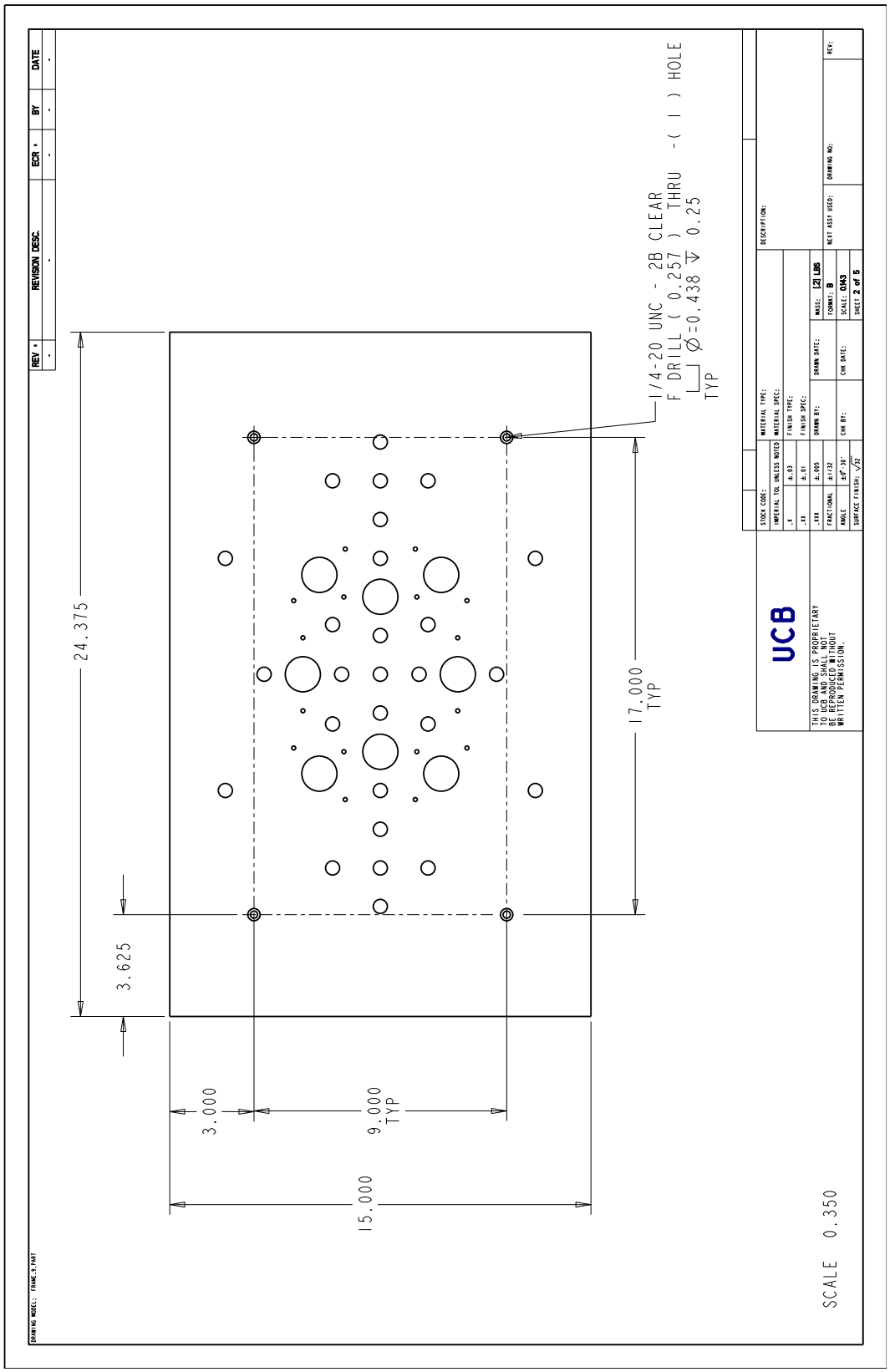
1/4-20 UNC - 2B CLEAR
F DRILL (0.257) THRU -(I I) HOLE
⌴ Ø=0.438 ↧ 0.25
TYP
24.375
3.625
17.000
TYP
3.000
9.000
TYP
15.000
SCALE 0.350
UCB
REV
REVISION DESC.
ECR
BY
DATE
DESCRIPTION:
THIS DRAWING IS PROPRIETARY TO UCB AND SHALL NOT BE REPRODUCED WITHOUT WRITTEN PERMISSION.
MASS: [2] LBS
FORMAT: B
SCALE: 0X3
SHEET 2 of 5
NEXT ASSY USED:
DRAWING NO:
REV:

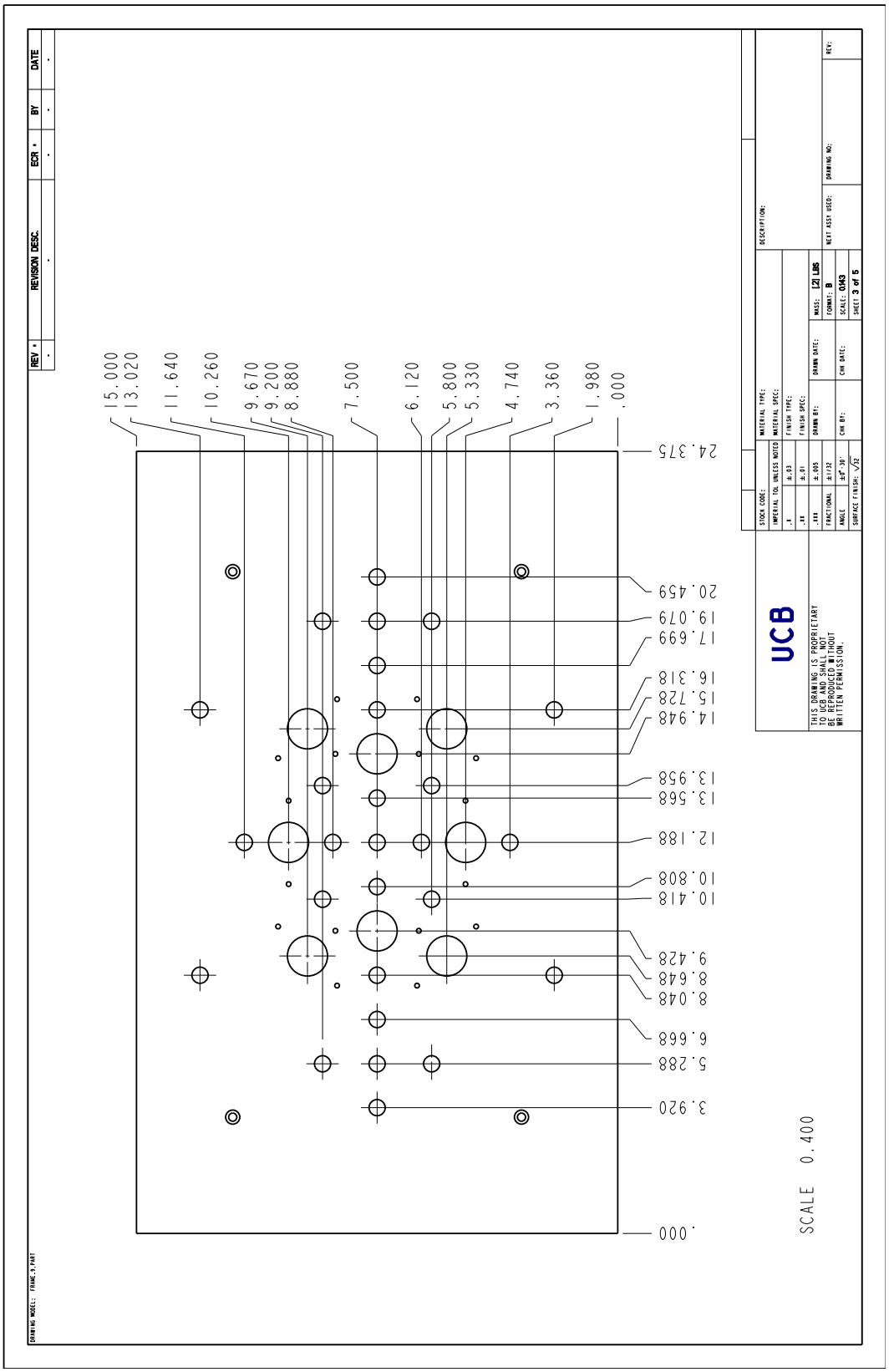
REV *
REVISION DESC.
ECR *
BY
DATE
15.000
13.020
11.640
10.260
9.670
9.200
8.880
7.500
6.120
5.800
5.330
4.740
3.360
1.980
.000
24.375
20.459
19.079
17.699
16.318
15.728
14.948
13.958
13.568
12.188
10.808
10.418
9.428
8.648
8.048
6.668
5.288
3.920
.000
SCALE 0.400
UCB
THIS DRAWING IS PROPRIETARY TO UCB AND SHALL NOT BE REPRODUCED WITHOUT WRITTEN PERMISSION.
STOCK CODE:
IMPERIAL TOL UNLESS NOTED
MATERIAL TYPE:
MATERIAL SPEC:
FINISH TYPE:
FINISH SPEC:
DRAWN BY:
CHK BY:
DRAWN DATE:
CHK DATE:
MASS: [2] LBS
FORMAT: B
SCALE: 0X3
SHEET 3 of 5
DESCRIPTION:
NEXT ASSY USED:
DRAWING NO:
REV:
DRAWING MODEL: FRAME_9.PART

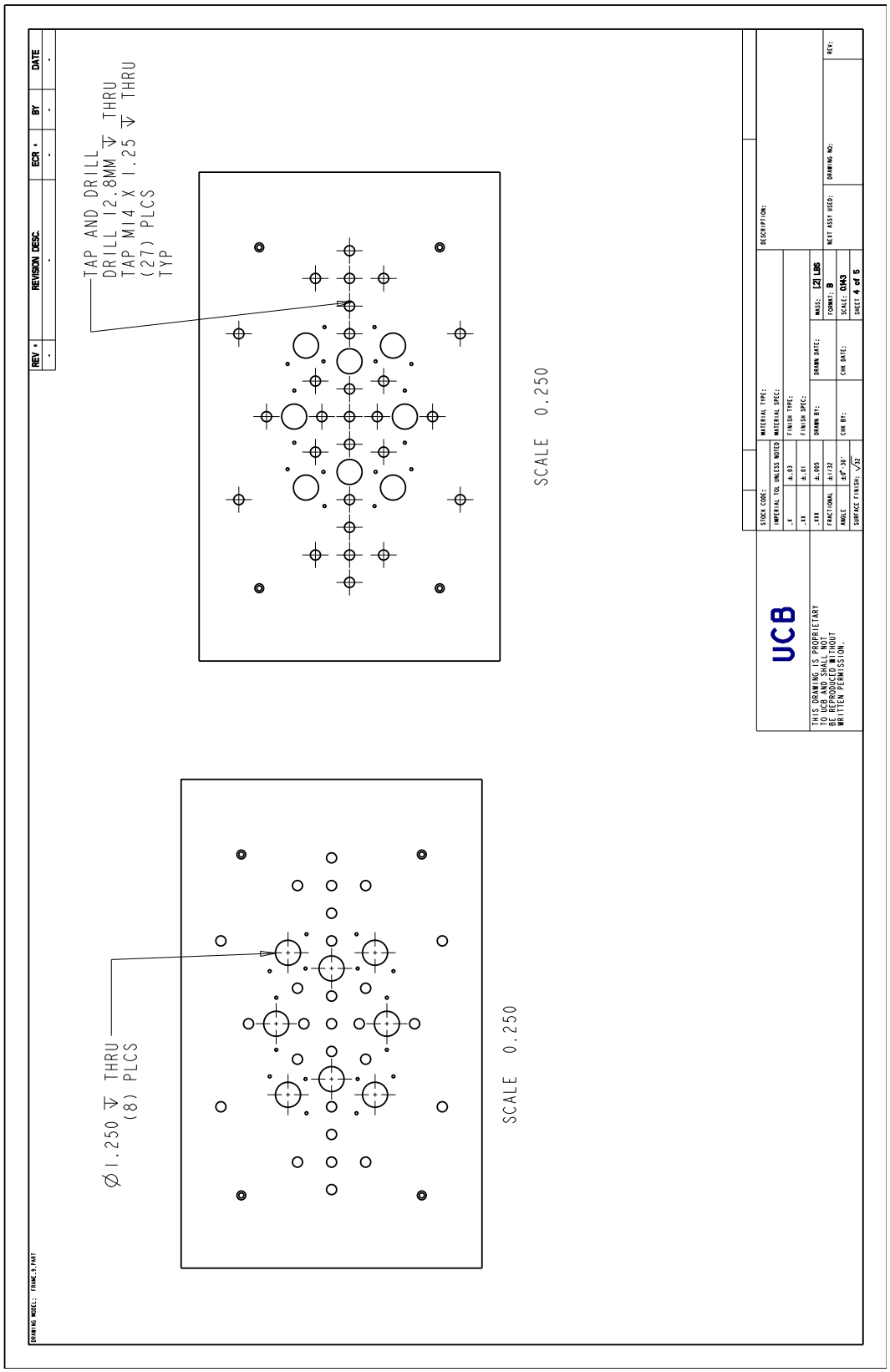
TAP AND DRILL
DRILL 12.8MM ⌀ THRU
TAP M14 X 1.25 ⌀ THRU
(27) PLCS
TYP
SCALE 0.250
Ø1.250 ⌀ THRU
(8) PLCS
SCALE 0.250
REV
REVISION DESC.
ECR #
BY
DATE
DRAWING MODEL: FRAME_9.PART
UCB
THIS DRAWING IS PROPRIETARY TO UCB AND SHALL NOT BE REPRODUCED WITHOUT WRITTEN PERMISSION.
STOCK CODE:
MATERIAL TYPE:
IMPERIAL TOL UNLESS NOTED
MATERIAL SPEC:
.X ±.03
FINISH TYPE:
.XX ±.01
FINISH SPEC:
.XXX ±.005
DRAWN BY:
DRAWN DATE:
MASS: [2] LBS
FRACTIONAL ±1/32
CHK BY:
CHK DATE:
FORMAT: B
ANGLE ±0° 30'
SCALE: 0343
SURFACE FINISH: √32
SHEET 4 of 5
DESCRIPTION:
NEXT ASSY USED:
DRAWING NO:
REV:

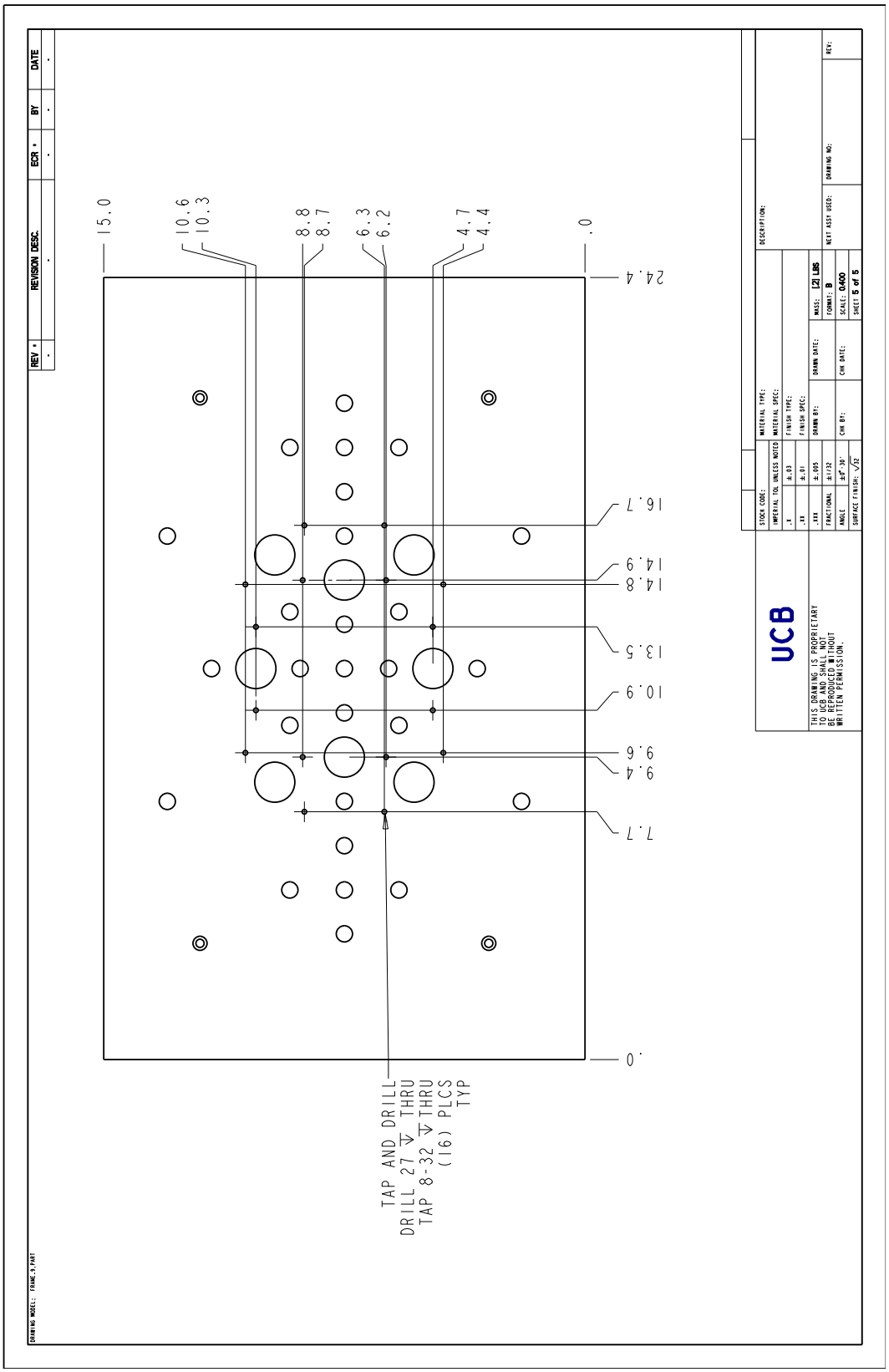
15.0
10.6
10.3
8.8
8.7
6.3
6.2
4.7
4.4
.0
24.4
16.7
14.9
14.8
13.5
10.9
9.6
9.4
7.7
.0
TAP AND DRILL
DRILL 27 ⩛ THRU
TAP 8-32 ⩛ THRU
(16) PLCS
TYP
REV #
REVISION DESC.
ECR #
BY
DATE
UCB
THIS DRAWING IS PROPRIETARY TO UCB AND SHALL NOT BE REPRODUCED WITHOUT WRITTEN PERMISSION.
STOCK CODE:
MATERIAL TYPE:
IMPERIAL TOL UNLESS NOTED
MATERIAL SPEC:
.X ±.03
FINISH TYPE:
.XX ±.01
FINISH SPEC:
.XXX ±.005
DRAWN BY:
DRAWN DATE:
FRACTIONAL ±1/32
ANGLE ±0° 30'
CHK BY:
CHK DATE:
SURFACE FINISH: √32
MASS: [2] LBS
FORMAT: B
SCALE: 0.400
SHEET 5 of 5
DESCRIPTION:
NEXT ASSY USED:
DRAWING NO:
REV:
DRAWING MODEL: FRAME_9.PART

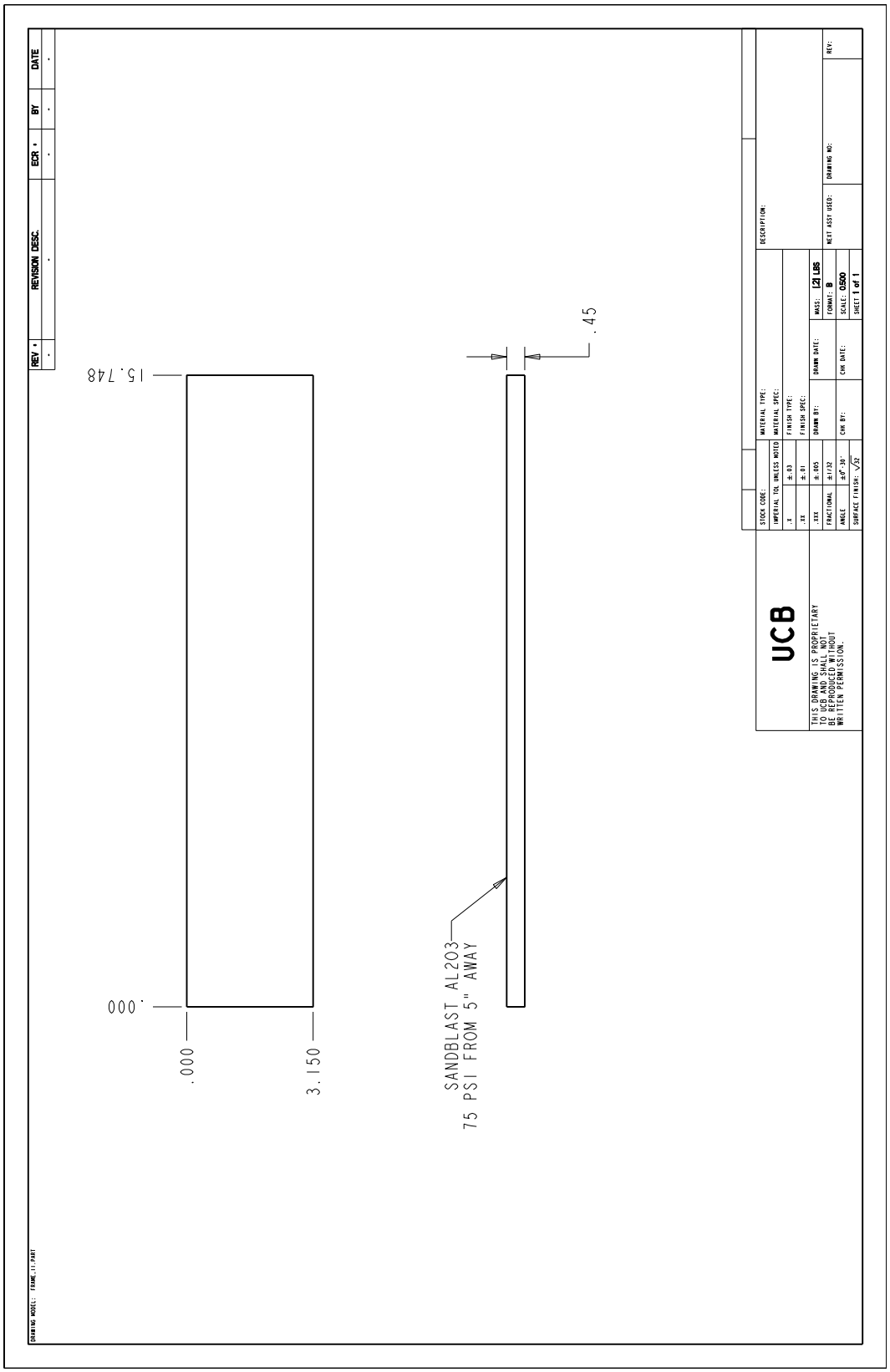
REV
REVISION DESC.
ECR #
BY
DATE
15.748
.000
.000
3.150
.45
SANDBLAST AL203
75 PSI FROM 5" AWAY
UCB
STOCK CODE:
MATERIAL TYPE:
IMPERIAL TOL UNLESS NOTED
MATERIAL SPEC:
FINISH TYPE:
FINISH SPEC:
DRAWN BY:
DRAWN DATE:
CHK BY:
CHK DATE:
MASS: 121 LBS
FORMAT: B
SCALE: 0500
SHEET 1 of 1
NEXT ASSY USED:
DRAWING NO:
REV:
DESCRIPTION:
THIS DRAWING IS PROPRIETARY TO UCB AND SHALL NOT BE REPRODUCED WITHOUT WRITTEN PERMISSION.

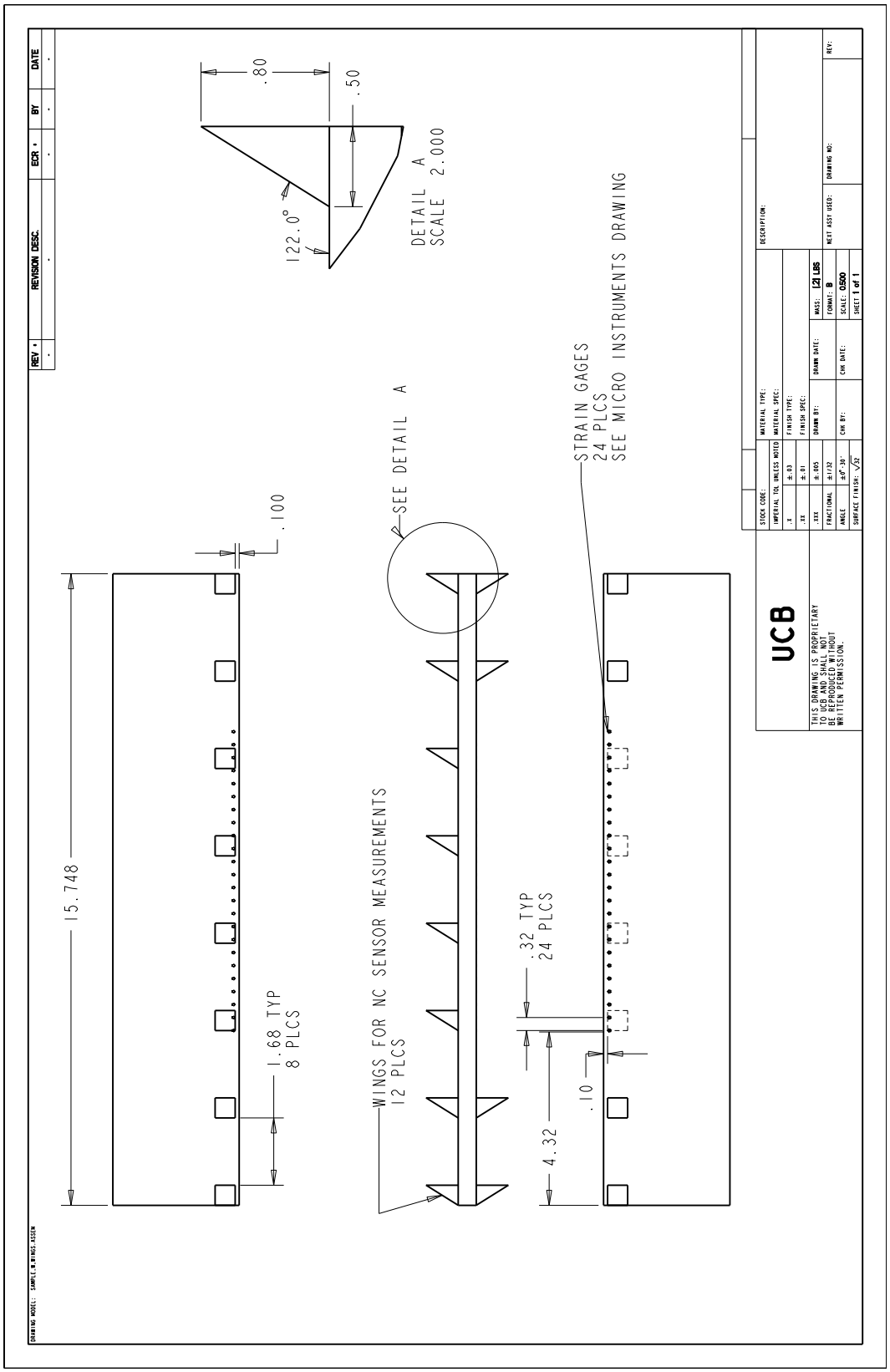
.80
.50
122.0°
DETAIL A
SCALE 2.000
.100
SEE DETAIL A
STRAIN GAGES
24 PLCS
SEE MICRO INSTRUMENTS DRAWING
15.748
1.68 TYP
8 PLCS
WINGS FOR NC SENSOR MEASUREMENTS
12 PLCS
.32 TYP
24 PLCS
4.32
.10
UCB
THIS DRAWING IS PROPRIETARY TO UCB AND SHALL NOT BE REPRODUCED WITHOUT WRITTEN PERMISSION.
REV
REVISION DESC.
ECR #
BY
DATE
DESCRIPTION:
STOCK CODE:
MATERIAL TYPE:
MATERIAL SPEC:
FINISH TYPE:
FINISH SPEC:
DRAWN BY:
DRAWN DATE:
CHK BY:
CHK DATE:
MASS: [2] LBS
FORMAT: B
SCALE: 0.500
SHEET 1 of 1
NEXT ASSY USED:
DRAWING NO:
REV:

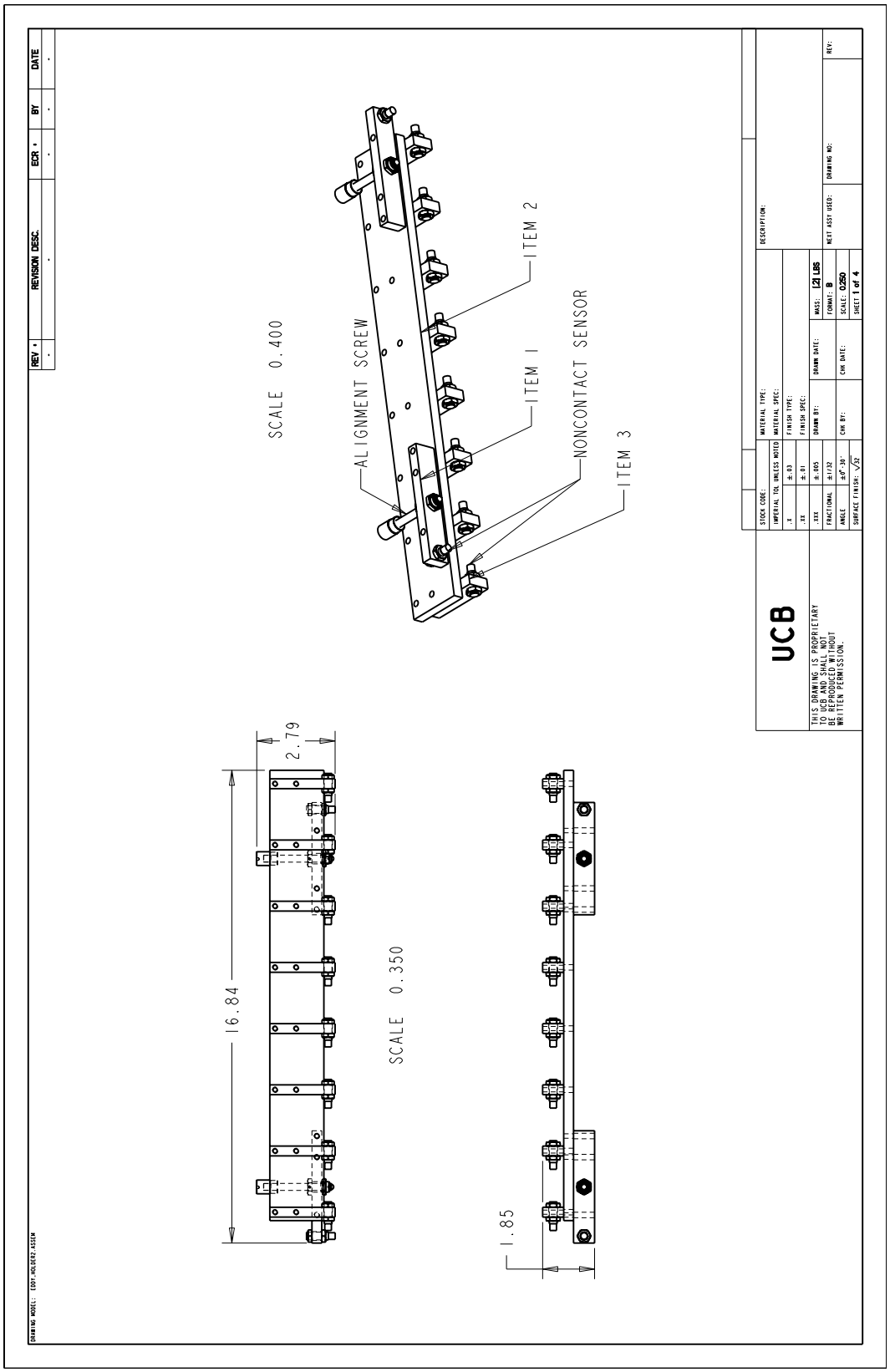
SCALE 0.400
ALIGNMENT SCREW
ITEM 2
ITEM 1
NONCONTACT SENSOR
ITEM 3
2.79
16.84
SCALE 0.350
1.85
UCB
REV
REVISION DESC.
ECR #
BY
DATE
DESCRIPTION:
STOCK CODE:
MATERIAL TYPE:
IMPERIAL TOL UNLESS NOTED
MATERIAL SPEC:
FINISH TYPE:
FINISH SPEC:
DRAWN BY:
DRAWN DATE:
CHK BY:
CHK DATE:
MASS: [2] LBS
FORMAT: B
SCALE: 0.250
SHEET 1 of 4
NEXT ASSY USED:
DRAWING NO:
REV:
THIS DRAWING IS PROPRIETARY TO UCB AND SHALL NOT BE REPRODUCED WITHOUT WRITTEN PERMISSION.

Appendix B

Pressure sensitive film algorithms

This page is intentionally left blank.

11/19/15 2:18 PM C:\...\I_CONVERT_TO_STRESS.m 1 of 1

```
% This file converts a .tif to stressed.  The function
% Calibration_curve_good.m is needed.

Title1 = 'name';
title2=strcat(num2str(Title1),'.tif')

A=imread(title2); %import image
B=rgb2gray(A);    %convert to gray
clear A
C=im2double(B);   %convert to double
clear B



Stress=(C');
Stress2=Stress;

% use calibration curve data

for loop=1:size(Stress2,1)
    for loop1=1:size(Stress2,2)
   Stress2(loop,loop1)=Calibration_curve_good(Stress2(loop,loop1));
    end
end

% write output
title3=strcat(num2str(Title1(zz)),'.mat');
save(title3,'-v7.3')
```

11/19/15 2:25 PM C:\Users\PA_Selv...\II_EQM.m 1 of 2

```
load('name.mat')

F=4400; %nominal applied load
L1=406.4;%mm %nominal area
w=0.5*25.4;%mm %nominla width
P=F/(L1*w); %nominal pressure

Stress1=Stress2;
thres=[12:0.1:50];

%This algorithm counts the pixels above a certain stress level "thres".
%Each pixel has a force  (pixelArea*pixelStress) that force is summed.
%Once the summed force equals the applied force "F" the "thres" is now a
%cutoff; everything blow this is noise.
for i=1:length(thres)

test=Stress1>=thres(i);
N=sum(sum(test));
Area_contact(i)=(N/(size(Stress1,1)*size(Stress1,2)))*100;

F(i)=P*L1*w;

%%
Stress2=Stress1.*test;
pix_w=(w./size(Stress2,1));
pix_L=(L1./size(Stress2,2));
pix= pix_L*pix_w;


%%

u(i)=mean2(Stress2(Stress2~=0));

F_bal(i)=u(i)*N*pix;

end
%%

%Manual determine where F_bal and F are equal. The corresponding "thres"↙
is
```

11/19/15 2:29 PM ...\III_ANALYZE_ASPERITIES.m 1 of 1

```
%

thres=21;  %units (MPa): this value is calulated manually from II_EQM.m

L1=400;%mm
w=12.7;%mm

%Pixel size definition

pix_w=(w./size(Stress2,1));     %mm
pix_L=(L1./size(Stress2,2));    %mm
pix= pix_L*pix_w;               %mm^2


%Filters erroneous noise from Film below thres
Stress=Stress2;
test=Stress>=thres;
N=sum(sum(test));
Stress2=Stress.*test;

%Find asperities.  Image detection algorithm
[L, num]=bwlabel(test,4);
STATS=regionprops(L,Stress2,'all');

% Save data
title4='Results_';
title5=strcat(title4,num2str(Title1(zz)),'.mat');
save(title5,'-v7.3')
```

11/19/15 2:34 PM C:\Users\...\IV_DISCRETIZE.m 1 of 2

```
title7='Results_name.mat';
load(title7);

%minimum threshold for asperity size as determined from the image↙
detection
%algorithm in III_ANALYZE_ASPERITIES.  This is important when generating
%abaqus models.  It is too difficult to model very small asperities.↙
Size
%is in total number of pixels

Min_asperity_size = 5; %pixels

%create a "STATS" structure for asperities along the interface. We store↙
x
%and y centroid location, area (in pixels), average normal stress,↙
standard
%deviation of normal stress field alond the asperity

        for a=1:length(STATS)

            if  STATS(a, 1).Area>=Min_asperity_size
            areaINFO(a,:,:,:,:,:)=[STATS(a, 1).Centroid(1).*pix_L,STATS↙
(a, 1).Centroid(2).*pix_w, STATS(a, 1).Area.*pix,STATS(a, 1).↙
MeanIntensity,std(STATS(a,1).PixelValues)];
            else
            areaINFO(a,:,:,:,:)=[nan,nan,nan,nan,nan];
            end

        end

x1=max(areaINFO(:,1))-areaINFO(:,1);
x1(isnan([x1(:)]))=[];
y=areaINFO(:,2);
y(isnan([y(:)]))=[];
A=areaINFO(:,3);
A(isnan([A(:)]))=[];
Sig=areaINFO(:,4);
Sig(isnan([Sig(:)]))=[];

ST_DEV=areaINFO(:,5);
ST_DEV(isnan([ST_DEV(:)]))=[];
```

```
TOTAL=[x1,y,A,Sig,ST_DEV];


INFO(1,z).x=TOTAL(:,1)';
INFO(1,z).y=TOTAL(:,2)';
INFO(1,z).A=TOTAL(:,3)';
INFO(1,z).SIG=TOTAL(:,4)';
INFO(1,z).ST_DEV=TOTAL(:,5)';
INFO(1,z).thresh=Min_asperity_size.*pix;
INFO(1,z).stress_crop=Stress2;
INFO(1,z).stress_image=Stress;


clearvars -except INFO

save('name_dicretized.mat','-v7.3')
```

11/19/15 2:18 PM ...\Calibration_curve_good.m 1 of 1

```
function out=Calibration_curve_good(input)
avg=↙
[0.411144160222084,0.421719098109199,0.442742998448631,0.478083773664135↙
,0.584994925989434,0.678496693144833,0.786651269669072,0.907904958533099↙
]-(0.411-0.27)+0.0299;
x=avg;
if input <=min(x);
        out=50;
elseif input >= min(x) && input <= x(2);
out = -7.943309066840878e+02*input + 3.764845135670759e+02;

elseif input >= x(2) && input <= x(3);
out = -2.663635153129446e+02*input + 1.538305814469709e+02;

elseif input >= x(3) && input <= x(4);
out = -1.598719882500293e+02*input + 1.066822034457622e+02;

elseif input >= x(4) && input <= x(5);
out = -51.444586279129370*input +54.844821942916330;

elseif input >= x(5) && input <= x(6);
out = -64.169910179644380*input +62.2890718562897;

elseif input >= x(6) && input <= x(7);
out = -60.099167403639610*input +59.5270863441272;

elseif input >= x(7) && input <= x(8);
out = -68.039167115579520*input +65.773097198696820;

else input >= max(x);
    out=0;

end
```

Bibliography

[1] *ABAQUS/Standard Version 6.4. ABAQUS Theory Manual. ABAQUS, Inc.; 2004.*

[2] L. Afferrante, G. Carbone, and G. Demelio. "Interacting and coalescing Hertzian asperities: A new multiasperity contact model". In: *Wear* 278-279.0 (2012), pp. 28–33.

[3] K Aki and P. G. Richards. *Quantitative Seismology*. Ed. by J. Ellis. 2nd. University Science Books, 2002.

[4] J. -P. Ampuero and A. M. Rubin. "Earthquake nucleation on rate and state faults: Aging and slip laws". In: *Journal of Geophysical Research* 113 (2008), B01302.

[5] R. Ando and K. Imanishi. "Possibility of M_w 9.0 mainshock triggered by diffusional propagation of after-slip from M_w 7.3 foreshock". In: *Earth Planets Space* 63.7 (2011), pp. 767–771.

[6] D. J. Andrews. "Rupture propagation with finite stress in antiplane strain". In: *Journal of Geophysical Research* 81.20 (1976), pp. 3575–3582.

[7] J. F. Archard. "Contact and Rubbing of Flat Surfaces". In: *Journal of Applied Physics* 24.8 (1953), pp. 981–988.

[8] J. F. Archard. "Single Contacts and Multiple Encounters". In: *Journal of Applied Geophysics* 32.8 (1961), pp. 1420–1425.

[9] K. Ariyoshi et al. "Influence of interaction between small asperities on various types of slow earthquakes in a 3-D simulation for a subduction plate boundary". In: *Godwana Reseach* 16 (2009), pp. 534–544.

[10] K. Ariyoshi et al. "Migration process of very low-frequency events based on a chain-reaction model and its application to the detection of preseismic slip for megathrust earthquakes". English. In: *Earth, Planets and Space* 64.8 (2012), pp. 693–702.

[11] E. M. Arruda, M. C. Boyce, and R. Jayachandran. "Effects of strain rate, temperature and thermomechanical coupling on the finite strain deformation of glassy polymers". In: *Mechanics of Materials* 19.2–3 (1995), pp. 193 –212.

[12] W. H. Bakun et al. "Implications for prediction and hazard assessment from the 2004 Parkfield earthquake". In: *Nature* 437 (2005), pp. 969–974.

[13] J. R. Barber. *Elasticity (Solid Mechanics and Its Applications)*. Ed. by G. M. L. Gladwell. 3rd. Springer Dordrecht Heidelberb, 2010.

[14] S. Barbot and Y. Fialko. "A unified continuum representation of post-seismic relaxation mechanisms: semi-analytic models of afterslip, poroelastic rebound and viscoelastic flow". In: *Geophysical Journal International* 182.3 (2010), pp. 1124–1140.

[15] G. I. Barenblatt. "The formation of equilibrium cracks during brittle fracture. General ideas and hypotheses. Axially-symmetric cracks". In: *Journal of Applied Mathematics and Mechanics* 23.3 (1959), pp. 622 –636.

[16] G. G. Batrouni, A. Hansen, and J. Schmittbuhl. "Elastic response of rough surfaces in partial contact". In: *EPL (Europhysics Letters)* 60.5 (2002), p. 724.

[17] T. Baumberger. "Contact dynamics and friction at a solid-solid interface: Material versus statistical aspects". In: *Solid State Communications* 102.2-3 (1997), pp. 175–185.

[18] T. Baumberger and C. Caroli. "Solid friction from stick-slip down to pinning and aging". In: *Advances in Physics* 55 (2006), pp. 279–348.

[19] N. M. Beeler, D. A. Lockner, and S. H. Hickman. "A simple stick-slip and creep-slip model for repeating earthquakes and its implication for microearthquakes at Parkfield". In: *Bulletin of the Seismological Society of America* 91.6 (2001), pp. 1797–1804.

[20] N. M. Beeler, T. E. Tullis, and J. D. Weeks. "The roles of time and displacement in the evolution effect in rock friction". In: *Geophysical Research Letters* 21.18 (1994), pp. 1987–1990.

[21] O. Ben-David, G. Cohen, and J. Fineberg. "The Dynamics of the Onset of Frictional Slip". In: *Science* 330.6001 (2010), pp. 211–214.

[22] I. A. Beresnev. "What We Can and Cannot Learn about Earthquake Sources from the Spectra of Seismic Waves". In: *Bulletin of the Seismological Society of America* 91.2 (2001), pp. 397–400.

[23] G. C. Beroza and W. L. Ellsworth. "Properties of the seismic nucleation phase". In: *Tectonophysics* 261.1-3 (1996), pp. 209–227.

[24] G. C. Beroza and S. Ide. "Slow Earthquakes and Nonvolcanic Tremor". In: *Annual Review of Earth and Planetary Sciences* 39 (2011), pp. 271–296.

[25] P. Berthoude and T. Baumberger. "Shear stiffness of a solidsolid multicontact interface". In: *Proceedings of the Royal Society of London A* 454.1974 (1998), pp. 1615–1634.

[26] P. Berthoude et al. "Physical analysis of the state- and rate-dependent friction law: Static friction". In: *Physical Review B: Condensed Matter and Materials Physics* 59.22 (1999), pp. 14313–14327.

[27] P. J. Blau. "Amontons' Laws of Friction". English. In: *Encyclopedia of Tribology*. Ed. by Q.Jane Wang and Yip-Wah Chung. Springer US, 2013, pp. 71–71.

[28] J. Boatwrigth and H. Quin. "Earthquake Source Mechanics". In: ed. by S. Das, J. Boatwright, and C. H. Scholz. American Geophysical Union, 1986. Chap. The Seismic Radiation from a 3-D Dynamic Model of a Complex Rupture Process. Part I: Confined Ruptures, pp. 97–109.

[29] M. S. Boettcher, A. McGarr, and M. Johnston. "Extension of Gutenberg-Richter distribution to M_W -1.3, no lower limit in sight". In: *Geophysical Research Letters* 36.10 (2009). L10307, n/a–n/a.

[30] G. N. Boitnott et al. "Micromechanics of Rock Friction 2: Quantitative Modeling of Initial Friction With Contact Theory". In: *Journal of Geophysical Research* 97.B6 (1992), pp. 8965–8978.

[31] E. Bouchaud. "Scaling properties of cracks". In: *Journal of Physics: Condensed Matter* 9.21 (1997), pp. 4319–4344.

[32] M. Bouchon et al. "The long precursory phase of most large interplate earthquakes". In: *Nature Geoscience* 6.4 (Apr. 2013), pp. 299–302.

[33] F. P. Bowden and D. Tabor. *The Friction and Lubrication of Solids*. New York: Oxford University Press, 2001.

[34] M. C. Boyce, D. M. Parks, and A. S. Argon. "Large inelastic deformation of glassy polymers. Part I: rate dependent constitutive model". In: *Mechanics of Materials* 7.1 (1988), pp. 15 –33.

[35] R. N. Bracewell. *The fast Fourier transform and its applications*. McGraw Hill, 1986.

[36] O.M. Braun et al. "Collective Effects at Frictional Interfaces". English. In: *Tribology Letters* 48.1 (2012), pp. 11–25.

[37] E. E. Brodsky and T. Lay. "Recognizing Foreshocks from the 1 April 2014 Chile Earthquake". In: *Science* 344.6185 (2014), pp. 700–702.

[38] S. R. Brown and C. H. Scholz. "Broad Bandwidth Study of the Topography of Natural Rock Surfaces". In: *Journal of Geophysical Research* 90.B14 (1985), pp. 12575–12582.

[39] J. N. Brune. "Correction [to Tectonic stress and the spectra, of seismic shear waves from earthquakes]". In: *Journal of Geophysical Research* 76.20 (1971), p. 5002.

[40] J. N. Brune. "Tectonic stress and spectra of seismic shear waves from earthquakes". In: *Journal of Geophysical Research* 75.26 (1970), pp. 4997–5009.

[41] R. Bürgmann. "Earth science: Warning signs of the Iquique earthquake". In: *Nature* 512.7514 (Aug. 2014), pp. 258–259.

[42] R. Bürgmann et al. "Earthquake Potential Along the Northern Hayward Fault, California". In: *Science* 289.5482 (2000), pp. 1178–1182.

[43] T. Candela et al. "Characterization of Fault Roughness at Various Scales: Implications of Three-Dimensional High Resolution Topography Measurements". In: *Pure and Applied Geophysics* 166 (2009), pp. 1817–1851.

[44] T. Candela et al. "Stress Drop during Earthquakes: Effect of Fault Roughness Scaling". In: *Bulletin of the Seismological Society of America* 101.5 (2011), pp. 2369–2387.

[45] G. Carbone and F. Bottiglione. "Asperity contact theories: Do they predict linearity between contact area and load?" In: *Journal of the Mechanics and Physics of Solids* 56.8 (2008), pp. 2555 –2572.

[46] C. Cattaneo. "Sul contatto di due corpi elastici: Distribuzione locale degli sforzi". In: *Reconditi del Accademia Nazionale de Lincei* 27 (1938), pp. 342–348,434–436,474–478.

[47] K. H. Chen, R. Burgmann, and R. M. Nadeau. "Do earthquakes talk to each other? Triggering and interaction of repeating sequences at Parkeld". In: *Journal of Geophysical Research* 118 (2013), pp. 165–182.

[48] F. M. Chester, J. P. Evans, and R. L. Biegel. "Internal structure and weakening mechanisms of the San Andreas Fault". In: *Journal of Geophysical Research: Solid Earth* 98.B1 (1993), pp. 771–786.

[49] L. Chiaraluce et al. "The anatomy of the 2009 LAquila normal fault system (central Italy) imaged by high resolution foreshock and aftershock locations". In: *Journal of Geophysical Research* 116.B12 (2011), B12311.

[50] M. Ciavarella. "The generalized Cattaneo partial slip plane contact problem. I - Theory". In: *International Journal of Solids and Structures* 35.18 (1998), pp. 2349–2362.

[51] M. Ciavarella. "The generalized Cattaneo partial slip plane contact problem. II - Examples". In: *International Journal of Solids and Structures* 35.18 (1998), pp. 2363–2378.

[52] M. Ciavarella, J.A. Greenwood, and M. Paggi. "Inclusion of interaction in the Greenwood and Williamson contact theory". In: *Wear* 265.5–6 (2008), pp. 729 –734.

[53] ClimateWire. *Leaking CO2 Fails to Cause Marine Catastrophe*. Scientifc American. 2014.

[54] S. Das and B. V. Kostrov. "Breaking of a Single Asperity Rupture Process and Seismic Radiation". In: *Journal of Geophysical Research* 88 (1983), B5.

[55] S. Das and B. V. Kostrov. "Breaking of a Single Asperity Rupture Process and Seismic Radiation". In: *Journal of Geophysical Research* 88 (1983), B5.

[56] S. Das and C. H. Scholz. "Theory of Time-Dependent Rupture in the Earth". In: *Journal of Geophysical Research* 86.B7 (1981), pp. 6039–6051.

[57] R. O. Davis and A. P. S. Selvadurai. *Elasticity and Geomechanics*. Cambridge University Press, 1996.

[58] C. DeMets et al. "Effect of recent revisions to the geomagnetic reversal time scale on estimates of current plate motions". In: *Geophysical Research Letters* 21.20 (1994), pp. 2191–2194.

[59] J. H. Dieterich. "A constitutive law for rate of earthquake production and its application to earthquake clustering". In: *Journal of Geophysical Research* 99 (1994), pp. 2601–2618.

[60] J. H. Dieterich. "Earthquake nucleation on faults with rate- and state-dependent friction". In: *Tectonophysics* 211 (1992), pp. 115–134.

[61] J. H. Dieterich. "Modeling of rock friction: 1. Experimental results and constitutive equations". In: *Journal of Geophysical Research* 84.B5 (1979), pp. 2161–2168.

[62] J. H. Dieterich. "Preseismic fault slip and earthquake prediction". In: *Journal of Geophysical Research* 83.B8 (1978), pp. 3940–3948.

[63] J. H. Dieterich and B. D. Kilgore. "Direct observation of frictional contacts: New insights for state-dependent properties". In: *Pure and Applied Geophysics* 143.1-3 (1994), pp. 283–302.

[64] J. H. Dieterich and B. D. Kilgore. "Imaging surface contacts: power law contact distributions and contact stresses in quartz, calcite, glass and acrylic plastic". In: *Tectonophysics* 256 (1996), pp. 219–239.

[65] J. H. Dieterich and B. D. Kilgore. "Implications of fault constitutive properties for earthquake prediction". In: *Proceedings of the National Academy of Sciences of the United States of America* 93.9 (1996), pp. 3787–3794.

[66] J. H. Dieterich and K. B. Richards-Dinger. "Earthquake Recurrence in Simulated Fault Systems". English. In: *Pure and Applied Geophysics* 167.8-9 (2010), pp. 1087–1104.

[67] D. A. Dodge, G. C. Beroza, and W. L. Ellsworth. "Detailed observations of California foreshock sequences: Implications for the earthquake initiation process". In: *Journal of Geophysical Research* 101.B10 (1996), pp. 22371–22392.

[68] D. A. Dodge, G. C. Beroza, and W. L. Ellsworth. "Foreshock sequence of the 1992 Landers, California, earthquake and its implications for earthquake nucleation". In: *Journal of Geophysical Research* 100.B6 (1995), pp. 9865–9880.

[69] P. Dublanchet, P. Bernard, and P. Favreau. "Interactions and triggering in a 3-D rate-and-state asperity model". In: *Journal of Geophysical Research* 118 (2013), pp. 2225–2245.

[70] W. L. Ellsworth and G. C. Beroza. "Seismic Evidence for an Earthquake Nucleation Phase". In: *Science* 268.5212 (1995), pp. 851–855.

[71] F. N. Fritsch and R. E. Carlson. "Monotone piecewise cubic interpolation". In: *SIAM Journal of Numerical Analysis* 17 (1980), pp. 238–246.

[72] M. Goldberg. "The Packing of Equal Circles in a Square". In: *Mathematical Magazine* 43.1 (1970), pp. 24–30.

[73] R. C. Gonzalez, R. Woods, and S. L. Eddins. *Digital Image Processing Using MATLAB*. Gatesmark Publishing, 2009.

[74] S. D. Goodfellow and R. P. Young. "A laboratory acoustic emission experiment under in situ conditions". In: *Geophysical Research Letters* 41.10 (2014), pp. 3422–3430.

[75] A. Govoni et al. "Investigating the Origin of Seismic Swarms". In: *EOS, Transactions American Geophysical Union* 94.41 (2013), pp. 361–362.

[76] J. A. Greenwood. "A note on Nayaks third paper". In: *Wear* 262 (2007), pp. 225–227.

[77] J. A. Greenwood. "A simplified elliptic model of rough surface contact". In: *Wear* 261 (2006), pp. 191–200.

[78] J. A. Greenwood and J. B. P. Williamson. "Contact of Nominally Flat Surfaces". In: *Proceedings of the Royal Society of London A* 295.1442 (1966), pp. 300–319.

[79] A. A. Griffith. "The Phenomena of Rupture and Flow in Solids". In: *Philosophical Transactions of the Royal Society of London A: Mathematical, Physical and Engineering Sciences* 221.582-593 (1921), pp. 163–198.

[80] A. Hansen et al. "Normal Stress Distribution of Rough Surfaces in Contact". In: *Geophysical Research Letters* 27.22 (2000), pp. 3639–3642.

[81] H. Hertz. "On the contact of firm elastic bodies (in German: Ueber die Berhrung fester elastischer Krper)". In: *Journal Reine Angewandte Mathematik* 92 (1882), pp. 156–171.

[82] S. G. Holtkamp, M. E. Pritchard, and R. B. Lohman. "Earthquake swarms in South America". In: *Geophysical Journal International* 187.1 (2011), pp. 128–146.

[83] Y. Ida. "Cohesive force across the tip of a longitudinal-shear crack and Griffith's specific surface energy". In: *Journal of Geophysical Research* 77.20 (1972), pp. 3796–3805.

[84] S. Ide. "Striations, duration, migration and tidal response in deep tremor". In: *Nature* 466 (2010), pp. 356–359.

[85] S. Ide and H. Aochi. "Earthquakes as multiscale dynamic ruptures with heterogeneous fracture surface energy". In: *Journal of Geophysical Research: Solid Earth* 110.B11 (2005), n/a–n/a.

[86] Y. Iio. "Observations of the slow initial phase generated by microearthquakes: Implications for earthquake nucleation and propagation". In: *Journal of Geophysical Research* 100.B8 (1995), pp. 15333–15349.

[87] K. L. Johnson. *Contact Mechanics*. Cambridge University Press, 1985.

[88] L. R. Johnson. "An earthquake model with interacting asperities". In: *Geophysical Journal International* 182.3 (2010), pp. 1339–1373.

[89] L. R. Johnson. "Greens Function for Lambs Problem". In: *Geophysical Journal of the Royal Astronomical Society* 37 (1974), pp. 99–131.

[90] L. R. Johnson and R. M. Nadeau. "Asperity Model of an Earthquake: Dynamic Problem". In: *Bulletin of the Seismological Society of America* 95.1 (2005), pp. 75–108.

[91] L. R. Johnson and R. M. Nadeau. "Asperity Model of an Earthquake: Static Problem". In: *Bulletin of the Seismological Society of America* 92.2 (2002), pp. 672–686.

[92] M. J. S. Johnston et al. "Continuous borehole strain and pore pressure in the near field of the 28 September 2004 M_w 6.0 Parkfield, California, earthquake: Implications for nucleation, fault response, earthquake prediction, and tremor". In: *Bulletin of the Seismological Society of America* 96.4B (2006), S56–S72.

[93] L. M. Jones and P. Molnar. "Some characteristics of foreshocks and their possible relationship to earthquake prediction and premonitory slip on faults". In: *Journal of Geophysical Research* 84.B7 (1979), pp. 3596–3608.

[94] Y. Kaneko and J. -P. Ampuero. "A mechanism for preseismic steady rupture fronts observed in laboratory experiments". In: *Geophysical Research Letters* 38.21 (2011), p. L21307.

[95] B. M. Kaproth and C. Marone. "Slow Earthquakes, Preseismic Velocity Changes, and the Origin of Slow Frictional Stick-Slip". In: *Science* 314.6151 (2013), pp. 1229–1232.

[96] A. Kato, T. Igarashi, and K. Obara. "Detection of a hidden Boso slow slip event immediately after the 2011 Mw 9.0 Tohoku-Oki earthquake, Japan". In: *Geophysical Research Letters* 41.16 (2014), pp. 5868–5874.

[97] A. Kato et al. "Propagation of Slow Slip Leading Up to the 2011 $M_w 9.0 Tohoku-Oki Earthquake$". In: *Science* 335 (2012), pp. 705–708.

[98] N. Kato. "Interaction of slip on asperities: Numerical simulation of seismic cycles on a two-dimensional planar fault with nonuniform frictional property". In: *Journal of Geophysical Research: Solid Earth* 109.B12 (2004), n/a–n/a.

[99] L. Knopoff. "Energy release in earthquakes". In: *Geophysical Journal International* 1.1 (1958), pp. 44–52.

[100] B.V. Kostrov. "Unsteady propagation of longitudinal shear cracks". In: *Journal of Applied Mathematics and Mechanics* 30.6 (1966), pp. 1241–1248.

[101] B. A. Krick et al. “Optical In Situ Micro Tribometer for Analysis of Real Contact Area for Contact Mechanics, Adhesion, and Sliding Experiments”. English. In: *Tribology Letters* 45.1 (2012), pp. 185–194.

[102] J. Langbein, J. R. Murray, and H. A. Snyder. “Coseismic and Initial Postseismic Deformation from the 2004 Parkfield, California, Earthquake, Observed by Global Positioning System, Electronic Distance Meter, Creepmeters, and Borehole Strainmeters”. In: *Bulletin of the Seismological Society of America* 96.4B (2006), S304–S320.

[103] S. Langers et al. “Stress heterogeneities in earthquake rupture experiments with material contrasts”. In: *Journal of the Mechanics and Physics of Solids* 61 (2013), pp. 742–761.

[104] N. Lapusta et al. “Elastodynamic analysis for slow tectonic loading with spontaneous rupture episodes on faults with rate- and state-dependent friction”. In: *Journal of Geophysical Research* 105.B10 (2000), pp. 23,765–23,789.

[105] S. Latour et al. “Characterization of nucleation during laboratory earthquakes”. In: *Geophysical Research Letters* 40.19 (2013), pp. 5064–5069.

[106] T. Lay and T. C. Wallace. *Modern Global Seismology*. San Diego, CA,USA: Academic Press, 1995.

[107] O. Lengliné et al. “Interplay of seismic and aseismic deformations during earthquake swarms: An experimental approach”. In: *Earth and Planetary Science Letters* 331-332 (2012), pp. 215–223.

[108] Q. Li et al. “Frictional ageing from interfacial bonding and the origins of rate and state friction”. In: *Nature* 480 (2011), pp. 233–236.

[109] J. Lin and R. S. Stein. “Stress triggering in thrust and subduction earthquakes and stress interaction between the southern San Andreas and nearby thrust and strike-slip faults”. In: *Journal of Geophysical Research: Solid Earth* 109.B2 (2004), n/a–n/a.

[110] D. A. Lockner. “The Role of Acoustic Emission in the study of Rock Fracture”. In: *International Journal of Rock Mechanics and Mining Sciences & Geomechanics Abstracts* 30.7 (1993), pp. 883–899.

[111] X. Lu, N. Lapusta, and A. J. Rosakis. “Pulse-like and crack-like dynamic shear ruptures on frictional interfaces: experimental evidence, numerical modeling, and implications”. In: *International Journal of Fracture* 163 (2010), pp. 27–39.

[112] V. Lyakhovsky. “Scaling of fracture length and distributed damage”. In: *Geophysical Journal International* 144.1 (2001), pp. 114–122.

[113] C. Marone. “Laboratory derived friction laws and their application to seismic faulting”. In: *Annual Review of Earth and Planetary Sciences* 26 (1998), pp. 643–696.

[114] MATLAB. *Version 8.3 (R2014a)*. Natick, Massachusetts: The MathWorks Inc., 2014.

[115] G. C. McLaskey. “Stress Wave Source Characterization: Impact, Fracture, and Sliding Friction”. PhD thesis. University of California, Berkeley, 2011.

[116] G. C. McLaskey and S. D. Glaser. “Acoustic Emission Sensor Calibration for Absolute Source Measurements”. In: *Journal of Nondestructive Evaluation* 31.2 (2012), pp. 157–168.

[117] G. C. McLaskey and S. D. Glaser. "Hertzian impact: experimental study of the force pulse and resulting stress waves". In: *Journal of the Acoustical Society of America* 128 (2010), pp. 1087–1096.

[118] G. C. McLaskey and S. D. Glaser. "Micromechanics of asperity rupture during laboratory stick slip experiments". In: *Geophysical Research Letters* 38.12 (2011), p. L12302.

[119] G. C. McLaskey and B. D. Kilgore. "Foreshocks during the nucleation of stick-slip instability". In: *Journal of Geophysical Research* 118.6 (2013), pp. 2982–2997.

[120] G. C. McLaskey and D. A. Lockner. "Preslip and cascade processes initiating laboratory stick slip". In: *Journal of Geophysical Research: Solid Earth* 119.8 (2014), pp. 6323–6336.

[121] G. C. McLaskey et al. "Fault healing promotes high-frequency earthquakes in laboratory experiments and on natural faults". In: *Nature* 491 (2012), pp. 101–105.

[122] G. C. McLaskey et al. "Laboratory Generated **M** -6 Earthquakes". In: *Pure and Applied Geophysics* (2014).

[123] L. Meng et al. "Dual megathrust slip behaviors of the 2014 Iquique earthquake sequence". In: *Earth and Planetary Science Letters* 411 (2015), pp. 177 –187.

[124] A. Mignan. "The debate on the prognostic value of earthquake foreshocks: A meta-analysis". In: *Scientific Reports* 4 (2014), p. 4099.

[125] R. D. Mindlin. "Compliance of elastic bodies in contact". In: *Journal of Applied Mathematics* 16 (1949), pp. 259–268.

[126] K. Mogi. "Some Discussions on Aftershocks, Foreshocks and Earthquake Swarms: the Fracture of a Semi-infinite Body Caused by an Inner Stress Origin and Its Relation to the Earthquake Phenomena (Third Paper)". In: *Bulletin of the Earthquake Research Institute* 41 (1963), pp. 615–658.

[127] R. Monatersky. "Seabed scars raise questions over carbon-storage plan". In: *Nature* 504 (2013), pp. 339–340.

[128] O. Mutlu and A. Bobet. "Slip initiation on frictional fractures". In: *Engineering Fracture Mechanics* 72 (2005), pp. 729–747.

[129] R. M. Nadeau and L. R. Johnson. "Seismological Studies at Parkfield VI: Moment Release Rates and Estimates of Source Parameters for Small Repeating Earthquakes". In: *Bulletin of the Seismological Society of America* 88.3 (1998), pp. 790–814.

[130] R. M. Nadeau and T. V. McEvilly. "Fault Slip Rates at Depth from Recurrence Intervals of Repeating Microearthquakes". In: *Science* 285.5428 (1999), pp. 718–721.

[131] R. M. Nadeau et al. "Seismological studies at Parkfield III: Microearthquake clusters in the study of fault-zone dynamics". In: *Bulletin of the Seismological Society of America* 84.2 (1994), pp. 247–263.

[132] B. Nagata K.and Kilgore, N. Beeler, and M. Nakatani. "High-frequency imaging of elastic contrast and contact area with implications for naturally observed changes in fault properties". In: *Journal of Geophysical Research: Solid Earth* 119.7 (2014), pp. 5855–5875.

[133] P. R. Nayak. "Random process model of rough surfaces in plastic contact". In: *Wear* 26 (1973), pp. 305–333.

[134] H. Noda, M. Nakatani, and T. Hori. "Large nucleation before large earthquakes is sometimes skipped due to cascade-Implications from a rate and state simulation of faults with hierarchical asperities". In: *Journal of Geophysical Research: Solid Earth* 118.6 (2013), pp. 2924–2952.

[135] I. Nogueira, F. Robbe-Valloire, and R. Gras. "Experimental validations of elastic to plastic asperity-based models using normal indentations of rough surfaces". In: *Wear* 269.11-12 (2010), pp. 709 –718.

[136] K. Obara. "Characteristics and interactions between non-volcanic tremor and related slow earthquakes in the Nankai subduction zone, southwest Japan". In: *Journal of Geodynamics* 52.3–4 (2011), pp. 229 –248.

[137] Y. Ogata. "Statistical models for earthquake ooccurrence and residual analysis for point processes". In: *Journal of the American Statistical Association* 83.401 (1988), pp. 9–27.

[138] M. Ohnaka. "Critical Size of the Nucleation Zone of Earthquake Rupture Inferred from Immediate Foreshock Activity". In: *Journal of Physics of the Earth* 41.1 (1993), pp. 45–56.

[139] M. Ohnaka. "Earthquake source nucleation: A physical model for short-term precursors". In: *Tectonophysics* 211.1-4 (1992), pp. 149–178.

[140] M. Ohnaka and L. F. Shen. "Scaling of the shear rupture process from nucleation to dynamic propagation: Implications of geometric irregularity of the rupturing surfaces". In: *Journal of Geophysical Research* 104.B1 (1999), pp. 817–844.

[141] M. Ohnaka and T. Yamashita. "A cohesive zone model for dynamic shear faulting based on experimentally inferred constitutive relation and strong motion source parameters". In: *Journal of Geophysical Research: Solid Earth* 94.B4 (1989), pp. 4089–4104.

[142] P. G. Okubo and J. H. Dieterich. "Effects of physical fault properties on frictional instabilities produced on simulated faults". In: *Journal of Geophysical Research* 89.B7 (1984), pp. 5817–5827.

[143] M. Paggi, R. Pohrt, and V. L. Popov. "Partial-slip frictional response of rough surfaces". In: *Scientific Reports* 4 (2014), p. 5178.

[144] Z. Peng and J. Gomberg. "An integrated perspective of the continuum between earthquakes and slow-slip phenomena". In: *Nature Geoscience* 3 (2010), pp. 599–607.

[145] B. N. J. Persson. "Contact mechanics for randomly rough surfaces". In: *Surface Science Reports* 61.4 (2006), pp. 201–227.

[146] B. N. J. Persson. "Sliding Friction". In: *Surface Science Reports* 33 (1999), pp. 89–119.

[147] B. N. J. Persson. "Theory of friction: Friction dynamics for boundary lubricated surfaces". In: *Physical Review B: Condensed Matter and Materials Physics* 55.12 (1997), pp. 8004–8012.

[148] B. N. J. Persson, F. Bucher, and B. Chiaia. "Elastic contact between randomly rough surfaces: Comparison of theory with numerical results". In: *Phys. Rev. B* 65 (18 2002), p. 184106.

[149] W. L. Power and T. E. Tullis. "Euclidean and Fractal Models for the Description of Rock Surface Roughness". In: *Journal of Geophysical Research* 96.B1 (1991), pp. 415–424.

[150] C. Putignano et al. “The influence of the statistical properties of self-affine surfaces in elastic contacts: A numerical investigation”. In: *Journal of the Mechanics and Physics of Solids* 60.5 (2012), pp. 973 –982.

[151] J. R. Rice and Y. Ben-Zion. “Slip complexity in earthquake fault models”. In: *Proceedings of the National Academy of Sciences of the United States of America* 93.9 (1996), pp. 3811–3818.

[152] J. R. Rice and M. Cocco. “Seismic fault rheology and earthquake dynamics”. In: *Tectonic Faults: Agents of Change on a Dynamic Earth*. Cambridge, Mass.: MIT Press, 2007. Chap. 5, pp. 99–137.

[153] J. Ripperger et al. “Earthquake source characteristics from dynamic rupture with constrained stochastic fault stress”. In: *Journal of Geophysical Research* 112 (2007), B04311.

[154] F. Robbe-Valloire, B. Paffoni, and R. Progri. “Load transmission by elastic, elasto-plastic or fully plastic deformation of rough interface asperities”. In: *Mechanics of Materials* 33.11 (2001), pp. 617 –633.

[155] E. A. Roeloffs. “Evidence for aseimsic defomation rate changes prior to earthquakes”. In: *Annual Review of Earth and Planetary Sciences* 34.1 (2006), pp. 591–627.

[156] S. M. Rubinstein, G. Cohen, and J. Fineberg. “Detachment fronts and the onset of dynamic friction”. In: *Nature* 430 (2004), pp. 1005–1009.

[157] A. Ruina. “Slip instability and state variable friction laws”. In: *Journal of Geophysical Research* 88.B12 (1983), pp. 10,359–10,370.

[158] S. Saltiel et al. “Experimental development of low-frequency shear modulus and attenuation measurements for fractured rocks: detectability of fractures at various stress conditions”. in prepartion for Geophysics.

[159] J. Schmittbuhl et al. “Are stress distributions along faults the signature of asperity squeeze?” In: *Geophysical Research Letters* 33.13 (2006), p. L13307.

[160] J. Schmittbuhl et al. “Slow Crack Propagation and Slip Correlations”. English. In: *pure and applied geophysics* 160.5-6 (2003), pp. 961–976.

[161] C. H. Scholz. *The Mechanics of Earthquakes and Faulting*. 2nd. UK: Cambridge University Press, 2002.

[162] A. P. S. Selvadurai, A. P. Suvorov, and P. A. Selvadurai. “Thermo-hydro-mechanical processes in fractured rock formations during a glacial advance”. In: *Geoscientific Model Development* 8.7 (2015), pp. 2167–2185.

[163] A. P. S. Selvadurai and Q. Yu. “Mechanics of a discontinuity in a geomaterial”. In: *Computers and Geotechnics* 32 (2005), pp. 92–106.

[164] P. A. Selvadurai and S. D. Glaser. “Direct measurement of contact area and seismic stress along a sliding interface”. In: *46th US Rock Mechanics / Geomechanics Symposium*. Chicago, IL., 2012, ARMA 12–538.

[165] P. A. Selvadurai and S. D. Glaser. “Insights into dynamic asperity failure in the laboratory”. In: *48th US Rock Mechanics / Geomechanics Symposium*. Minneapolis, MN, USA, 2014, ARMA 14–143.

[166] P. A. Selvadurai and S. D. Glaser. "Laboratory-developed Contact Models Controlling Instability on Frictional Faults". In: *Journal of Geophysical Research* 120.6 (2015), pp. 4208–4236.

[167] P. A. Selvadurai and S. D. Glaser. "Novel Monitoring Techniques for Characterizing Frictional Interfaces in the Laboratory". In: *Sensors* 15.5 (2015), pp. 9791–9814.

[168] P.A. Selvadurai and S. D. Glaser. "Experimental evidence of micromechanical processes that control localization of shear rupture nucleation". In: *47th U.S. Rock Mechanics/Geomechanics Symposium*. San Fransisco, CA., 2013, ARMA 13–639.

[169] E. Specht. *The best known packings of equal circles in a square (up to N = 10000)*. English. 2015. URL: http://hydra.nat.uni-magdeburg.de/packing/csq/csq.html#Overview.

[170] H. Spetzler. "Seismic Velocity Changes during Fracture and Frictional Sliding". English. In: *Rock Friction and Earthquake Prediction*. Ed. by JamesD. Byerlee and Max Wyss. Vol. 6. Contributions to Current Research in Geophysics (CCRG). Birkhäuser Basel, 1978, pp. 732–742.

[171] S. Stanchits et al. "Fracturing of porous rock induced by fluid injection". In: *Tectonophysics* 503.1-2 (2010), pp. 129–145.

[172] R. S. Stein. "The role of stress transfer in earthquake occurrence". In: *Nature* 402 (1999), pp. 605–609.

[173] V. Subramanian and R. P. Singh. "Experimental Observation of Slip Pulses During Onset of Sliding Friction". English. In: *Dynamic Behavior of Materials, Volume 1*. Ed. by Bo Song, Daniel Casem, and Jamie Kimberley. Conference Proceedings of the Society for Experimental Mechanics Series. Springer International Publishing, 2015, pp. 133–140.

[174] Swissinfo. *Earth-shaking energy project cleared in court*. 2009.

[175] C. Tape et al. "Earthquake nucleation and triggering on an optimally oriented fault". In: *Earth and Planetary Science Letters* 363 (2013), pp. 231–241.

[176] B. D. Thompson, R. P. Young, and D. A. Lockner. "Premonitory acoustic emissions and stick-slip in natural and smooth-faulted Westerly granite". In: *Journal of Geophysical Research* 114.B2 (2009), B02205.

[177] S. P. Timoskenko and J. N. Goodier. *Theory of Elasticity*. New York: McGraw-Hill, 1970.

[178] A. C. To and S. D. Glaser. "Full waveform inversion of a 3-D source inside an artificial rock". In: *Journal of Sound and Vibration* 285 (2005), pp. 835–857.

[179] T. E. Tullis. "Rock friction and its implications for earthquake prediction examined via models of Parkfield earthquakes". In: *Proceedings of the National Academy of Sciences of the United States of America* 93.9 (1996), pp. 3803–3810.

[180] A. Udías, R. Madriaga, and E. Buforn. *Source Mechanisms of Earthquakes: Theory and Practice*. University Printing House, Cambridge: Cambridge University Press, 2014.

[181] J. Vidale, J. Mori, and H. Houston. "Something wicked this way comes: Clues from foreshocks and earthquake nucleation". In: *Eos, Transactions American Geophysical Union* 82.6 (2001), pp. 68–68.

[182] F. T. Wu, K. C. Thomson, and H. Kuenzler. "Stick-slip propagation velocity and seismic source mechanism". In: *Bulletin of the Seismological Society of America* 62 (1972), pp. 1621–1628.

[183] Y. Yagi et al. "Rupture process of the 2014 Iquique Chile Earthquake in relation with the foreshock activity". In: *Geophysical Research Letters* 41 (2014), pp. 4201–4206.

[184] V. A. Yastrebov, G. Anciaux, and J. -F. Molinari. "Contact between representative rough surfaces". In: *Phys. Rev. E* 86 (3 2012), p. 035601.

[185] N. Yoshioka. "A review of the micromechanical approach to the physics of contacting surfaces". In: *Tectonophysics* 277 (1997), pp. 29–40.

[186] N. Yoshioka and K. Iwasa. "The characteristic displacement in rate and state-dependent friction from a micromechanical point of view". In: *Pure and Applied Geophysics* 147.3 (1996), pp. 433–453.